Modifying Single-Molecule Fluorescence with a Plasmonic Optical Antenna: Theory, Methodology, and Measurement

by

Benjamin P. Isaacoff

A dissertation submitted in partial fulfillment
of the requirements for the degree of
Doctor of Philosophy
(Applied Physics)
in The University of Michigan
2018

Doctoral Committee:

Associate Professor Julie S. Biteen, Chair
Professor Anthony Grbic
Professor Nicholas A. Kotov
Assistant Professor Somin Eunice Lee
Professor Roberto D. Merlin

Benjamin P. Isaacoff

isaacoff@umich.edu

ORCID iD: 0000-0002-2022-4074

For Ira & Kendall

Parents: creators, caretakers, teachers, and more. Loving linchpins.

ACKNOWLEDGEMENTS

This dissertation is not the result of my efforts alone, it is the result of a series of collaborations, communities, mentorships, and diverse arrays of support structures. Here, I'd like to briefly thank some of the people who have made this possible.

First and foremost is my advisor, Professor Julie Biteen. Julie welcomed me into her lab under unusual circumstances and at a challenging moment in my life. Nonetheless, Julie helped me to hit the ground running and we immediately started working on several projects simultaneously—we've never dropped the pace since. Over the last five years Julie has pushed and challenged me to grow as a scientist and as a person. I will always be grateful for the wonderful lab Julie has assembled, the space she made for me there, and for the superhuman amounts of labor she put into supporting me and our lab.

Maybe the single greatest lesson of my PhD is the preeminent importance of being part of a good team. A good team working together can accomplish orders of magnitude more than the team members alone could possibly have—truly, the whole is greater than sum of its parts. Being part of intense and long standing teams is not exclusively smiles and high fives, but it is a lot of growth and it is very productive.

The most important team that I've been a part of is the Biteen Lab. During my time in the Biteen Lab, I've had the honor to work with many amazing scientists. In particular, my Team Plasmons crew Bing Fu, Stephen Lee, and Curly Zuo, who were my close collaborators and friends, through fun times, challenging times, and successes and failures—this wouldn't have been possible without you guys. Stephen, I am constantly amazed by the breadth of your expertise and how generously you share it. I benefited tremendously from the mentorship and collaboration of Esther Wertz and Jessica Flynn. I owe much of my Matlab prowess (my only real superpower) to the tutelage of David Rowland and Yi Liao. To Bing, Stephen, Curly, Esther, Jess, Dave, Yi, Josh, Yilai, Hannah H, Hannah C, Chan, Beth, and all the other wonderful scientists that have passed through our lab, thank you, you've all been great labmates and I'm a better scientist for having worked with you.

I had the opportunity to spend a fantastic summer of stimulating science and great fun working at Leiden University in the Netherlands. Thanks to Michel Orrit for having me, Martin Caldarola and Thomas Jollans for letting me wreak havoc for a few months, and to the entire MoNOS group for warmly welcoming me as a colleague and friend.

Finally, I never would have gotten here in the first place, let alone completed this journey, without the love and support of my family. I'm quite sure that I have greatest parents that have ever existed, and all that I do is a testament to this truth. My brother Max's movie star good looks and charisma are only outdone by his genuine kindness and empathy, and as a team we are unstoppable. I am inexpressibly lucky to have the love and companionship of my partner Amanda. Amanda, you're my partner in so many different ways, whether we're travelling the world, crafting something tasty, learning from each other (mostly me from you), or just going for a walk, I'm so happy to be doing it with you. I love you darling, and I look forward to soon reading my acknowledgement in your dissertation.

TABLE OF CONTENTS

CHAPTER

LIST OF FIGURES

Figure

LIST OF TABLES

Table

LIST OF ABBREVIATIONS

CTAB cetrimonium bromide

e-beam electron-beam lithography

EMCCD electron multiplying charge-coupled device

FDTD finite difference time domain

FEM finite element method

GNR gold nanorod

ITO indium tin oxide

LDOS local density of (photonic) states

LM longitudinal plasmon mode

LSPR localized surface plasmon resonance

NA numerical aperture

NI nano-island

NP nanoparticle

NSOM near-field scanning optical microscopy

NT nano-triangle

OD optical density

PAINT points accumulation for imaging in nanoscale topography

PALM photoactivated localization microscopy

PL photoluminescence

PSF point spread function

sCMOS scientific complementary metal-oxide-semiconductor

SEM scanning electron microscope

SNR signal-to-noise ratio

SOFI super-resolution optical fluctuation imaging

SPP surface plasmon polariton

STED stimulated emission depletion

STORM stochastic optical reconstruction microscopy

TM transverse plasmon mode

ABSTRACT

Nanophotonics is the study and technological application of light on the nanometer scale. This dissertation brings together two disparate branches of nanophotonics: plasmonics and single-molecule super-resolution microscopy. Plasmonics studies the collective oscillations of free electrons in a conductor, which enable light to be manipulated on subwavelength length scales. Plasmonics, and in particular plasmonic optical antennas, have generated a huge amount of interest due to their rich new physics and countless applications, ranging from surface-enhanced spectroscopies, to novel cancer therapies, and to quantum information platforms. With single-molecule fluorescence super-resolution microscopy, the optical properties of individual molecules can be studied with nanometer-scale resolution, far better than the micron scale of traditional microscopy. Super-resolution microscopy has revolutionized cellular biomedicine, ushering in a new generation of fundamental discoveries and associated medical therapies. Super-resolution microscopy is also increasingly enabling discoveries and advances across disciplines, allowing direct visualizations of phenomena ranging from chemical imaging of surface reactions to nanoscale fluid dynamics. By bringing together these two fields, this dissertation supports two synergistic directions for applications of this science: enhancing the resolution of single-molecule fluorescence super-resolution imaging and using a novel technique to directly study how a single emitter interacts with an optical antenna.

In this dissertation, I present a new theoretical approach to understand the interaction of a single fluorescent molecule with an optical antenna, a broadly applicable new image analysis algorithm, and experimental measurements of antenna-modified fluorescence. The theoretical framework expands an established theory of antenna-modified fluorescence to incorporate the variability of real experiments. This research has uncovered a mislocalization effect: differences between the actual position of an emitter and the apparent, super-resolved position of the emitter image. I therefore present computational methods to predict the emission mislocalization of single fluorescent molecules coupled to an optical antenna and compare these predictions to experiments. I describe the SMALL-LABS algorithm, a general data analysis approach to accurately locating and measuring the intensity of single molecules, regardless of the shape or brightness of an obscuring background. Finally, I present the results of experiments studying the polarization dependence of coupling a single fluorescent molecule to a gold nanorod plasmonic optical antenna, and I compare these measurements with theoretical predictions. This work advances the fundamental science of nanophotonics and will pave the way for next-generation super-resolution imaging and optical antenna technologies.

CHAPTER I

Introduction

Nanophotonics is the study and technological application of light on the nanometer scale. Like nanotechnology in general, what unifies this field is a length scale, and not a particular set of questions, techniques, or even disciplines. The wide range of nanophotonics gives me hope that the impact of my work may extend to researchers and applications far beyond my sub-field.

My dissertation is at the intersection of two disparate branches of nanophotonics: plasmonics and single-molecule super-resolution microscopy. Plasmonics studies the collective oscillations of free electrons in a conductor, which enable light to be manipulated on subwavelength length scales. With single-molecule fluorescence super-resolution microscopy, the optical properties of individual molecules can be studied with nanometer-scale resolution, far better than the micron scale of traditional microscopy.

Super-resolution microscopy has revolutionized cellular biomedicine [1–6], ushering in a new generation of fundamental discoveries and associated medical therapies. Super-resolution microscopy is also increasingly enabling discoveries and advances across disciplines [7–11], allowing direct visualizations of diverse phenomena ranging from chemical imaging of surface reactions [12] to nanoscale fluid dynamics [13, 14].

In Chap. II, I give a brief overview and introduction to single-molecule fluorescence super-resolution microscopy. The chapter starts with an introduction to microscopy and fluorescence, and then moves on to an overview of the tools and techniques for imaging single molecules. I end the chapter by describing how single-molecule imaging enables super-resolution measurements, and briefly discuss some of the other approaches available.

Plasmonics, and in particular plasmonic optical antennas, have generated a huge amount of interest due to their rich new physics and countless applications [15–25], ranging from surface-enhanced spectroscopies [26, 27], to novel cancer therapies [28–30], and to quantum information platforms [31–33].

In Chap. III, I give a brief overview of plasmonics and optical antennas, and I present derivations for some fundamental results. I specifically focus on how plasmonic nanoparticles function as an optical antenna, detailing how they act on the excitation and emission of a coupled fluorophore. I then explain the main electromagnetic simulation technique I used in this dissertation, the finite difference time domain (FDTD) method. I end the chapter with an introduction to gold nanorods (GNRs), which are the main plasmonic optical antenna discussed throughout the rest of the dissertation.

By bringing together these two fields, this dissertation supports two synergistic directions for applications of this science: enhancing the resolution of single-molecule fluorescence super-resolution imaging and using a novel technique to directly study how a single emitter interacts with an optical antenna.

In Chap IV, I present a new theoretical approach to understand the interaction of a single fluorescent molecule with an optical antenna. This understanding is essential to enhancing the resolution of single-molecule fluorescence super-resolution imaging and is integral to fundamental studies of optical antennas. I expand on a theoretical framework first published in 2008 [34] to accurately predict real experiments. I end this chapter by applying this framework to predicting how a GNR modifies the fluorescence of coupled emitters, experimental measuresments of which are the subject of Chap. VII.

Gold nanoparticles are intrinsically photoluminescent, and in a single-molecule imaging experiment, a background composed of gold nanoparticles looks exactly like the foreground being measured—single-fluorescent molecules. As I worked on these experiments I realized that there was no accurate background-removal approach capable of dealing with this kind of background. To address this need, I invented the SMALL-LABS algorithm, a general data analysis approach which accurately locates and measures the intensity of single molecules, regardless of the shape or brightness of the background. Chap. V presents the SMALL-LABS algorithm.

Research in our group studying plasmonics with super-resolution microscopy has discovered the mislocalization effect [35], in which significant inaccuracies in super-resolution localization of an emitter are introduced by coupling (even very weakly) the emission from that emitter to an optical antenna. In Chap. VI, I explain the origin of the mislocalization effect and detail our investigations of the effect, focusing on my theoretical predictions and computational approaches to mislocalization, published in [35–37].

In Chap. VII, I detail my experimental and theoretical investigations of the excitation polarization dependence of fluorescence enhancement for single molecules coupled to a GNR plasmonic optical antenna.

CHAPTER II

Single-Molecule Fluorescence Super-Resolution Microscopy

2.1 Microscopy

2.1.1 Introduction to Microscopy

Before delving into the function of a microscope, I will begin by reviewing what an imaging system is, after all, a microscope is simply a specialized imaging system. All imaging systems share the same basic structure as shown in Fig. 2.1a. Optical radiation (light) is radiated from an object. This radiation could be emitted from an emitter, like a fluorescent molecule, a lightbulb, or a bioluminescent jellyfish, or it could be scattered from the object. Scattering can take many forms, reflection and transmission for example (how we view most of the world) are simply forms of directional elastic scattering. Regardless of the origin of the radiation, the function of an imaging system is to transform that radiation into an image which is then detected. The simplest imaging system is a single lens (Fig. 2.1b) coupled to a detector.

For an object larger than the diffraction limit of our imaging system (discussed in detail in Sec. 2.1.2), Fig. 2.1b fails capture the whole story. The diffraction limit of an imaging system is the minimum separation at which two infinitesimal sources of light, referred to as point emitters, can be distinguished. We can view an object bigger than the system

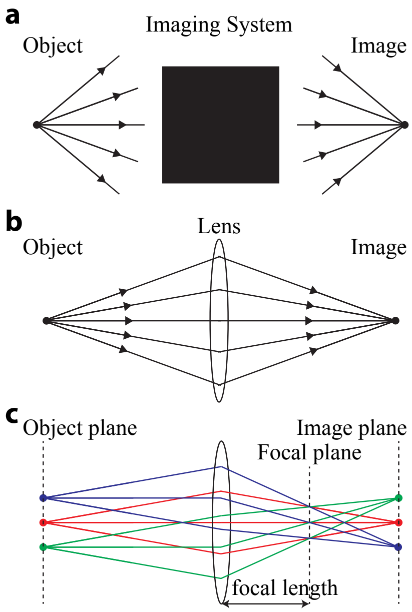

Figure 2.1: A generalized imaging system. In a - c, the image plane contains a detector. (a) A black box imaging system. (b) A simple lens can function as an imaging system. (c) A lens forming an image for multiple point sources (colored for clarity) which is equivalent to imaging an object larger than the diffraction limit.

diffraction limit as being effectively composed of multiple point emitters. As shown in Fig. 2.1c, the function of the imaging system is still to transform the emitted radiation from the object into an image.

The focal plane of a lens in an imaging system contains the spatial Fourier transform of the object. This is easy to see in Fig. 2.1c if you think of a spatial Fourier transform as showing the angular distribution of the emitted radiation. The light emitted at a specific *angle* converges in the *focal* plane (a spatial Fourier transform), whereas the light emitted from a specific *object* converges in the *imaging* plane.

A microscope is an image-forming device that magnifies an object and makes this magnified image accessible to the eye. Fig. 2.2 shows how with just two lenses, an eyepiece and an objective lens, a microscope acts as a magnifying image formation device. A telescope has a very similar setup and function, however, the difference between a microscope and a telescope is that in a telescope configuration, the eyepiece and the objective

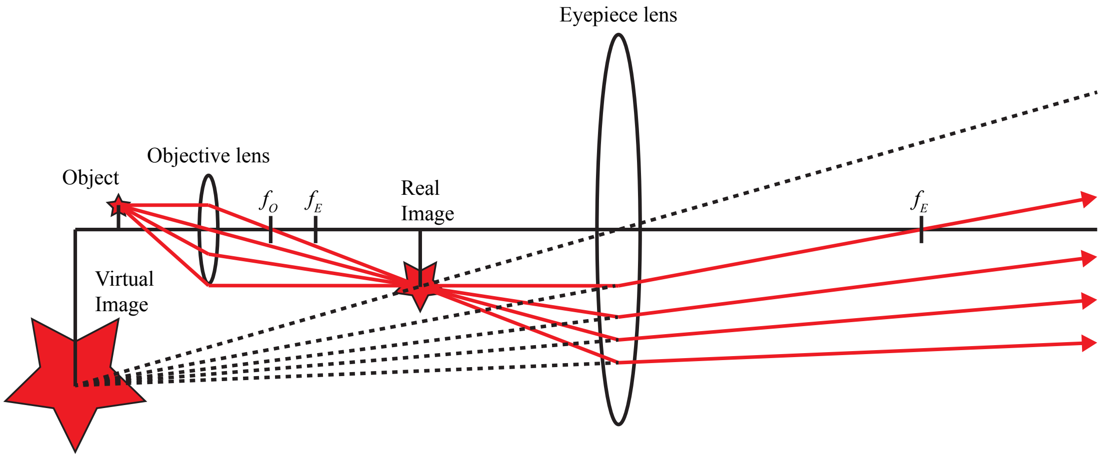

Figure 2.2: Simple microscope ray diagram. With just two lens a microscope can magnify and create an image. f_E is the focal length of the eyepiece lens and f_O is the focal length of the objective lens.

lens focal planes overlap. The consequence is that the collimation (a collimated beam is composed of parallel rays) of the observed light is not changed in a telescope, whereas in a microscope configuration with non-overlapping focal planes, this is not the case.

Shortly after their invention, microscopes quickly evolved beyond a simple two lens design. Modern research microscopes are highly complex, extremely precise, configurable, and reliable, workhorses of scientific research. Microscopes come in many different shapes, sizes, and configurations, designed and used for myriad applications. Some example microscopes are shown in Fig. 2.3. The light path and optics shown for the Olympus IX70 in Fig 2.3b are quite similar to the light path and optics in Fig. 2.3c, the Olympus IX71 inverted microscope, used for the experiments described in this thesis.

Arguably the most important component of a microscope is the objective lens (Fig. 2.2 and Fig. 2.3). The properties of the objective lens determine a number of important characteristics of the microscope imaging system. Modern objectives are marvels of engineering—they are precisely tuned to correct for nearly all lens aberrations. Unlike the objective lens shown in Fig. 2.2, modern microscope objectives comprise a series of different lenses (and often other optical elements) that work together to enable the high performance of the objective. The two properties of an objective lens that play the most significant role in this

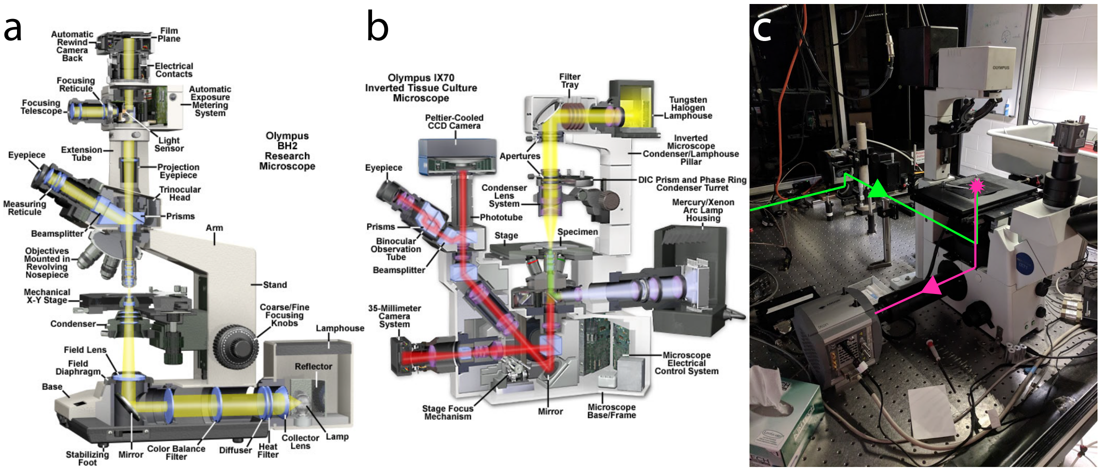

Figure 2.3: Example microscope configurations. (a) The Olympus BH2 upright white light microscope [38]. (b) The Olympus IX70 inverted fluorescence microscope [39]. (c) The Olympus IX71 inverted fluorescence microscope in its natural habitat (laser and fluorescent light path drawn for clarity). a & b Copyright ©Olympus Corporation.

thesis are the magnification and the numerical aperture. The magnification, M, is straightforward to understand: it is the ratio of the length of an object in the imaging plane, l_I, to the length of that same object in the object plane, l_O, giving $M = l_I / l_O$.

An essential property of an objective lens is the numerical aperture (NA). The NA is a dimensionless measure of the range of angles that an objective lens (or any optical system) can emit into or collect light from. The NA is defined as

$$NA = n \sin\theta \tag{2.1}$$

where n is the refractive index of the medium around the lens and θ is the half-angle of the cone of collection (or maximal half-angle for an emissive cone) for the objective lens. Increasing the NA of the objective lens means more light can be collected; and as described in the next section, increasing the NA increases the resolution of the imaging system.

2.1.2 The Diffraction Limit

Consider a point source of optical radiation: a light emitter that is infinitesimal in size. All real light emitters have some actual spatial extent, though many are small enough compared with the wavelength of the light they emit that they may be considered a true point source. Fluorescent molecules, quantum dots, and atoms, are all more than two orders of magnitude smaller than the wavelength of visible light, and thus can very confidently be treated as true point sources—which I will do for the remainder of this discussion.

A point source is spatially a delta function, and thus its Fourier transform shows that it contains all spatial frequencies. By seeing how various spatial frequencies (wavevectors) are filtered out (as this filtering is usually undesirable, it is equivalent to say that these frequencies are *lost*), we can see how an optical imaging system develops a point spread function (PSF) [40]. The usual filtering of the highest spatial frequencies associated with radiation (traveling waves) applies: the near field wavevectors are not radiated and thus do not make it to the detector in the far field, away from the point source[1].

Another typical filtering occurs due to the imaging system having a finite NA. By not capturing the radiation emitted at all angles (as would be the case for $NA = \infty$), a subset of the radiation spatial frequencies from the point source are not detected. All of this filtering occurs even in a totally lossless ideal (though finite) imaging system. Further (realistic) losses to undesired absorptions, reflections, aberrations, etc., can compound the effect, causing additional spatial frequencies to be lost.

As a result of these losses, the optical field that reaches the detector no longer contains an infinite spectrum of spatial frequencies, and thus when transformed back into an image, the detected light does not reproduce the spatial delta function of the point source. The true profile of the point source is spread out when imaged—the image appears to have a finite spatial extent, even though the source has an infinitesimal spatial extent. When

---

[1] Near field microscopy avoids this filtering by placing the detector, or equivalently an optical element (such as a fiber tip) capable of coupling to these wavevectors, in the near field.

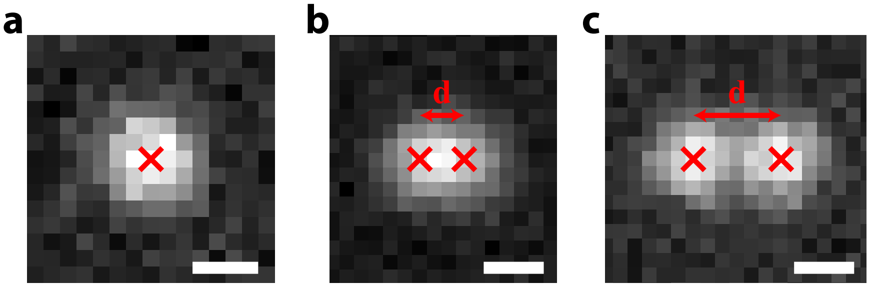

Figure 2.4: Realistic diffraction-limited images of point sources. These images contain moderate shot noise (Poissonian noise), which is usually the dominant noise source in low-light experiments. (a) A single point source located located at the red X. (b) Two point sources separated by a distance d less than the diffraction limit. (c) Two point sources separated by a distance d greater than the diffraction limit. Scale bars: 200 μm.

diffraction of the emitted radiation is the fundamental cause of the described wavevector loss, such a system is referred to as a diffraction-limited imaging system.

Consider imaging a point source with a pixelated detection system. If the imaging system was *not* diffraction-limited, we would expect a single pixel (down to the size of the point emitter) to contain the image of the point source. However, in a diffraction-limited imaging system, as shown in Fig. 2.4a, the image of the point source gets spread out, showing an image of the system PSF.

If two point sources are very close together, their PSFs may overlap. This is the case in Fig. 2.4b,c. If there is significant overlap, as in Fig. 2.4b, it can be difficult or even impossible to determine if there are multiple point emitters there and where exactly they are. This limitation was realized quite early on in the development of optical sciences and technology [41], and those early scientists described what they believed was a lower limit on how close together two point emitters could be and still be distinguished from each other. A popular formulation is Abbe's limit [42, 43], first described in the late 19th century [41], which states that the lower limit two point sources can be separated by is a distance d which is given by the ratio of the emitted wavelength to twice the system NA:

$$d = \frac{\lambda}{2NA} \tag{2.2}$$

Eq. 2.2 is typically referred to as the diffraction limit[2]. Because the two point sources in Fig. 2.4b are separated by less than the system d it might be impossible to distinguish them as two separate emitters. Whereas the point sources shown in Fig. 2.4c are separated by a distance greater than system d, therefore they can be successfully distinguished.

Modern objective lenses can have very high numerical apertures. Cutting-edge oil-immersion objectives are approaching $NA \approx 1.5$, meaning that the diffraction limit is not such an impediment for many imaging tasks. At the visible wavelength $\lambda = 500$ nm, Eq. 2.2 gives $d \approx 166$ nm. This quite small length indicates good resolution, meaning that optical microscopy, even encumbered by the diffraction limit, is a powerful tool for studying very small objects down to the scale of a few hundred nanometers.

For the intervening century or so after the discovery of the diffraction limit, this distance was believed to be a fundamental limit on the obtainable information from an imaging system [40, 44]. As discussed in Sec. 2.4, this assumption turned out to not be quite correct. Modern techniques have not removed diffraction effects from standard imaging systems, but we have developed a number of approaches to obtain information from diffraction-limited systems at length scales smaller than the diffraction limit.

2.1.3 Why Optical Microscopy?

Optical microscopy is a ubiquitous technique used throughout all of science, engineering, and medicine. It is also a very old technique: the first compound microscopes were already being developed as far back as the 16th century [45]. In the intervening centuries (though mostly in the 20th and 21st), many new forms of microscopy—based, for instance, on imaging with electrons, or physical contact—have been developed that have opened up all new insights and directions for research and development, some capable of answering questions that optical microscopes cannot. Yet, even after all of this time and

---

[2] There are other popular variations on what is considered discernible. Two well known examples are Rayleigh's condition, which is more liberal, replacing the 2 with 1.64, and Sparrow's condition, which is more conservative, replacing the 2 with 2.13 [43, 44].

an ever growing numbers of alternative techniques developed, optical microscopy is still extensively used to address diverse questions in myriad fields. Before getting into why optical microscopy is still the most prevalent technique, I will briefly mention some of the strengths and weaknesses of alternative microscopy techniques.

The basic principles behind electron microscopy are extremely similar to optical microscopy, except that the photons in an optical microscope are replaced by electrons. An electron source, like a light source in an optical microscope, produces a beam of electrons which either scatter (elastically or inelastically[3]) or transmit through the object being imaged, exactly like a light microscope. Eq. 2.2 still applies, and by recalling the de Broglie relationship, that the wavelength, λ, of a particle is the ratio of Plank's constant, h, to its momentum, p, $\lambda = h/p$, we see that electrons, which can have very high momentum, can in principle achieve very short wavelengths. Therefore, according to Eq. 2.2, an electron microscope can have a very small resolution[4]. Due to this excellent resolution, electron microscopes can resolve objects down to the atomic level. There are a number of different types of electron microscopes, in this thesis I have mainly used the scanning electron microscope (SEM) variety.

The biggest limitation of an electron microscope is that the sample must be under vacuum to be imaged. This precludes a wide variety of samples from being imaged, importantly, living samples cannot be imaged in an electron microscope[5]. Another major limitation is that unless samples are conducting, or covered with a conducting material, electrons tend to build up on the sample or substrate surface, and through Coulombic effects progressively degrade further imaging, restricting the samples and preparations that can be investigated.

---

[3] For example as in cathodoluminescence microscopy, where an electron beam excites optical luminescence from an object.

[4] Electron microscopes do not actually achieve this diffraction limit, instead significant aberrations in the electron lenses limit the resolution.

[5] This is actually a very active area of current research, with some groups developing creative approaches to try and overcome this barrier. It is however still controversial if anyone has yet succeeded, or that is even possible [46–48].

Using the same basic idea as an electron microscope, newly developed ion microscopes are capable of imaging with sub-nanometer resolution [49]. In ion microscopes the electrons are replaced by some other charged particle, helium for example is the most common choice. Though ion microscopes have their own strengths and weaknesses as compared to electron microscopes, similar limitations apply. Unlike electron microscopes or ion microscopes, optical microscopes can image virtually any sample, and usually do so without causing much or any sample destruction.

Another popular and very powerful advanced microscopy technique is atomic force microscopy (AFM). The most straightforward AFM technique, contact-mode AFM, functions by touching the sample surface with an ultrasharp tip and recording the physical profile of the sample. Like electron microscopes, AFMs can achieve extremely small resolutions, well below the optical diffraction limit. The major limitations of an AFM are mainly practical. AFMs cannot map out a high dynamic range of heights, and further struggle with fast changes in height, like a large vertical step. One of the biggest limitations of AFMs are their very slow scanning speed. AFM fundamentally cannot be a widefield imaging technique, and though there is work developing parallel or faster scanning approaches [50], taking an image with an AFM will always require scanning over the sample. AFMs therefore have an inherent tradeoff between resolution and scan time, either take small steps in a scan giving high resolution, but taking a long time, or use larger steps sacrificing resolution for scan speed. Optical microscopes can operate in a wide-field configuration, completely avoiding this limitation. If the optical microscope is configured in a scanning setup (such as with a confocal microscope), the diffraction limit means that moving in steps much smaller than the diffraction limit (like an AFM does to achieve nm resolution) does not give a resolution improvement, and thus scanning optical microscopes can cover much larger areas in much shorter times than an AFM.

Probably the most compelling reason though that optical microscopes are still far more prevalent than other advanced microscopy techniques is the simple pragmatic reasons of cost and ease of use. Optical microscopes are orders of magnitude less expensive than some of these other techniques, such as electron microscopes or an AFMs. The result is that whenever it will suffice, the optical microscope is the preferred technique simply to save money. Similarly, these other advanced microscopy techniques tend to require advanced training and maintenance. Young children regularly use optical microscopes, demonstrating their ease of use. Finally, because optical microscopes are such an old technology and so ubiquitously used and in so many different domains, there is frequently an optical microscopy approach capable of addressing the question a researcher may want to ask. The implication of this situation is that advancing optical microscopy science and technology, as is one of the aims of this thesis, can have a large impact due to the ever increasing number of researchers and fields making use of the technique.

2.2 Fluorescence

Fluorescence is a type of luminescence. It is a mechanism by which an excited state can relax in energy by emitting light. To begin our discussion of fluorescence we consider the simplified Jabłoński diagram appropriate for typical fluorescent molecules in solution, shown in Fig. 2.5. To begin, the molecule is not excited and the electron is in the singlet ground state, S_0. If the molecule is excited, the electron follows the excitation path, *ex*, to the higher energy excited states. Excitation can occur through a number of different processes, but for the purposes of this thesis, we will focus on excitation caused by the molecule absorbing a high(er) energy photon. For instance, the path colors in Fig. 2.5 indicate that this molecule absorbed a green photon (energy ≈ 2.35 eV). The electron gets excited to a high vibrational energy level in the singlet excited state, S_1 indicated by the top of the green arrow. It then very quickly, on a timescale of 10^{-12} s (non-radiatively) relaxes to the lowest energy vibrational level of S_1; this thermal relaxation is indicated by the gray arrow starting at the level of the top of the green arrow. Because typical fluorescence emission timescales are closer to 10^{-9} s, the electron nearly always makes it to the

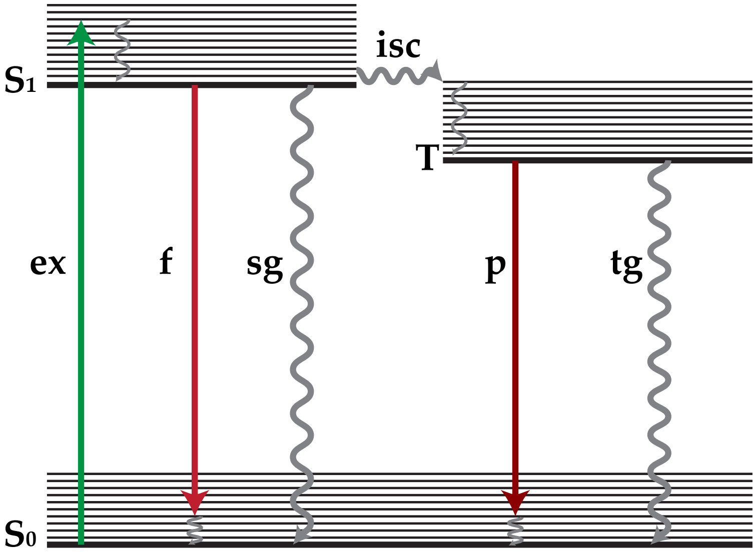

Figure 2.5: A simplified Jabłoński diagram. Labeled states are: S_0, singlet ground state, S_1, singlet excited state, T, triplet excited state. Labeled paths are: *ex*, excitation (usually an absorbed photon), f, fluorescence, *sg*, singlet-to-ground non-radiative relaxation, *isc*, inter-system crossing, p, phosphorescence, *tg*, triplet-to-ground non-radiative relaxation.

lowest energy vibrational state (i.e., it reaches thermal equilibrium) before relaxing to a lower energy electronic state [51].

Once the electron has reached the lowest energy vibrational level in S_1, it can relax further in energy through a number of different paths. Fluorescence is the relaxation of an excited electron from an excited singlet state to a lower energy singlet state through the emission of a photon, equal to the electron energy difference. Fluorescence is is the red path, f, in Fig. 2.5. This radiative emission, occurs when the molecule relaxes by emitting a radiative photon. Because the electron has lost energy by thermally equilibrating, the energy of the photon emitted is lower than the energy of the photon absorbed. For instance, if this molecule absorbed a green photon at 2.35 eV, it might emit a red photon at 1.95 eV. This redshifting of emission is called a Stokes shift. The electron could also relax non-radiatively, most likely by dissipating energy through heat. This singlet-to-ground non-radiative relaxation path is labeled *sg* in Fig. 2.5.

Molecules in the excited state S_1 can also partially relax by transitioning to a triplet state, labeled T in Fig. 2.5. Transition to the triplet state usually occurs through a spin conversion called intersystem crossing, labeled *isc*. Transition directly from $T \longrightarrow S_0$ is a forbidden transition, which in a realistic system, doesn't mean a probability of zero, but rather that the rate for this transition is several orders of magnitude slower than for fluorescence [51]. The electron in T can either relax non-radiatively, *tg*, triplet-to-ground non-radiative relaxation, through dissipating heat, or it can relax through a radiative process, called phosphorescence, *p*. Because intersystem crossing must occur from a higher to a lower energy level, and because further vibrational relaxation subsequently occurs, phosphorescence is further red-shifted from the excitation photon energy.

We can use this granular understanding of the Jabłoński diagram to pull out a number of important features of fluorescence. Fluorescence quantum yield, η, is the ratio of the number of emitted fluorescent photons to the number of absorbed photons. The quantum yield can equivalently be expressed as the ratio of the probability of fluorescence to the probability of all processes. Because something will occur (the electron won't stay in the excited state indefinitely), the probability of all processes (the denominator of the ratio) is 1, so

$$\eta = P(f) \tag{2.3}$$

It is instructive to write out the details of the denominator. Because the possible decay pathways is dependent on the starting state (e.g., the probability of fluorescence is 0 if the electron is in the triplet state), we need to utilize conditional probabilities, where $P(a|b)$ means the probability of a given the condition b. This gives

$$\eta = \frac{P(f|S_1)}{P(f|S_1) + P(sg|S_1) + P(isc|S_1)\left(P(p|T) + P(tg|T)\right)} \tag{2.4}$$

However because we assume that excitation is occurring when calculating the fluorescence quantum yield, we can simplify this to

$$\eta = \frac{P(f)}{P(f) + P(sg) + P(isc)\,(P(p|T) + P(tg|T))} \tag{2.5}$$

where

$$P(f) + P(sg) + P(isc)\,(P(p|T) + P(tg|T)) = 1 \quad \& \quad P(p|T) + P(tg|T) = 1 \tag{2.6}$$

Because $P(isc) \ll P(f) + P(sg)$, Eq. 2.5 is frequently approximated as

$$\eta = \frac{P(f)}{P(f) + P(sg)} \tag{2.7}$$

The probability of any of these events can be described by the experimentally measurable quantity of rate, which is probability per time. Given a radiative decay rate, Γ_R, and a non-radiative decay rate, Γ_{NR}, we can write the quantum yield in its typical formulation as

$$\eta = \frac{\Gamma_R}{\Gamma_R + \Gamma_{NR}} \tag{2.8}$$

The next aspect of fluorescence that is immediately obvious from inspecting Fig. 2.5 is some typical characteristics of fluorescence spectra. As was previously mentioned, because the molecule relaxes vibrationally before relaxing electronically, there is a Stokes shift such that some of the excitation photon energy is lost, resulting in a lower energy (red-shifted) emission photon energy. The Stokes shift is readily apparent Fig. 2.6, which shows a typical excitation and emission fluorescence spectra.

Prior to excitation, the molecule is not always in the lowest energy vibrational state in S_0, mainly due to thermal fluctuations, the electron could be in any one of the many closely spaced vibrational levels in the ground state (the occupation probability is given by the Boltzmann distribution). Similarly, upon excitation, the molecule can go into higher vibrational levels in S_1. Because the excited state also has many populated vibrational

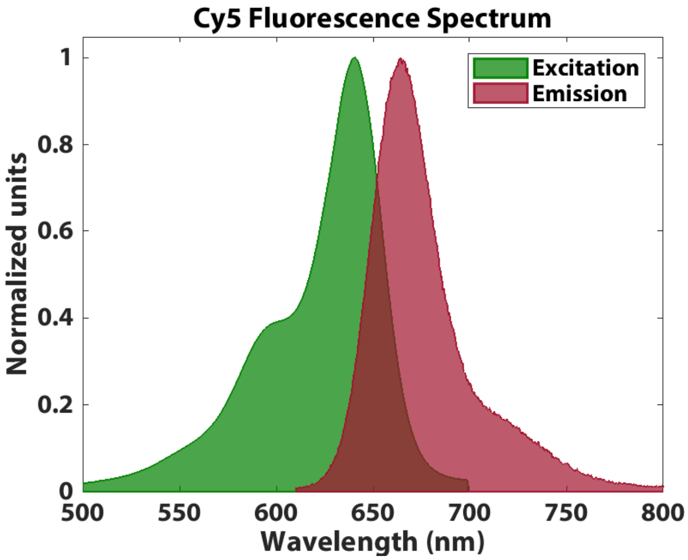

Figure 2.6: Cy5 Fluorescence Spectrum. Excitation (absorption) in green and emission in red.

levels, the result is that, there is nearly a continuous distribution of possible energy differences for the excitation process[6]. The result is that the excitation spectrum for a fluorescent molecule is fairly broad at room temperature, as shown in Fig. 2.6. Because the vibrational level spacing in the ground state and the excited state tend to be very similar, the reverse of this process occurs for emission, and excitation and emission sprectra for a given molecule tend to mirror each other [51].

Finally, Fig. 2.5 invites a preliminary discussion of blinking and bleaching. Throughout this thesis, I will assume fluorescent molecules are far from any saturation regime. Here, saturation means that the molecule can no longer absorb any further photons until it relaxes. This is a very good assumption for the experiments and science discussed here. One could potentially enter a saturation regime by exciting with high-power lasers, which we are careful to not do. Part of why we do not saturate these molecules is due to their fast fluorescence decay rates. For a typical fluorescent molecule, the fluorescence lifetime is relatively short, a typical lifetime is on the order of 10^{-9} s. The result of this is that

---

[6] For simplicity, I am leaving inhomogenous broadening out of this discussion, even though it is an important effect influencing the shape fluorescence spectra.

a continuously excited fluorescent molecule, for example with a continuous-wave (CW) laser, tends to continuously fluoresce.

The exception from this continuous fluorescence, is when the molecule undergoes intersystem crossing into T. Here, because the transition from $T \rightarrow S_0$ is forbidden, the molecule may stay in T for a very long time—typical phosphorescence lifetimes range from μs to ms. During the time in T, the molecule is not fluorescing. Eventually the molecule may undergo the forbidden transition back to S_0, and it can start fluorescing normally again. This reversible, aperiodic, on/off switching is the phenomenon of blinking. Relatedly, for reasons still debated [51,52], when the molecule is in T, it is susceptible to undergo chemical and physical changes that prevent the molecule from further fluorescing. This irreversible turn-off is the phenomenon of photobleaching.

2.3 Single-Molecule Imaging

Thus far we have seen that microscopy is both a widely used, and an incredibly useful, technique for imaging small features. Even when able to image at such small length scales, there is still a question of specificity, that is, determining what exactly is being imaged. This is the general idea behind various kinds of histological staining, to use color to create contrast, to help distinguish different structures or populations from each other. Taking this idea to the next level, scientists developed fluorescence tagging schemes to label various molecules of interest to let them image only the population of those particular molecules, even in crowded environments [53]. Therefore fluorescence microscopy allows scientists to study small features with incredibly high specificity.

The ultimate limit of specificity is imaging individual molecules. The first optical detection of single molecules in dense media occurred in 1989 through absorption [54] and shortly afterwards in 1990 by fluorescence [55]. The realization that it was feasible to optically study individual molecules, quickly opened the door to whole new areas of inquiry and fields of study [56]. With this ultimate level of specificity, sample heterogeneity

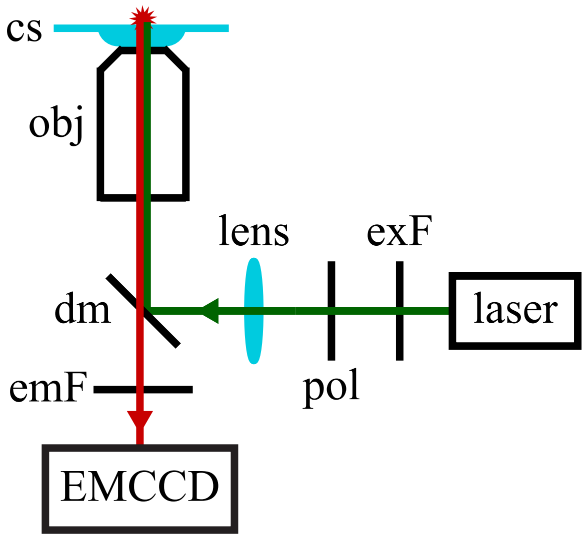

Figure 2.7: Basic wide-field epifluorescence light path. Labels are: exF, excitation filter; pol, polarizing optics; emF, emission filter; dm, dichroic mirror; obj, objective lens; cs, coverslip. Not drawn to scale.

could be understood. Early efforts were able to uncover troves of new insights into single molecules [57–59].

2.3.1 Single-Molecule Tools

Modern single-molecule imaging techniques look very different than the early experients optically detecting single molecules. In the remainder of this section, I will give a brief overview of the tools and techniques that allow us to, relatively easily, image a wide variety of single molecules. There are many different approaches to single-molecule imaging, each with their individual strengths and weaknesses [60]. As an illustrative example, my general single-molecules fluorescence experimental setup is shown in Fig. 2.7. Some of the tools necessary to image single molecules are newly developed and still being refined, such as high-NA objectives, which have significantly improved our ability to image single molecules. Others are older and fairly unchanged, for instance, functionally, lasers have been good enough for these experiments for many decades—indeed cutting-edge laser technology, like ultrafast pulsed systems, are not required.

Though a realistic single-molecule imaging experiment will have far more components than are shown in Fig. 2.7 (see for example my setup shown in Fig. 2.3c), these are the essential components that are fairly unchanged between different setups. Fig. 2.7 shows a wide-field epifluorescence setup, which means that an entire image is detected simultaneously and the same objective lens is used to excite the sample and detect its emission. There are many other approaches for imaging or detecting single molecules, a common alternative is a confocal setup, which removes the lens before the objective and adds a pinhole spatial filter in the detection path, the rest is essentially unchanged[7].

No single component is the lone key to being able to image single molecules, but rather it is the setup as a whole which enables this. That being acknowledged, possibly the most important component is the objective lens. Modern objective lenses can have extremely high NAs. This is usually achieved by using oil-immersion objectives. As depicted in Fig. 2.7, a drop of microscope oil is placed between the objective and the sample coverslip, made of glass. Importantly, the refractive index of the oil is matched to the objective and the coverslip. This has two basic functions, the first effect is that by reducing any index mismatches between the lens, a possible air gap, and the coverslip, unwanted interfacial reflections are eliminated. Secondly, the most important reason to use immersion oil, is that it increases the NA of the lens. Recall Eq. 2.1, $NA = n \sin \theta$. If n was limited to that of air for an air gap, the maximum NA possible would be $NA = 1$, however by eliminating the air gap, and having all components at $n = 1.515$ the NA can be increased toward the theoretical upper limit of $NA = n = 1.515$ (for a single objective). Single molecules tend to be fairly dim because they don't emit many photons before photobleaching. This is the main reason it took so long to first image them. By having a high NA objective, a large fraction of the emitted light from single molecules can be collected, and thus they are detected as brighter, this is an integral part of imaging single molecules.

Single-molecule fluorescence is relatively easy to detect (as compared with absorption, Raman, etc.) due to the large Stokes shift in emission. However, due the low photon

---

[7] In a confocal setup a single detection element is used (e.g., single photodiode) as opposed to an array of detection elements, like in an EMCCD.

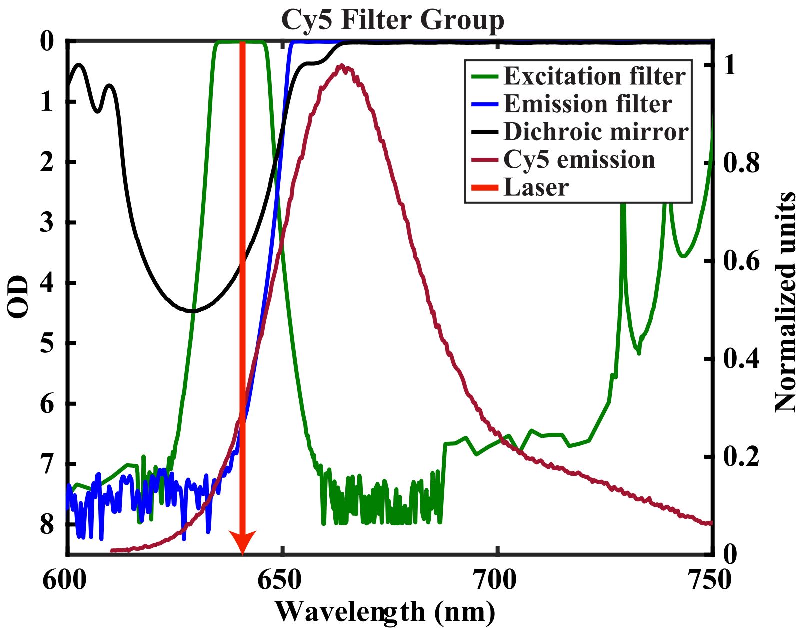

Figure 2.8: Cy5 filter group. The OD of the filters are shown on the left axis and the fluorescence spectrum of Cy5 is shown on the right axis. Filter data from Copyright ©Semrock, Inc.

budget of single molecules, without sufficient filtering, the laser light used to excite the fluorescent molecules would completely swamp out any fluorescent light. It is therefore critical to filter out the excitation laser light. The first step in this process is ensuring that the laser light is highly monochromatic. Ideal lasers are entirely monochromatic, but realistic lasers, especially inexpensive diode lasers, have non-trivial bandwidths and more problematically, broadband backgrounds, for instance from laser media intrinsic photoluminescence (PL). Thus, the first component necessary to ensure appropriate filtering is the laser itself, which must be fairly monochromatic. Secondly, to help ensure the monochromaticity of the source, and to filter out any potentially weak PL, a bandpass (or possibly shortpass) filter is used (exF in Fig. 2.7).

The monochromatic laser light excites fluorescence in the sample and the high NA objective captures the fluorescence and scattered laser light from the sample and coverslip. The first filter that both of these light paths pass through is a dichroic mirror (dm in Fig. 2.7). A fluorescence dichroic mirror is a reflecting longpass filter, with the passband edge slightly redder than the laser light. The dichroic mirror reflects the laser light twice: first it directs the laser to the sample in the excitation path, and second it reflects any elastically scattered laser light away from the detector in the detection path. In this way, it prevents laser light from reaching the detector. Then after the dichroic mirror is a second long-pass filter, called the emission filter (emF in Fig. 2.7). Because this filter doesn't need to function as a mirror, it can reject a much higher proportion of the laser light.

Take the example shown in Fig. 2.8, which is a possible filter group for the fluorescent dye Cy5, whose excitation and emission spectra were previously shown in Fig. 2.6. An excitation filter bandpasses the laser, in this case a 640 nm laser, ensuring that any broadband PL from the laser is filtered out. In the detection path, first a dichroic mirror filters out any elastically scattered laser light, in this case with optical density (OD)[8] of $OD \approx 4$. Next, an emission filter further blocks any laser light, in this case with $OD \approx 6$. The combined filtering is $OD \approx 10$, resulting in the scattered laser power being reduced by 10^{10} before reaching the detector. Furthermore, the desired fluorescence emitted by Cy5 is minimally filtered, in this case the emission filter and dichroic reach $OD \approx 0$ for all light redder than ≈ 670 nm, which is near the emission peak of Cy5. Without such intense filtering of the laser light and minimal filtering of the fluorescence, imaging single molecules would be nearly impossible.

Even with the best filters and a high NA objective, the reality is that single molecules are dim. It is therefore imperative to use a very sensitive detector. For widefield imaging experiments, a standard choice is the electron multiplying charge-coupled device (EMCCD) camera. EMCCD cameras are modified CCD cameras that have an amplifying gain built-in. The result is that EMCCDs can achieve very high sensitivity at reasonable imaging speeds (up to $\approx$ 30fps is still reasonable to image single molecules). The quantum efficiency, defined as the ratio of recorded counts to photons incident on the detector, of EMCCDs is extremely high ($> 90\%$ across most of the visible spectrum). Fi-

---

[8] OD is the $\log_{10}$ of the ratio of the power transmitted, P_T, to the incident power, P_0, $OD = \log_{10}(P_T/P_0)$.

nally, EMCCDs are an excellent choice because they have very low readout noise and dark counts, ensuring that the signal-to-noise ratio (SNR) remains as high as possible. Recently, an alternative to EMCCDs has appeared, the scientific complementary metal-oxide-semiconductor (sCMOS) camera. sCOMS cameras aren't as quite sensitive as EMCCDS, with quantum efficiencies closer to 60%, but they do have similarly low (or even better) levels of noise, and tend to be less expensive than EMCCDs. The main advantage of sCMOS cameras is they can image at faster speeds, with 100 fps being a reasonable speed to image single molecules.

An important set of component, though frequently overlooked, in single-molecule experiments are the polarizing optics. Nearly all fluorescent molecules are mainly dipolar absorbers (and emitters), meaning they absorb incident light like a dipole. Dipoles are strongly polarized. If the incident laser light is polarized perpendicular to the molecule absorption dipole then it will absorb very little of that incident optical energy and thus not fluoresce. Because fluorophore orientation is not precisely fixed in most experiments, in order to efficiently excite as many molecules as possible, circularly polarized light is used. Beyond this consideration, many experiments may require further control over the polarization for myriad reasons. For instance, in Chap. VII, I specifically studied the effect of the excitation polarization on fluorescent molecules coupled a plasmonic optical antenna. Another possible reason to control the polarization is to use it as a further filter (i.e., putting a crossed polarizer in the detection path).

2.3.2 Single-Molecule Techniques

Even with the most sensitive and carefully constructed imaging setup, if the density of emitting molecules is too high then their PSFs will overlap and it can be difficult or even impossible to measure individual single molecules. This limitation is essentially a reiteration of the diffraction limit. Therefore, techniques are needed which can keep the density of emitting molecules low (tautologically referred to as single-molecule densities), while keeping the density of total molecules much higher so that the experiment can reveal statistically useful information about the system under interrogation. Though there is an ever growing list of techniques (usually with accompanying colorful acronym), in this section I will focus here on the three main approaches, from which most (though not all) other techniques are derived.

The first technique, which is the main technique used in this thesis, is points accumulation for imaging in nanoscale topography (PAINT) [61]. PAINT is mainly used to interrogate surfaces. In PAINT, a low concentration (typically tens of nM) of dye molecules are diffusing in solution above the surface under investigation. As they diffuse, they move far too fast to be imaged above the background noise. Instead, occasionally a molecule will adsorb on the surface. While adsorbed the molecule remains still enough to be imaged as a single molecule. The molecule then desorbs or bleaches. By tuning the solution concentration, bleach rate (via the laser power), and surface chemistry (or alternatively the molecule functionalization), the density of emitting molecules on the surface can be adjusted to achieve single-molecule densities. Because adsorption is a stochastic process, the entire surface will eventually be uniformly and randomly interrogated by adsorption events.

Another widely used technique is photoactivated localization microscopy (PALM) [62, 63]. PALM is an especially popular technique for imaging inside cells because PALM relies on the use of photoactivatable fluorescent molecules (usually fluorescent proteins) which are attached to some other molecule under investigation. Photoactivatable means that the molecule can only fluoresce if it is first activated. Photoactivation is accomplished by using a separate activation laser than the fluorescence excitation laser. By illuminating for a short time with a low activation power, only a small subset of the total molecules are activated. Then when excited with the fluorescence excitation beam, a low density of emitting molecules can be achieved.

Finally, one of the most popular and widely applied techniques for single-molecule

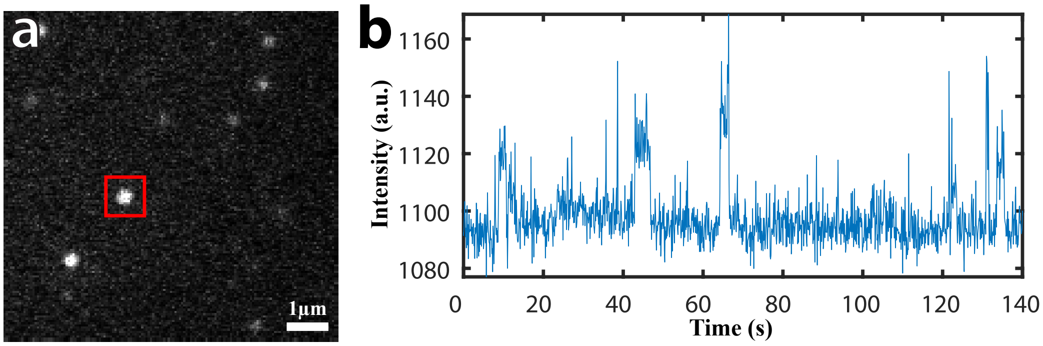

Figure 2.9: Representative time trace of a single molecule's fluorescence. (a) A representative frame from a single-molecule imaging movie. (b) Time trace of the mean intensity in the red box over the course of the movie showing digital blinking/bleaching steps.

super-resolution imaging is stochastic optical reconstruction microscopy (STORM) [64]. In STORM, the stochastic blinking of the fluorescent molecules is the key to achieving a low density of emitting molecules. Either by using a molecule with an intrinsically high blinking rate, or inducing an artificially high blinking rate (usually chemically), the molecules can be kept in an off state most of the time, and stochastically turn on to be detected. Tuning the blinking rate, optically or chemically, is the main tuning mechanism of a STORM experiment.

2.3.3 Actually Measuring Single Molecules

A question single-molecule researchers often get from reviewers or colleagues outside the field is how we are sure that we are actually measuring single molecules. Given how difficult it is to image single molecules, this is not an unreasonable question. There are two broad categories of evidence to support the claim of actually measuring single molecules.

The first is that experiments are conducted with a very low density of emitters—called single-molecule densities. As discussed in Sec. 2.3.2, there are many different methods to achieve this low density of on emitters (on meaning actively fluorescing). It is a fairly straightforward argument, that if images are mostly made up of pixels not containing molecules, for instance in the representative frame shown in Fig. 2.9a, then it should follow that multiple molecules appearing at the same time and place is a low probability (though not zero probability) event.

The second category of evidence is abductive: because measured single-molecules have properties that we would expect from single molecules, they probably are single molecules. This includes weak evidence like the image size and shape matching the system PSF. It also includes stronger evidence like molecules not being outliers from the distribution of all other measured molecules in the experiment for whatever property is being compared (brightness, speed, etc). Finally, the strongest evidence is that single molecules should display digital blinking/bleaching, meaning that they should be on with a given intensity value, then upon blinking off or bleaching, the intensity goes back to the background level. If multiple molecules were overlapping, for instance, we would see multiple blinking/bleaching steps. An example time trace of single-molecule fluorescence is shown in Fig. 2.9b, where such digital blinking/bleaching is clearly evident.

2.4 Single-Molecule Super-Resolution Microscopy

We have now seen that it is possible to reliably image single molecules using a variety of different tools and techniques. In this section, I will focus on one of the main payoffs of imaging single molecules, that by doing so in conjunction with numerical image analysis allows molecules to be localized with precision well below the diffraction limit. This localization microscopy approach, single-molecule super-resolution microscopy, has revolutionized microscopy and in particular cellular-biomedicine [1–6].

2.4.1 Super-Resolving Emitters

We know the functional form of a microscope's PSF. For a microscope imaging through a circular aperture (finite cylindrically symmetric objective lenses create such an aperture), the functional form of the PSF is an Airy disk [44]. The intensity profile of an Airy

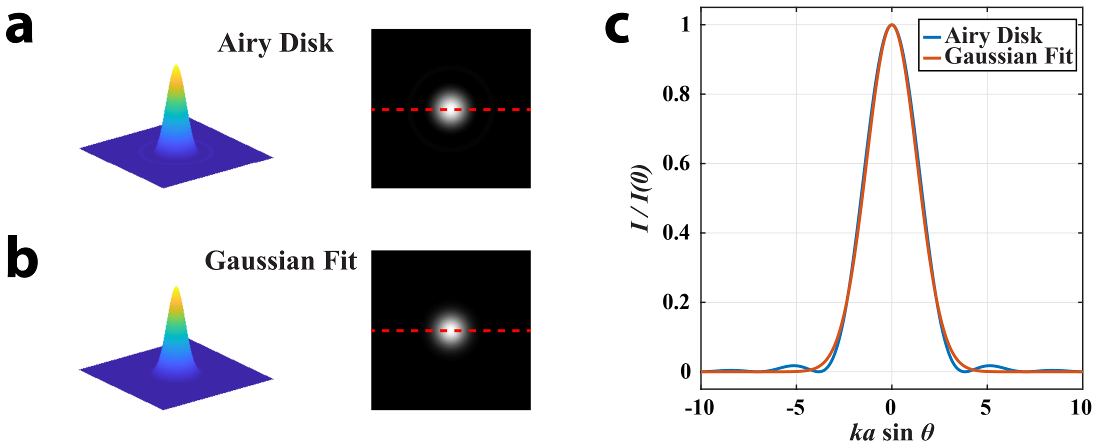

Figure 2.10: 2D Gaussian fit of an Airy disk. (a) Intensity surface and grayscale image of an Airy Disk. (b) Intensity surface and grayscale image a 2D Gaussian fit to the Airy disk in a. (c) Cross-sections of the Airy disk in a and its Gaussian fit in b, through the center indicated by the dashed red line.

disk is given by

$$I(\theta) = I(0)\left(\frac{2J_1(ka\sin\theta)}{ka\sin\theta}\right)^2 \tag{2.9}$$

Where $I(0)$ is an amplitude factor, J_1 is is the Bessel function of the first kind of order one, k is the wavenumber ($k = 2\pi/\lambda$), a is the aperture radius, and θ is the angle of observation. Note that $ka\sin\theta$ is effectively a radial coordinate. For convenience, we approximate the Airy disk by a 2D Gaussian function to implement PSF fitting algorithms,

$$I(x,y) = I(0)e^{-\frac{(x-x_0)^2}{2\sigma_x^2}-\frac{(y-y_0)^2}{2\sigma_y^2}} \tag{2.10}$$

where x_0 and y_0 are the x and y coordinates of the center of the Gaussian respectively, and σ_x and σ_y are the x and y widths[9] of the Gaussian respectively. An Airy disk and its 2D Gaussian fit are shown in Fig. 2.10. The first thing to note is that the approximation is extremely good. Without a very careful inspection, Fig. 2.10 a & b look identical. Secondly, due to the symmetric nature of the rings of the Airy disk, a Gaussian fit won't have

---

[9] Referencing a normal distribution (same functional form), I and many others frequently refer to σ as the standard deviation of the Gaussian. It is also important to note that, though Eq. 2.9 is for a circularly symmetric aperture, asymmetric apertures have similar (though asymmetric) diffraction patterns. This asymmetry is why Eq. 2.10 has distinct x and y widths.

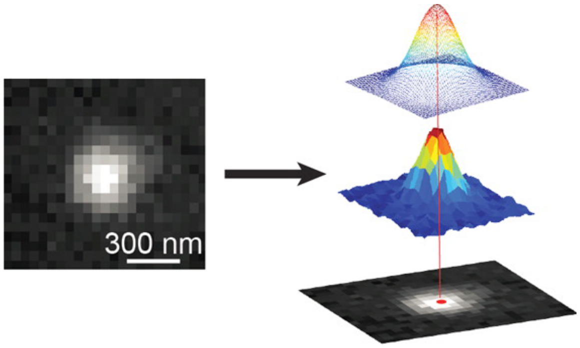

Figure 2.11: Schematic of super-resolution PSF fitting. A 2D Gaussian is fit to the image of a single molecule. Published in [6], Copyright ©American Chemical Society

any biases in position. Lastly, though the rings are a defining feature of an Airy disk, the brightest ring (first order) is only ≈ 2% of the central peak intensity and therefore not detectable in this regime, further demonstrating that a Gaussian is an excellent approximation. In a realistic single-molecule imaging experiment with a finite (and often small) SNR, unlike the noiseless representation shown in Fig. 2.10, the distinction between an Airy disk and 2D Gaussian becomes nearly meaningless.

To localize a point emitter with super-resolution precision, the image of that point emitter is fit to a 2D Gaussian function. This PSF fitting is demonstrated in Fig. 2.11 for a realisitic (noisy) image of a single molecule. PSF fitting the image of a single molecule in which N photons were detected can be viewed as doing N measurements of the molecule, with the position uncertainty of those measurements given by the PSF width [1,65]. By effectively repeating this position measurement N times the molecule can be localized with extremely high precision, far below the diffraction limit. The precision of this localization Δx (as in $x + \Delta x$), is derived in [65], which calculates

$$\langle(\Delta x)^2\rangle = \frac{\sigma^2 + a^2/12}{N} + \frac{8\pi\sigma^4 b^2}{a^2 N^2} \tag{2.11}$$

where σ is the standard deviation of the PSF (as defined above, but now for a symmetric 2D Gaussian), a is the side length of a pixel, and b is the standard deviation of the background noise. It is important to note that in [65] they break the measurement noise into two categories, the first is photon-counting noise which arises in any low-light measurement; this noise follows a Poissonian distribution (shot noise) and is thus related to the number of photons N. They then include all other noise sources in the term b, which for an EMCCD is typically dominated by readout noise and dark counts. If the overall noise is dominated by background noise then the precision scales as $1/N$ and if it is dominated by shot noise then the precision scales like $1/\sqrt{N}$ [65]. Regardless of the exact scaling, having brighter emitters means that they can be super-resolved with higher precision.

In the visible, for instance, at an emission wavelength of 570 nm (the peak emission wavelength of Cy3), with an $NA = 1.45$, Eq. 2.2 gives a diffraction limit size of $d = 196.5$ nm. However, using super-resolution PSF fitting, in 2003 Yildiz et al. [66] were able to achieve a localization precision of 1.5 nm, beating the diffraction limit by two orders of magnitude. Even in noisy live-cell imaging experiments resolutions on the order of tens of nm can regularly be achieved [6].

It is difficult to overstate the impact that single-molecule super-resolution microscopy has had. This technique has revolutionized cellular biomedicine and has begun to impact the physical sciences and engineering. To see some examples of the impact and breadth of this technique, see the reviews published in [7]. Due to the widespread impact super-resolution microscopy has had, the 2014 Nobel Prize in Chemistry was awarded partially for single-molecule super-resolution microscopy and partially for STED super-resolution microscopy (discussed in Sec. 2.5) [4].

2.4.2 The Importance of Algorithms

Single-molecule super-resolution microscopy is a data-heavy field where a large amount of data is collected, needs to be extensively numerically analyzed to do measurements, and then these large numbers of measurements need to be processed to produce useful information. Because the technique analyzes one molecule at a time, in order to make statistically significant inferences for a given measurable, hundreds or thousands of molecules need to be measured. This process needs to be repeated for every condition (dependent variable) under investigation. If the effect under investigation is particularly difficult to measure or a low-probability event, this means that the situation is even worse and better statistics—more measurements—are needed. The result is many layers of careful and efficient data processing algorithms are essential for single-molecule super-resolution microscopy [67–69].

Lee et al. [69] organize the problem of single-molecule data analysis into four problems: 1. the localization problem, 2. the counting problem, 3. the linking problem, and 4. the interpretation problem. In this thesis, I am not directly[10] concerned with #2, the counting problem, which is about distinguishing possibly spatially overlapping molecules from each other. As discussed in Sec. 2.3.3, ensuring that single-molecules are actually being measured is a preliminary check carried out before experiments can proceed, and in the PAINT experiments I present here, not typically further checked in data processing. With this in mind, I propose a modification of their classification, and break the problem down as:

1. The detection problem
2. The measurement problem
3. The interpretation problem

There is an extensive literature on the myriad different approaches to solving these different problems. There is significant overlap between single-molecule researchers and those whose work would have traditionally been housed in statistics or computer science departments. The rise of fields like bioinformatics or biostatistics is emblematic of this trend. For reviews on single-molecule data processing I particularly reccommend [67–69]. I will

---

[10] I say directly, because the SMALL-LABS algorithm I invented, discussed in Chap. V, is likely a powerful tool to address the counting problem. However, this has not been a focus of my work.

not go into detail on these problems, but instead highlight what I view as the essence of the problems, and why they are difficult to solve.

In general, as discussed above, because these datasets tend to be very large, fast and efficient algorithms are required. This highlights both the need for capable computing environments (hardware and software) and carefully constructed algorithms. Furthermore, the number of measurements undertaken here precludes extensive human intervention in the data analysis process. This reality comes with a number of challenges and potential payoffs. Humans (and indeed most animals) are phenomenal at pattern recognition, and it can be difficult to construct algorithms that achieve human-like success rates. It is really only in the last few years that carefully trained AIs utilizing machine learning approaches have begun to overtake humans in certain pattern recognition contests. Though some researchers are making tremendous progress in bringing machine learning to science, it is a fundamental problem in research that we are asking questions that have not been answered yet, and thus training an AI may be difficult. On the flipside, by removing humans from the analysis, the data analysis biases can become more concrete and possibly easier to identify and remedy.

The detection problem describes the difficulty of separating single-molecule signals from the background. Obviously, it is necessary to detect molecules before they can measured[11]. The main challenge here is that SNRs of single-molecule emission tend to be quite small, with an SNR $\gtrsim 2$ being excellent. The result is that detection false positive rates need to be very carefully balanced with false negative rates. This is usually accomplished with a series of detection and filtering steps compounding on each other. A particular difficulty for the detection problem is backgrounds which are not simply homogeneous, but which instead can obscure molecules and preclude detection. This problem was the impetus for my developing the SMALL-LABS algorithm discussed in Chap. V. The detection problem

---

[11] Surprisingly, some techniques and measurements do not explicitly need to localize molecules to measure them. For instance STICS [70] used to measure molecular diffusion [71] still needs to separate the molecular signal from the background, but is agnostic regarding the molecule location.

can also be one of the slowest steps of the data analysis problem as it usually requires the entire movie to be analyzed because in this first step there is not yet any way to exclude the many pixels which carry no useful information (at single-molecule densities it should be the majority of pixels).

The measurement problem is concerned with determining the properties of the detected molecules. One may want to measure seemingly straightforward properties like molecular location, brightness, speed, or direction, or more complex properties, for instance, how the speed of a green molecule changes as it moves relative to a red molecule during a specific stage of cellular mitosis. The measurement problem is not just measuring simple properties, but also includes the kinds of linking discussed in [69], for instance tracking the location of a molecule over the course of a movie is a common procedure [72]. This is difficult to solve primarily due to the complexity of the measurements being undertaken. A single measurement requires many individual steps, and fine tuning every step may be difficult or even impossible.

The interpretation problem is concerned with arranging all the measurements in a meaningful and useful arrangement. The canonical example here in single-molecule super-resolution, is the reconstruction of the locations detected in a super-resolution experiment. In a single-molecule localization experiment, many individual molecules are localized. How best (accurately, usefully, etc.) to reconstruct those localizations into a map of an underlying structure is still an ongoing area of development [68]. More generally, the difficulty of this problem reflects both the large size of datasets and the difficulty of the measurement problem. Visualizing any large dataset is a nontrivial task requiring some clever dimensionality reductions. The complexity of the measurement problem resurfaces here in finding the best way to include that complexity (and not completely discard it) in the interpretation.

Finally, before data analysis problems can be tackled, the data first needs to be recorded. Since single-molecule experiments require large datasets, recording these can be time consuming and/or require frequent precise adjustments. There is increasingly a push to use automated and computer controlled approaches for data collection. Such approaches can potentially increase experiment throughput, measurement quality (especially precision), and repeatability[12]. Some automation is standard, like controlling a grating angle in a spectrometer, or rapidly opening and closing shutters on cameras or lasers. Other tasks are only occasionally automated, like autofocusing or cycling through various dependent variables (stage position, laser wavelength, etc). As algorithms become more complex and computer controlled hardware more ubiquitous, the prevalence of partially or completely unsupervised experiments will continue to increase. I discuss RoboScope, the open-source microscope automation platform I developed, in Sec. 7.1.1.

2.5 Other Super-Resolution Approaches

The 2014 Nobel Prize in Chemistry was awarded "for the development of super-resolved fluorescence microscopy" [4]. In Sec. 2.4 I detailed how single-molecule fluorescence imaging enables super-resolution microscopy—microscopic imaging with a resolution better than the diffraction limit (Sec. 2.1.2). This is not the only approach to super-resolution fluorescence microscopy, the 2014 Nobel prize was also awarded to recognize stimulated emission depletion (STED) microscopy. There are also other fluorescence-based super-resolution techniques, and a wide range of additional super-resolution microscopy techniques. In this section, I will give a brief overview of some of these different techniques.

In STED microscopy, much of the setup is similar to a typical confocal fluoresence experiment, the defining feature is an extra beam in the excitation path [73,74]. The extra beam is called the STED beam. As shown in Fig. 2.12 the STED beam is doughnut-shaped. The STED beam is matched to the frequency of emission (on the blue side of the emission spectrum) of the fluorescent molecules (energy difference between S_1 & S_0) inducing stimulated emission, which in turn suppresses fluorescence (spontaneous emission). The

---

[12] In the context of the so-called "reproducibility crisis," this is especially important.

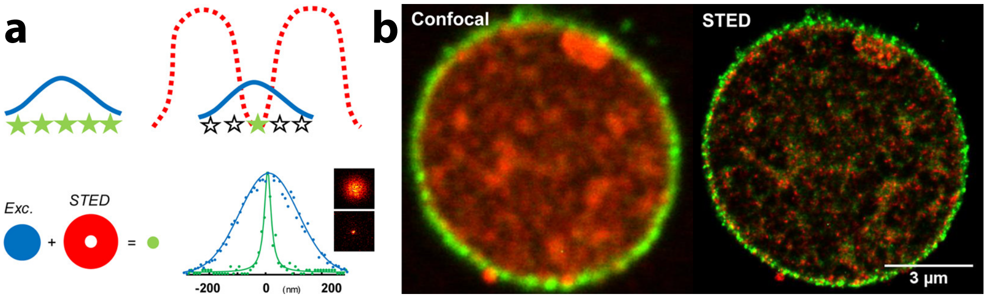

Figure 2.12: Schematic and example of STED microscopy. (a) A diffraction limited intensity profile (blue curve) preclude high precision localization of dense emitters (stars). STED depletes emission outside of the central area allowing super-resolution localization (green curve). (b) Example comparison of diffraciton limited confocal imaging vs. STED imaging of the same cell with two different biomolecules labeled in red and green. Adapted from [74], ©American Chemical Society.

result is that the convolution of the nonlinearities induced by the STED beam and the original fluorescence excitation beam produces an effective fluorescence excitation beam with a PSF much smaller than the diffraction limit of the system. Even though the detection is still diffraction-limited, because the excitation is known to be sub-diffraction, the location of the detected fluorescence is measured with precision well below the diffraction limit, given by the width of the effective excitation beam.

As compared to localization microscopy, STED has a number of advantages and disadvantages. One of the primary disadvantages is that the STED beam itself adds a lot more light energy to the sample and increases concerns about phototoxicity for living samples and range of other destructive effects. A big practical difference between STED and localization microscopy is that STED is necessarily a scanning technique. Therefore the same scanning considerations discussed previously in the context of AFM (Sec. 2.1.3) apply here. Interestingly though, because STED does not require the stochastic turning on of fluorophores as in single-molecule imaging, the amount of time required to image a particular spot is only the imaging integration time, and is not dependent on the rate at which molecules appear. In this way, for certain applications, STED can be a much faster approach. One advantage is that the resolution of a STED experiment is far less dependent on the brightness of the emitters, it is mostly dependent on the excitation optics and alignment. Overall, output from STED is quite similar to single-molecule microscopy, and the two techniques can be used fairly interchangeably.

In near-field scanning optical microscopy (NSOM), the diffraction limit is overcome by imaging directly in the near field [75, 76]. This is accomplished by effectively bringing the excitation source or the detector into the near field. This typically is an ultra-sharp tip or aperture. The near field does not extend very far (hence its name), in the visible this means that such an tip or aperture must be within tens of nm of the surface being imaged. Building off of techniques developed for AFM, NSOM scans a tip or aperture over a surface and excites and/or detects directly in the near field.

NSOM and related techniques are fairly distinct from single-molecule super-resolution microscopy. Like an AFM or an SEM, NSOMs are large, expensive, and highly specialized pieces of equipment, very different than the simpler, cheaper, and more broadly applicable optical microscope. One of the main advantages of an NSOM is how direct the measurement is, this simplifies a lot of the implementation and interpretation of some kinds of data. Additionally, because the tip can serve many different functions, NSOM can address questions that are difficult to address in an optical microscope. For instance, NSOM is an excellent technique for investigation localized excitations or fields on surfaces [77, 78]. On the other hand, because NSOM and related techniques are best at investigating surfaces, their utility is limited, and cannot be applied to some questions, like measuring dynamics inside a cell.

A number of correlative approaches to super-resolution imaging exist and are widely used. A popular technique is super-resolution optical fluctuation imaging (SOFI), which I use here as a general introduction to these methods. In SOFI, frames in a movie with blinking/bleaching fluorophores are correlated with each other to produce super-resolved images of the underlying structures [79]. Because noise won't correlate with itself, and the correlation of emitters at the same location will be stronger than the correlation of emitters at different locations, SOFI pulls out the locations of individual emitters with extremely high precision. A benefit of SOFI as compared to single-molecule imaging is the simplicity of the post-processing numerical analysis. However, due to its indirect nature, SOFI cannot as directly measure various properties of the fluorophores being imaged.

CHAPTER III

Plasmonic Optical Antennas

3.1 Introduction to Optical Antennas

Maxwell's equations, the governing laws of electromagnetism, are scaleless. Yet, the principles that underlay the design and function of much of radio technology are fundamentally different than the principles underlying optical technology. The reason for this is not that the underlying science is different, but rather because the length scales are different—with the wavelength of optical radiation[1] extending from $\sim$ 300 nm - 1.1 μm and the radio at $\sim$ 1 m - 100 km. Compared to humans, radio waves are approximately at our size or much larger, whereas optical radiation is many orders of magnitude smaller than human length scales.

Optical technology, for instance the lenses, mirrors, and filters described in Ch. II, functions by modifying optical wave fronts. For example, a mirror redirects (reflects) an incident optical wavefront, and a polarizer predominantly absorbs the incident wavefronts polarized perpendicular to its axis. Such optics are typically many orders of magnitude larger than the wavelength of the light being manipulated. For most of the history of the development of optics, there was not even a notion of trying to interact with optical radiation using technology comparable or smaller than the wavelength. Radio technology, on

---

[1] Here I am referring to optical radiation in the context of the atmospheric optical window, of which the visible spectrum is the main part. I am excluding microwaves from the radio, though most of this discussion applies there as well.

the other hand, operates almost entirely with wavelength-scale and subwavelength technology. The essential difference is that wavefront engineering in optics relies on the wave nature of light, whereas radio technology relies on directly manipulating the involved fields [16].

These two approaches to interacting with electromagnetic radiation—wavefront manipulation versus direct field manipulation—have their own strengths and weaknesses. Although there is no reason that all devices for a given frequency range should use one approach over the other, this was the situation.

It was only in the last few decades or so, with the rise of nanotechnology, that humans could reliably engineer structures at length scales comparable to optical wavelengths. These new nanofabrication techniques have opened the door for direct manipulation of optical fields, analogous to the approach in the radio frequency regime. Nanophotonics is the study and technological application of optics and photonics on the nanoscale, relying on the direct manipulation of optical fields. Nanophotonics has given us the optical antenna, the optical analog of the fundamental tool in radio technology—the radio antenna. A convenient definition of an optical antenna is given by Novotny and coworkers (emphasis mine):

> An **optical antenna** is a device designed to efficiently convert free-propagating optical radiation to localized energy, and *vice versa.* [16]

A general illustration of an antenna is shown in Fig. 3.1. An optical antenna converts optical radiation to localized energy, potentially to a receiver. In the opposite direction, a localized source of optical energy, for instance the light from a fluorescent molecule, is converted into free-propagating optical radiation.

The analogy between optical antennas and radio-frequency antennas is conceptually robust. However, our ability to engineer devices on the nanoscale is still far behind our ability to engineer macroscale devices, and therefore there are still practical differences in their implementation and use thus far. One of the biggest differences is that many radio-

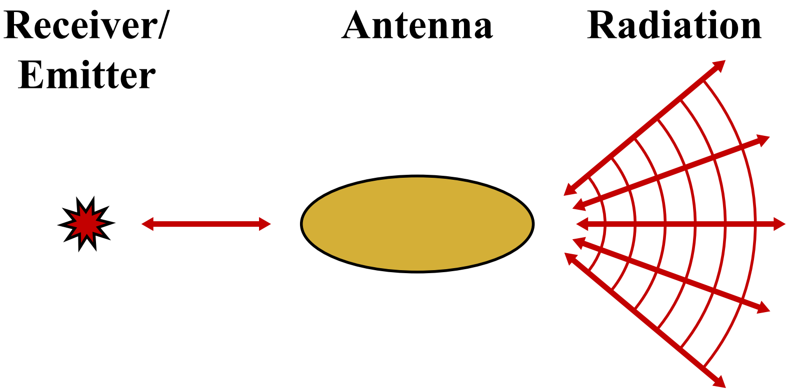

Figure 3.1: General illustration of the function of an antenna. An optical antenna converts free-propagating optical radiation to localized energy (to a receiver) and *vice versa* (from a emitter). Adapted from [16, 17].

frequency antennas are locally (and frequently electrically) driven, whereas most optical antennas are driven by incident optical radiation [17]. Another dissimilarity lies in the design of broadband antennas. Many radio-frequency broadband antennas rely on fractal designs, but such designs can be difficult to fabricate with sufficiently high quality for nanoscale optical antennas [17], though there has been significant progress on this front, see for example [80, 81]. In general, translating design principles from radio antennas to optical antennas has been a tremendously productive scientific endeavor producing many new technologies and scientific insights.

Many different kinds of optical antennas have thus far been developed. The two main classes of optical antennas are dielectric optical antennas and plasmonic optical antennas. Dielectric antennas rely on exclusively on Mie resonances (electric and magnetic dipole scattering resulting from particle polarization) to function as an optical antennas. Plasmonic optical antennas are made of conductors (usually metal) and their plasmon resonance is the key to their antenna function. In the next section I give a general introduction to plasmonics, ending with plasmonic optical antennas.

3.2 Introduction to Plasmonics

Plasmonics is the study and technological application of plasmons, the free-electron oscillations of conductors. Plasmonics is an essential part of the larger field of nanophotonics, which covers of research directions spanning the physical sciences, engineering, and biomedicine. The field of plasmonics has already produced myriad technological applications at all stages of development. In this section, I will briefly introduce some of the basic science behind plasmonics, serving as a foundation for the rest of this thesis. In this section, I will reproduce some of the derivations found in [40, 82, 83].

3.2.1 Metal Optics

We begin this discussion with Maxwell's equations for macroscopic media

$$\begin{aligned} \nabla \cdot \mathbf{D} &= \rho_e \qquad \nabla \times \mathbf{E} = -\frac{\partial \mathbf{B}}{\partial t} \\ \nabla \cdot \mathbf{B} &= 0 \qquad\;\; \nabla \times \mathbf{H} = \mathbf{J}_e + \frac{\partial \mathbf{D}}{\partial t} \end{aligned} \tag{3.1}$$

where **E** is the electric field, **B** and **H** are the magnetic fields, **D** is the displacement field, ρ_e is the external charge density, and $\mathbf{J}_e$ is the external current density. Together with the constitutive relations incorporating the material permittivity, ε, for linear and non-magnetic (material permeability $\mu = 1$) media

$$\mathbf{D} = \varepsilon_0 \varepsilon \mathbf{E} = \varepsilon_0 \mathbf{E} + \mathbf{P} \quad \& \quad \mathbf{B} = \mu_0 \mathbf{H} \tag{3.2}$$

where, ε_0 is the permittivity of free space, and μ_0 is the permeability of free space, are sufficient starting points for our electromagnetic derivations.

Metals are conductors, defined as materials with free-charge carriers. Here, "free" means that the carriers are free to move in the material. For our purposes here, it is accurate to treat the carriers in a metal, electrons, as a negatively charged gas—a plasma—confined by the material boundaries. To begin, we will consider the motion of an electron [40, 82, 83] of charge e and mass m, in the plasma being driven by an external light field at frequency ω, $\mathbf{E}_0 \mathrm{e}^{-i\omega t}$, whose oscillation is damped with a rate γ. This gives an equation of motion of for the electron position $\mathbf{r}$, of

$$m\ddot{\mathbf{r}} + m\gamma\dot{\mathbf{r}} = -e\mathbf{E}_0 \mathrm{e}^{-i\omega t} \tag{3.3}$$

solving by looking for oscillating solutions gives

$$\mathbf{r}(t) = \frac{e}{m(\omega^2 + i\gamma\omega)} \mathbf{E}_0 \mathrm{e}^{-i\omega t} \tag{3.4}$$

The polarization of a plasma with N electrons per unit volume is $\mathbf{P} = -Ne\mathbf{r}$. Substituting into Eq. 3.2 gives

$$\mathbf{D} = \left(\varepsilon_0 - \frac{Ne^2}{m(\omega^2 + i\gamma\omega)} \right) \mathbf{E}_0 \mathrm{e}^{-i\omega t} \tag{3.5}$$

rearranging Eq. 3.2 gives the dispersion of the dielectric function as

$$\varepsilon(\omega) = 1 - \frac{Ne^2}{\varepsilon_0 m(\omega^2 + i\gamma\omega)} \tag{3.6}$$

if we define the **plasma frequency**, ω_p, as

$$\omega_p = \sqrt{\frac{Ne^2}{\varepsilon_0 m}} \tag{3.7}$$

we arrive at the permittivity of a free-electron plasma

$$\varepsilon(\omega) = 1 - \frac{\omega_p^2}{\omega^2 + i\gamma\omega} \tag{3.8}$$

This expression for the permittivity is the central result of the Drude-Sommerfeld model [40, 82, 83]. Eq. 3.8 indicates that for a negligibly damped material, where $\gamma \ll \omega$, the

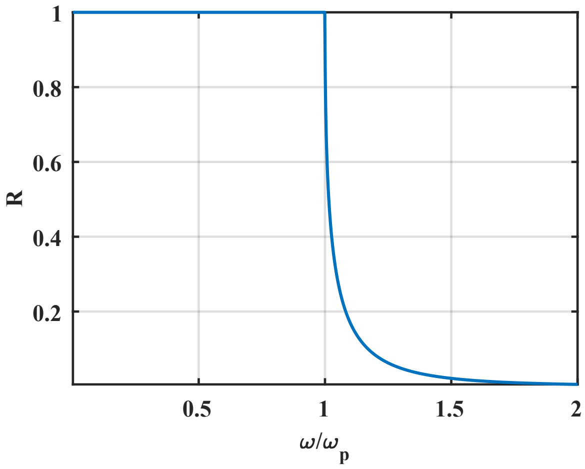

Figure 3.2: Reflectivity of a Drude plasma with negligible damping. Adapted from [83].

permittivity is entirely real (essentially no losses), and simplifies to

$$\varepsilon(\omega) = 1 - \frac{\omega_p^2}{\omega^2} \tag{3.9}$$

The refractive index, n, of a material is $n = \sqrt{\varepsilon\mu}$, and for non-magnetic media $n = \sqrt{\varepsilon}$. Since the reflection coefficient for an interface, R, is related to index of refraction as [44]

$$R = \left|\frac{n-1}{n+1}\right|^2 \tag{3.10}$$

we can see how R changes as the frequency changes relative to the plasma frequency. Fig. 3.2 shows that for $\omega < \omega_p$, a metal is highly reflective. This reflectivity dispersion is the result that we are accustomed to in everyday life, and why most mirrors are made of metal. For higher energy photons, $\omega > \omega_p$, $R \longrightarrow 0$, and thus the transmittance increases, showing the classic ultraviolet transparency of metals.

Inspecting the absorptive nature of the reflectivity regime, $\omega < \omega_p$, of this negligibly damped plasma is also instructive. For a light wave with wavenumber $k = n\omega/c$, propagating in a medium with complex refractive index $\tilde{n} = n + i\kappa$

$$\mathbf{E}_0 \mathrm{e}^{kz - i\omega t} = \mathbf{E}_0 \mathrm{e}^{-\kappa\omega z/c} \mathrm{e}^{i\omega(nz-t)} \tag{3.11}$$

we see that the intensity, $I = |\mathbf{E}|^2$, decays exponentially with absorption (decay) constant as $\alpha = 2\kappa\omega/c$. Separating Eq. 3.8 into real and imaginary parts, $\varepsilon = \varepsilon_1 + i\varepsilon_2$, gives

$$\varepsilon_1 = 1 - \frac{\omega_p^2}{\omega^2 + \gamma^2} \quad \& \quad \varepsilon_2 = \frac{\gamma\omega_p^2}{\omega(\omega^2 + \gamma^2)} \tag{3.12}$$

Solving $n + i\kappa = \sqrt{\varepsilon_1 + i\varepsilon_2}$ for κ gives the dispersion of the absorption coefficient as

$$\alpha(\omega) = \sqrt{\frac{2\omega_p^2\omega}{\gamma c^2}} \tag{3.13}$$

If instead of the absorption (decay) constant α of the intensity, we want to know the absorption length for the light electric field decay into the plasma, $\mathbf{E}_0\mathrm{e}^{-z/\delta}$, with $\delta = 2/\alpha$, substituting gives

$$\delta = \sqrt{\frac{2\gamma c^2}{\omega_p^2\omega}} \tag{3.14}$$

Where δ is the skin depth of the metal, the length over which an AC electric field decays by a factor of e as it enters into a metal. For most metals in the visible, the field decays extremely quickly with $\delta < 10\text{nm}$ [82, 83], showing the intense reflectivity of metals. An exponentially decaying field—a non-radiative field—is called an evanescent field.

The Drude-Sommerfeld model is actually quite accurate for most metals in the infrared region of the spectrum. However, for many metals, especially gold (on which much of this thesis is focused), there are significant inaccuracies in the visible. The main contribution to these inaccuracies comes neglecting interband transitions of electrons from low lying bands to the conduction band. These transitions are responsible for the recognizable colors of metals like copper and gold.

To account for interband transitions (bounded electrons), we follow the same procedure stemming from Eq. 3.3 and add a restoring force [40, 82] giving

$$m\ddot{\mathbf{r}} + m\Gamma\dot{\mathbf{r}} + m\omega_0^2\mathbf{r} = -e\mathbf{E}_0\mathrm{e}^{-i\omega t} \tag{3.15}$$

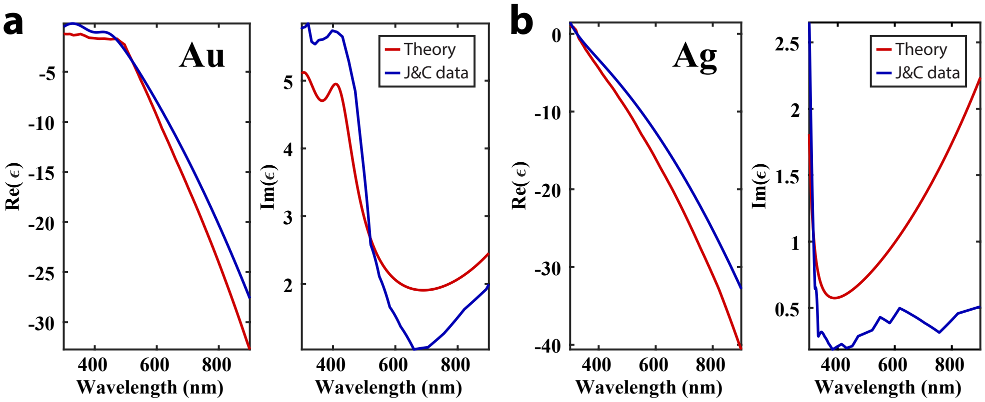

Figure 3.3: Permittivity dispersion of Au and Ag. Real and imaginary parts of the permittivity, ε, of (a) Au and (b) Ag. Data from Johnson and Christy [84]. Theoretical values calculated with Eq. 3.17, with parameters from [85, 86].

where Γ is the radiative damping from bound electrons, as opposed to the collisional damping γ. Solving gives

$$\varepsilon(\omega) = 1 + \frac{\tilde{\omega_p}^2}{\omega_0^2 - \omega^2 - i\Gamma\omega} \tag{3.16}$$

where $\tilde{\omega_p}$ is an analogous plasma frequency for the bound electrons. In reality, there may be more than one single resonance ω_0. For multiple resonances, additional Lorentz oscillator terms at those frequencies are simply added to the expression. Then typically, one adds the results for free electrons to the result for bound electrons giving the final permittivity

$$\varepsilon(\omega) = \varepsilon_\infty - \frac{\omega_p^2}{\omega^2 + i\gamma\omega} + \frac{\tilde{\omega_p}^2}{\omega_0^2 - \omega^2 - i\Gamma\omega} \tag{3.17}$$

where a constant offset ε_∞ is added to account for a constant background polarization in the $\omega > \omega_p$ region.

We can now compare these theoretical results to measured data. Fig. 3.3 shows measured data for the real and imaginary parts of the permittivity, ε, of (a) Au and (b) Ag, from a standard source, Johnson and Christy [84]. To calculate the theoretical values, Eq. 3.17 was used with five Lorentz oscillator terms with values for model parameters from [85,86]. Fig. 3.3 shows that both qualitatively and quantitatively, there is a good match between experiment and theory, and importantly most of the major features of the data are captured in the model. However, it is not a perfect reproduction of the data. The first conclusion I want to draw is that the theoretical results and derivations in this section appear to sufficiently capture much of the physics of metal optics and can therefore be used to help produce insights. On the other hand, because the match is not perfect, for carefully calculating optical phenomenon involving metals, as I will do repeatedly in this thesis, measured material data should be used when possible as opposed to a theoretical model.

3.2.2 Plasmons

Conductors can sustain collective oscillations of their free carriers, this phenomenon is called a plasma oscillation. Mark Fox has an excellent illustrative description of how such oscillations arise:

> [Consider a metal, a negatively charged free-electron plasma surrounding positively charged lattice ions. If there arises] a small region with with an excess charge, the charges in that volume would be repelled away by the surrounding charges. The velocity acquired in this process could cause the excess charges to overshoot their original position, in which case they would then be pushed back in the opposite direction. This process can lead to oscillatory motion called **plasma oscillations**. [83]

Though we will now derive the plasma oscillation frequency using only classical electromagnetism, oscillators are quantized. The quantum (quasiparticle) of a plasma oscillation is called a **plasmon**.

We begin our derivation of the plasmon frequency, closely following [83], with the charge continuity equation, where for a metal (free electrons and fixed positive lattice ions) the current is composed exclusively of electrons, giving

$$\nabla \cdot \mathbf{J}_e = \frac{\partial \rho_e}{\partial t} = -\varepsilon_0 \frac{\partial \mathbf{E}}{\partial t} \tag{3.18}$$

where ρ_e is the electron charge density, and the second equality came from substituting Gauss's Law (Maxwell's Equations are Eq. 3.1). We then substitute Ampere's Law, take a time derivative, and substitute Faraday's law, giving

$$\frac{\partial \mathbf{J}_e}{\partial t} + \varepsilon_0 \frac{\partial^2 \mathbf{E}}{\partial t^2} = -\frac{1}{\mu_0} \nabla \times (\nabla \times \mathbf{E}) \tag{3.19}$$

Newton's second law for electrons responding to local electric field gives $e\mathbf{E} = -m\mathbf{a}$. Thus, noting that the current density is $\mathbf{J}_e = -Ne\mathbf{v}$, and recalling our definition of the plasma frequency Eq. 3.7, we can rewrite Eq. 3.19 as

$$\omega_p^2 \mathbf{E} + \frac{\partial^2 \mathbf{E}}{\partial t^2} = -c^2 \nabla \times (\nabla \times \mathbf{E}) \tag{3.20}$$

where we substituted $c = 1/\sqrt{\varepsilon_0 \mu_0}$. It is now instructive to break $\mathbf{E}$ in Eq. 3.20 into transverse ($\nabla \cdot \mathbf{E}_T = 0$) and longitudinal ($\nabla \times \mathbf{E}_L = 0$) components [83], rearranging and separating gives

$$\omega_p^2 \mathbf{E}_T + \frac{\partial^2 \mathbf{E}_T}{\partial t^2} - c^2 \nabla^2 \mathbf{E}_T = 0 \tag{3.21}$$

$$\omega_p^2 \mathbf{E}_L + \frac{\partial^2 \mathbf{E}_L}{\partial t^2} = 0 \tag{3.22}$$

Solving by looking for wave solutions gives the dispersion relations for the two components [83]. For the transverse component, we get the normal dispersion for a transverse electromagnetic (TEM) wave in the plasma, $c^2 k^2 = \omega^2 - \omega_p^2$, showing that there are no radiative solutions for $\omega < \omega_p$, which is simply a reiteration of the reflectivity shown in Fig. 3.2.

For the longitudinal component, we get the surprising result that in the plasma, all longitudinal modes oscillate at the plasma frequency

$$\omega = \omega_p \tag{3.23}$$

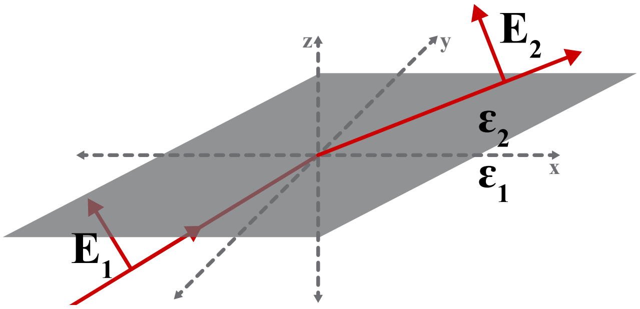

Figure 3.4: SPP interface geometry for p-polarization. Materials are ε_1 for $z < 0$ and ε_2 for $z > 0$ with p-polarized incident, $\mathbf{E}_1$, and transmitted, $\mathbf{E}_2$, light. Adapted from [40]

This result indicates that bulk (volume) plasmons have frequency ω_p, and thus energy $\hbar\omega_p$. Light is a TEM wave, and thus cannot directly couple to bulk plasmons (longitudinal excitations). Coupling plasmons to light occurs through secondary excitations [40,82,83].

3.2.3 Surface Plasmon Polaritons

For our purposes, far more important than the bulk plasmon, is the surface plasmon polariton (SPP). SPPs exists at the interface of two materials—on surfaces. A polariton is the quasiparticle of a photon coupled to a polarized excitation, thus SPPs are surface plasmons coupled with light. Closely following [40], we derive the dispersion for a SPP by considering the simple geometry of a light wave, with electric field $\mathbf{E}_1$, incident on a planar interface between two materials, with the geometry shown in Fig. 3.4. We start with the Helmholtz equation for a monocrhomatic wave at frequency ω with wavevector $\mathbf{k} = \frac{\omega}{c}\hat{\mathbf{k}}$

$$\nabla^2 \mathbf{E} + k^2 \varepsilon \mathbf{E} = 0 \tag{3.24}$$

We look for p-polarized (TM wave) solutions because s-polarized (TE wave) surface modes do not exist [82]. Such a wave on either side of the interface is

$$\mathbf{E} = \left(\hat{\mathbf{x}} E_{n,x} + \hat{\mathbf{z}} E_{n,z}\right) \mathrm{e}^{i\left(k_x x + k_{n,z} z\right)} \qquad n = 1, 2 \tag{3.25}$$

Enforcing that both sides of the interface be source-free implies that $\nabla \cdot \mathbf{D} = 0$, applying this to Eq. 3.25 gives the condition

$$k_x E_{n,x} + k_{n,z} E_{n,z} = 0 \qquad n = 1, 2 \tag{3.26}$$

which allows us to reduce Eq. 3.25 to

$$\mathbf{E} = E_{n,x} \left(\hat{\mathbf{x}} - \hat{\mathbf{z}} \frac{k_x}{k_{n,z}} \right) \mathrm{e}^{i k_{n,z} z} \qquad n = 1, 2 \tag{3.27}$$

We now match the fields across the interface using the boundary conditions from Maxwell's equations (Eq. 3.1). First, the parallel component of $\mathbf{E}$ must be continuous, giving

$$E_{1,x} = E_{2,x} \tag{3.28}$$

and the perpendicular component of $\mathbf{D}$ must be continuous, giving

$$\varepsilon_1 E_{1,z} = \varepsilon_2 E_{2,z} \tag{3.29}$$

Eqs. 3.26, 3.28, and 3.29 form a system of equations

$$\begin{pmatrix} 1 & -1 & 0 & 0 \\ 0 & 0 & \varepsilon_1 & -\varepsilon_2 \\ k_x & 0 & k_{1,z} & 0 \\ 0 & k_x & 0 & k_{2,z} \end{pmatrix} \begin{pmatrix} E_{1,x} \\ E_{2,x} \\ E_{1,z} \\ E_{2,z} \end{pmatrix} = 0 \tag{3.30}$$

which implies that the only non-trivial solution ($k_x = 0$, no wave, also solves the above system) is

$$\varepsilon_2 k_{1,z} = \varepsilon_1 k_{2,z} \tag{3.31}$$

We then apply the result of the boundary conditions on Maxwell's equations for a planewave across an interface: the wavevector parallel to the interface is conserved [40], giving

$$k_x^2 + k_{n,z}^2 = \varepsilon_n k^2 \qquad n = 1, 2 \tag{3.32}$$

where k is the vacuum wavevector magnitude, $k = 2\pi/\lambda = \omega/c$. Putting Eq. 3.31 and Eq. 3.32 together finally gives the dispersion relation (along the propagation direction) for an SPP [40, 82, 83]

$$k_x^2 = \frac{\varepsilon_1 \varepsilon_2}{\varepsilon_1 + \varepsilon_2} \left(\frac{\omega}{c}\right)^2 \tag{3.33}$$

and we also get the dispersion relation for the z (perpendicular) component of an SPP

$$k_{n,z}^2 = \frac{\varepsilon_n^2}{\varepsilon_1 + \varepsilon_2} \left(\frac{\omega}{c}\right)^2 \qquad n = 1, 2 \tag{3.34}$$

Before proceeding, it is important to inspect Eq. 3.33 and see the condition on the materials necessary for such SPP traveling solutions to exist—for $k_x \in \mathbb{R}$. To simplify this discussion, we assume that ε_1 & ε_2 have negligible imaginary components. An SPP is characterized by decay in z, meaning $k_{n,z} \in \mathbb{C}$. Eq. 3.34 implies that the only way to achieve this decay is by having $\varepsilon_1 + \varepsilon_2 < 0$. Eq. 3.33 indicates that the only way to ensure $k_x \in \mathbb{R}$ is if $\varepsilon_1 \varepsilon_2 < 0$: these two conditions together imply that one material must have a positive permittivity, and the other must have a negative permittivity with an absolute value exceeding that of the positive medium [40]. This situation is easily satisfied at the interface between many metal (large negative ε) and a insulator-like dielectric (small positive ε) materials.

If we replace ε_1 in Eq. 3.33 with the Drude model permittivity for a metal in the case

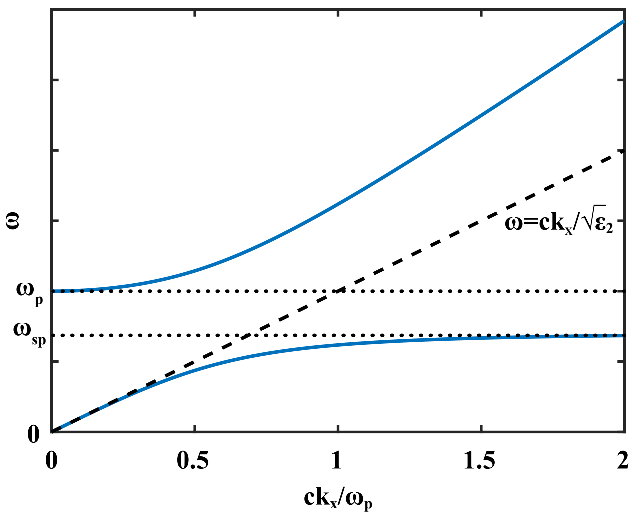

Figure 3.5: SPP dispersion. The dielectric is air (or vacuum), $\varepsilon_2 = 1$. The light line, $\omega = ck_x/\sqrt{\varepsilon_2}$ is indicated by the dashed line. Adapted from [83].

of negligible loss, Eq. 3.9, we can express the dispersion in terms of ω_p

$$k_x = \frac{\omega\sqrt{\varepsilon_2}}{c}\sqrt{\frac{1-\frac{\omega_p^2}{\omega^2}}{1-\frac{\omega_p^2}{\omega^2}+\varepsilon_2}} \tag{3.35}$$

Plotting the dispersion (for $\varepsilon_2 = 1$, air) in Fig. 3.5 shows two branches. The upper branch, $\omega = \omega_p$ for $k_x = 0$, is simply the regime of propagation inside the metal. The lower branch is the SPP branch. At high k_x, the SPP frequency asymptotes. To calculate its asymptotic value, we consider Eq. 3.35 in the limit that $k_x \to \infty$, which occurs when $\varepsilon_2 = \frac{\omega_p^2}{\omega^2} - 1$ Rearranging gives ω_{sp}, the surface plasmon frequency [40, 82, 83]

$$\omega_{sp} = \frac{\omega_p}{\sqrt{1+\varepsilon_2}} \tag{3.36}$$

The most important feature to takeaway from Fig. 3.5 is that the SPP branch approaches the light line (the dispersion of light in the medium) for small k_x, but never touches it. This lack of intersection implies that an external light field cannot directly excite a SPP. Instead, special phase-matching techniques to increase the wavevector are needed. These phase-matching techniques are typically accomplished by using a grating or a prism to create an evanescent field, which can directly couple to SPPs [40, 82].

Briefly, for a given material (ω_p is intrinsic), Eq. 3.36 shows that under the conditions of this derivation, the only extrinsic condition that ω_{sp} depends on is the the dielectric function of the surrounding medium. Thus, measuring ω_{sp} gives the medium dielectric constant, and if done precisely, can detect very small changes in the surrounding medium. This frequency shifting is the basic principle behind SPP refractive index sensors—for an introduction to the vast literature on this subject see [15, 26, 82, 87–90].

I end my discussion of SPPs by describing their ability to concentrate electromagnetic fields into nanoscale volumes. This field confinement is perhaps the most compelling reason that plasmonics has become such a large and dynamic field [23–25]. Eq. 3.34 gives the dispersion of the z (perpendicular) component of the wavevector of an SPP. For the evanescent field with this wavevector, the decay length, $\hat{z}$, is $1/k_z$. Using real material permittivity for Au [84] at $\lambda = 600$ nm, gives $\hat{z} = 29$ nm. SPPs can effectively confine their fields into nanoscale volumes far below the length scale dictated by the diffraction limit. [40, 82].

3.2.4 Localized Surface Plasmon Resonances

Though we derived the properties of SPPs for planar interfaces, SPPs can form for a variety of geometries. In particular, if confined (unable to propagate), a resonance develops called a localized surface plasmon resonance (LSPR). In this thesis, I will mainly focus on LSPRs sustained by metal nanoparticles. Interest in LSPRs has largely been driven by the many technologies and applications they promise to improve or enable, see the following reviews are references within for more details [15–22, 26].

LSPRs arise for metal nanoparticles smaller than the wavelength of light [26, 82]. By confining the SPP to such a small volume, the associated fields become even further confined than for the case of propagating SPPs[2]. This intense field localization requires the

---

[2] I will henceforth refer to propagating SPPs simply as SPPs. This is not to suggest that LSPRs aren't SPPs—which they certainly are—but to have a simple way to distinctly refer to the two phenomena.

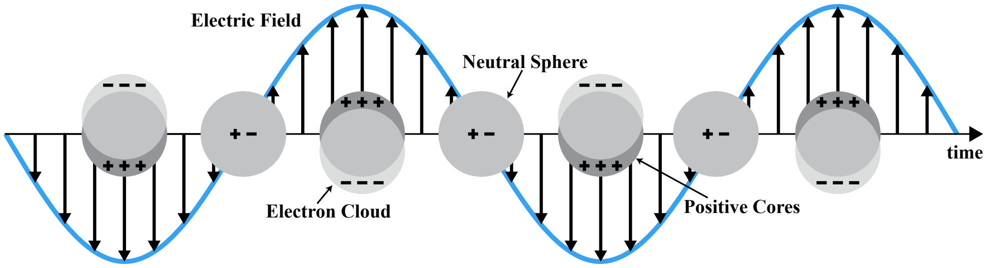

Figure 3.6: Light inducing a plasma oscillation of a metal sphere. As the electric field of the light wave oscillates, it causes the metal sphere's electron cloud to oscillate relative to the stationary positively charged ion cores. Adapted from [26].

field to bend at extreme angles and thus inherently relaxes the phase-matching problem of the SPP. Therefore, LSPRs can directly couple with freely propagating radiation. A light wave inducing a plasma oscillation (LSPR) in a metallic sphere is illustrated in Fig. 3.6.

A complete derivation of the fields assoicated with an LSPR is given in a number of textbooks [40, 82, 91], where I reccommend [92] for an especially thorough treatment, and the supplemental material of [26] for an especially clear and easy to follow derivation. Unfortunately, the standard analytical treatment is not especially generalizable, and though it can give us some useful insights into LSPRs, misses a lot of important features as well. With that caveat, here I will present a brief overview for the most straightforward analytically solvable case, a small sphere.

Consider a small spherical particle of radius a, with a dielectric constant ε in a non-absorbing medium with dielectric constant ε_m ($\varepsilon_m \in \mathbb{R}$) under monochromatic exciation $\mathbf{E} = \mathbf{E}_0 \mathrm{e}^{i(2\pi x/\lambda + \omega t)}$. If this sphere is sufficiently small relative to the wavelength of light ($a \ll \lambda$), then the field is essentially constant (static) over the volume of the particle—this condition is the quasistatic approximation. Solving for the electrostatic potential inside and outside of the sphere gives [82]

$$\begin{aligned} \Phi_{in} &= -\frac{3\varepsilon_m}{\varepsilon + 2\varepsilon_m} E_0 r \cos\theta \\ \Phi_{out} &= -E_0 r \cos\theta + \frac{\mathbf{p}\cdot\mathbf{r}}{4\pi\varepsilon_0\varepsilon_m r^3} \end{aligned} \tag{3.37}$$

where $\mathbf{p}$ is the particle dipole moment defined as

$$\mathbf{p} = 4\pi\varepsilon_0\varepsilon_m a^3 \frac{\varepsilon - \varepsilon_m}{\varepsilon + 2\varepsilon_m}\mathbf{E}_0 \tag{3.38}$$

indicating that the particle radiates as a dipole. Calculating the dipole moment now allows us to extract the polarizability using $\mathbf{p} = \varepsilon_o\varepsilon_m\alpha\mathbf{E}_0$ [82]

$$\alpha = 4\pi a^3 \frac{\varepsilon - \varepsilon_m}{\varepsilon + 2\varepsilon_m} \tag{3.39}$$

Thus we see that for a small sphere under the quasistatic approximation, the sphere's polarizability (and thus its dipole moment) has a resonance when the sphere dielectric constant is equal to the opposite of twice the medium dielectric constant, $\varepsilon = -2\varepsilon_m$. Because ε_m was specified to be non-absorbing, the resonance condition is more specifically

$$\mathrm{Re}(\varepsilon) = -2\varepsilon_m \tag{3.40}$$

This equation is known as the Fröhlich condition. Eq. 3.39 indicates that the strength of the resonance increases as $|\mathrm{Re}(\varepsilon)/\mathrm{Im}(\varepsilon)|$ increases—this condition on the materials is an essential point for plasmonics: lower losses means stronger resonances. Though this derivation is not restricted to metallic nanoparticles, for a metallic nanoparticle in an oscillating field, the mode associated with this resonance is the LSPR [26, 93].

We can connect the polarizability to the absorption and scattering efficiencies, Q_{abs} and Q_{sca}, respectively [21, 82, 92], giving

$$Q_{abs} = 4ka\mathrm{Im}\left(\frac{\varepsilon - \varepsilon_m}{\varepsilon + 2\varepsilon_m}\right) \quad \& \quad Q_{sca} = \frac{8}{3}(ka)^4\left|\frac{\varepsilon - \varepsilon_m}{\varepsilon + 2\varepsilon_m}\right|^2 \tag{3.41}$$

where the efficiency is simply the optical cross-section, C, normalized by the geometric area (e.g.$C_{abs} = \pi a^2 Q_{abs}$) and k is the wavevector. We thus see that the LSPR is a resonant

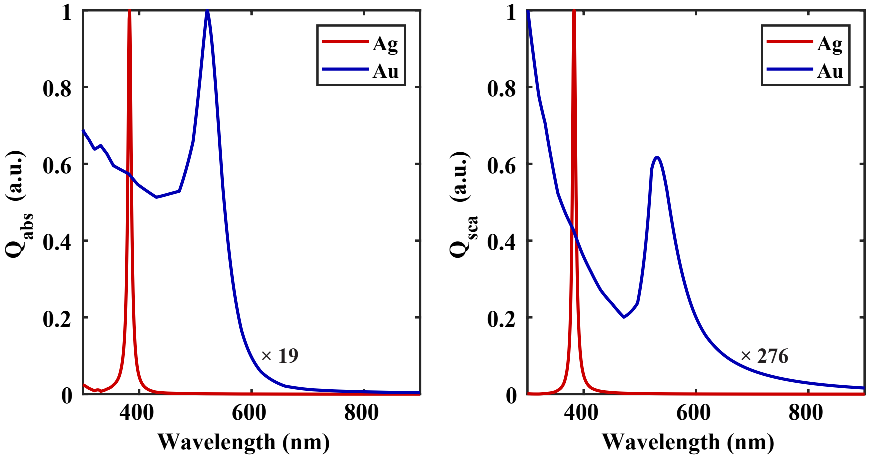

Figure 3.7: Theoretical scattering and absorption efficiencies of Au and Ag spheres. (Left) absorption efficiency. (Right) scattering efficiency. The surrounding medium is water ($\varepsilon_m = 1.77$). Spectra calculated with Eq. 3.41, using permittivity data from [84].

interaction with an external light field resulting in significant scattering and absorption. Fig. 3.7 shows Eq. 3.41 used to calculate the scattering and absorption efficiencies of Au and Ag spheres in water ($\varepsilon_m = 1.77$) using measured permittivity data from [84]. Fig. 3.7 shows that Au nanospheres have a LSPR in the visible frequency range, with $\lambda_{sca} = 531$ nm and $\lambda_{abs} = 521$ nm, and that the LSPR of Ag nanopsheres are nearly in the visible, with $\lambda_{sca} \approx \lambda_{abs} = 383$ nm. In this frequency range, Ag is a much better metal than Au ($|\mathrm{Re}(\varepsilon_{Ag})/\mathrm{Im}(\varepsilon_{Ag})| > |\mathrm{Re}(\varepsilon_{Au})/\mathrm{Im}(\varepsilon_{Au})|$), and Fig. 3.7 confirms our insight from Eq. 3.39: that Ag will have a stronger and higher quality (narrower linewidth) resonance than Au.

As was discussed for SPPs, LSPRs are excellent refractive index sensors. The Fröhlich condition (Eq. 3.40) shows that, as was the case for the resonance frequency of SPPs, for a given nanoparticle, the only extrinsic factor that shifts the resonance is the dielectric constant of the surrounding medium. LSPRs can be very precisely measured [94–96], and refractive index sensitivity down to the single-molecule level is regularly achieved [15,26, 82,87–90]. This sensing function is one the most important technological applications of plasmonics.

On resonance, LSPRs concentrate the incident field into nanoscale volumes near their surface. To see this concentration effect, we take the gradient of Eq. 3.37 ($\mathbf{E} = -\nabla\Phi$) giving [82]

$$\mathbf{E}_{in} = \frac{3\varepsilon_m}{\varepsilon + 2\varepsilon_m}\mathbf{E}_0 \quad \& \quad \mathbf{E}_{out} = \mathbf{E}_0 + \frac{3\mathbf{n}(\mathbf{n}\cdot\mathbf{p}) - \mathbf{p}}{4\pi\varepsilon_0\varepsilon_m r^3} \tag{3.42}$$

and we see that on resonance (at the Fröhlich condition), both the internal and external fields are greatly enhanced[3]. Furthermore, the external field decays as r^3, resulting in the confinement of these enhanced fields to a nanoscale volume about the nanoparticle.

So far, we have only discussed the case of a small spherical particle. Vast categories of other objects (particles, voids, wires, etc.) can sustain LSPRs. Furthermore, a particle sustaining an LSPR is not conditional on meeting the quasistatic limit (on which I have relied here). This approximation is simply a convenient tool to make analytical treatments more tractable. For an introduction to how important parameters like material, shape, dielectric environment, and size affect the LSPR, I recommend starting with [26, 97–102]. In general, as shapes become less symmetric, degeneracy decreases and LSPR modes are separated. As particles get bigger, their LSPRs tend to redshift (move to lower energies) and higher order modes (quadrupole modes for instance) become more prominent. As is clear from Eq. 3.36, the LSPR wavelength moves in the same direction as the medium refractive index: a higher refractive index medium redshifts the resonance, whereas a lower medium refractive index blueshifts the resonance.

Field concentration into nanoscale volumes upon resonant excitation is exactly what was meant by “converting free-propagating optical radiation to localized energy” [16] in Novotny’s definition of an optical antenna. In the following section we will complete this discussion of how metal nanoparticles, enabled by their LSPR, function as optical antennas, by discussing the converse direction, in which optical antennas convert localized energy into free-propagating optical radiation.

---

[3] Formally, it is mostly electromechanical, not electro*magnetic* energy which is being confined about the nanoparticle [20].

3.3 Emission Modification

Basic quantum electrodynamics (QED) shows that the energy levels of an atom or molecule are stationary solutions to Schrödinger's equation and therefore in isolation, an excited state will never decay [18,40,103,104]. Coupling this excited state to the quantized radiation field enables the process of spontaneous emission. In his landmark work [105], Purcell extended this insight by considering the problem of a radio emitter coupled to a resonant circuit. The Purcell effect (as it has come to be known) showed that not only is coupling to an environment necessary for spontaneous emission, but in fact, under certain conditions, the environment can drastically modify the emission.

Most work on the Purcell effect prior to the rise of plasmonics, considered emitters coupled to resonant cavities. Though not a perfect analogy, many of the insights from resonant cavities can be mapped on to optical antennas. This analogy is easiest to understand by viewing cavities and optical antennas as both special cases of optical resonators. I particularly like the work of Mario Agio in making this point and fleshing out the comparison, and I recommend starting with [18, 106]; Matt Pelton also has a very clear and easy to follow explanation of this analogy [104]. For a history of the development of this work, see the introduction in [107].

To see how an LSPR modifies the spontaneous emission rate of a coupled emitter, I will reproduce here a brief derivation of the Purcell effect from [106]. At the outset, I note that this is not a perfect description of the system under investigation in this thesis: a plasmonic optical antenna interacting with a single fluorescent molecule. However, the following derivation does captures some of the general principles of this system and is useful for understanding the origins of emission modification. After the derivation, I will detail how the results deviate from a real system.

In free space, the quantized electromagnetic field at a position $\mathbf{r}$ for wavevector $\mathbf{k}$ can be written as [106, 108]

$$\mathbf{E}(\mathbf{r}) = i\sum_{\mu}\sqrt{\frac{\hbar\omega_{\mu}}{2\varepsilon_0 V}}\mathbf{e}_{\mu}\left(\hat{a}_{\mu}\mathrm{e}^{i\mathbf{k}\cdot\mathbf{r}} - \text{h.c.}\right) \tag{3.43}$$

which is a sum over modes μ, in the quantization volume V, with polarization vector $\mathbf{e}$. The annihilation operator is $\hat{a}$, and h.c. denotes the Hermitian conjugate. Fermi's golden rule allows us to calculate the decay rate, Γ_0, for an emitter coupled to this quantized field

$$\Gamma_0 = \frac{2\pi}{\hbar}\sum_{\mu}\frac{\hbar\omega_{\mu}}{2\varepsilon_0 V}|\mathbf{d}\cdot\mathbf{e}_{\mu}|^2\delta(\hbar\omega - \hbar\omega_{\mu}) = \frac{2\pi}{3\varepsilon_0}\omega d^2 g_0(\omega) \tag{3.44}$$

where we have introduced the emitter dipole moment $\mathbf{d} = \hat{\mathbf{d}}d$ and defined the density of photonic states (DOS) as $g_0(\omega) = \omega^2/(2\pi^2\hbar c^3)$. The Purcell effect describes how the decay rate changes when the emitter is coupled to a resonator, in which case the emitter does not necessarily couple to planewaves ($\mathrm{e}^{i\mathbf{k}\cdot\mathbf{r}}$ in Eq. 3.43), but rather couples to the modes of the resonator, $\alpha_{\mu}(\mathbf{r})$. The quantized field is then [106, 108]

$$\mathbf{E}(\mathbf{r}) = i\sum_{\mu}\sqrt{\frac{\hbar\omega_{\mu}}{2\varepsilon_0}}\left(\hat{a}_{\mu}\alpha_{\mu}(\mathbf{r}) - \text{h.c.}\right) \tag{3.45}$$

where the resonator modes are normalized by the volume, and thus $|\alpha_{\mu}(\mathbf{r})|^2$ corresponds to the probability of finding a photon at position $\mathbf{r}$. Applying Fermi's golden rule allows us to calculate the decay rate, Γ, for an emitter coupled to a resonator

$$\Gamma = \frac{2\pi}{\hbar}\sum_{\mu}\frac{\hbar\omega_{\mu}}{2\varepsilon_0}\left|\mathbf{d}\cdot\alpha_{\mu}(\mathbf{r})\right|^2\delta(\hbar\omega - \hbar\omega_{\mu}) \tag{3.46}$$

If we now assume that the emitter is has a Lorentzian line shape[4] much narrower than the cavity line width, γ, the emitter is resonant with only one mode $\alpha(\mathbf{r})$, and $|\mathbf{E}\cdot\mathbf{d}|^2$ is

---

[4] A Lorentzian line shape is $L(\omega) = \frac{1}{\pi}\frac{\gamma}{(\omega-\omega_0)^2+\gamma^2}$

maximal, then the DOS is [106]

$$g(\omega) = \frac{2}{\pi\hbar\gamma} = \frac{2Q}{\pi\hbar\omega} \tag{3.47}$$

where $Q = \omega/\gamma$ is the quality factor of the resonance. If we define the mode volume as $V_\mu = 1/|\alpha(\mathbf{r})|^2$, we can rewrite the decay rate as

$$\Gamma = \frac{2d^2Q}{\varepsilon_0\hbar V_\mu} = F\Gamma_0 \tag{3.48}$$

where F is the Purcell factor [106]

$$F = \frac{3}{4\pi^2}\lambda^3\frac{Q}{V_\mu} \tag{3.49}$$

This result is central to this derivation. To enhance the spontaneous emission decay rate of an emitter coupled to a resonator for a given wavelength, the figure of merit is the Purcell factor, which scales as the ratio of the resonator quality factor to the mode volume

$$\frac{\Gamma}{\Gamma_0} \propto F \propto \frac{Q}{V_\mu} \tag{3.50}$$

One can qualitatively understand the Purcell factor by viewing Q as a measure of the spectral energy density of the resonance and V_μ as a measure of the spatial energy density of the resonance [109].

Plasmonic optical antennas, characterized by their LSPR, tend not to have large Q (especially in comparison with dielectric microcavities). Typically $Q \lesssim 10^2$ [110]. Inspecting any LSPR spectra shown in this thesis, shows that most appear somewhat broadband, indicating a relatively low quality factor. Low Q, might lead one to conclude that plasmonic antennas are not a good choice for increasing spontaneous decay rates, but this faulty conclusion ignores the denominator in Eq. 3.50.

As discussed in Sec. 3.2, plasmonic antennas excel at confining external electromagnetic fields to nanoscale volumes. This field confinement occurs by transferring the electromagnetic energy into the plasmon mode, which itself has an extremely small physical mode volume. A lossy resonator like a plasmon mode is quite different from the resonator modes typically considered in Purcell effect discussions; taking such differences into consideration to calculate an effective mode volume requires a careful treatment. In [109], Stefan Maier showed that the small *physical* mode volume of a plasmon does indeed imply a small *effective* mode volume consistent with the Purcell effect. Therefore, although plasmonic optical antennas do not typically have large quality factors, their extremely small mode volumes can indeed produce significant increases in the spontaneous decay rate of a coupled emitter.

This discussion of the Purcell effect for LSPRs is useful to illustrate the basic mechanism of emission enhancement and to give general design principles for the effect. However, a rigorous analysis of an emitter coupled to a plasmonic optical antenna highlights some flaws in this discussion. Femius Koenderink showed [110] that several key assumptions that go into describing the Purcell effect are not valid for LSPRs. Importantly, he found that a Purcell effect description of emission modification tends to *under*estimate the increase in the decay rate [110]. That is, plasmonic optical antennas are *more* effective at increasing the decay rate of a coupled emitter, than an analysis entirely based on the Purcell effect would indicate.

Finally, I want to note that a useful picture for understanding emission modification is that the antenna (resonator) modifys the local density of (photonic) states (LDOS). Revisiting Eq. 3.48 and defining the LDOS as $\rho(\mathbf{r},\omega) = g(\omega)|\alpha(\mathbf{r})|^2$, gives [106]

$$\Gamma = \frac{\pi d^2 \omega}{\varepsilon_0}\rho(\mathbf{r},\omega) = \frac{\rho(\mathbf{r},\omega)}{\rho_0(\mathbf{r},\omega)}\Gamma_0 \tag{3.51}$$

where ρ_0 is the free-space LDOS. Therefore, an antenna needs only to modify the LDOS to modify the decay rate of a coupled emitter. The antenna can be entirely passive, and in the case of a plasmonic optical antenna, the plasmon occupation number can be zero (the antenna need not be externally excited).

We have now seen that an LSPR can lead to increasing the spontaneous decay rate of a coupled emitter. This is exactly what was meant by “vice versa” in Novotny’s definition of an optical antenna as “a device designed to efficiently convert free-propagating optical radiation to localized energy, and *vice versa*” [16]. Together with the field confinement described in Sec. 3.2, we have now completely described how a metallic nanoparticle, enabled by its LSPR, can be accurately described as an optical antenna.

3.4 Simulating Optical Antennas

Electromagnetic optical antenna phenomena can only be solved purely analytically for very simple problems and under many (often restrictive) approximations [40]. Thus, numerical approaches are required to predict the full electromagnetic effects associated with optical antennas. Understanding these effects is essential for engineering optical antennas, elucidating or complementing experimental results, and advancing the science and technology of optical antennas.

There are many different approaches to numerically simulating electromagnetic phenomena. Some of these approaches even naturally integrate other physics into the simulation, and many of them have easy to use commercial implementations. I will not review all of these approaches, just briefly mention a few popular techniques. For comprehensive reviews and references for each technique see [111–116]. The multiple multipole method (MMP) and the volume integral method are well-known semi-analytical approaches [40]. Popular entirely numerical approaches are the FDTD method, the finite element method (FEM), the discrete dipole approximation (DDA), and the boundary element method (BEM). In this thesis, I have exclusively used the FDTD method, and will go over it in detail in the next section, but here I will first make a quick comparison between

FDTD and FEM.

In FDTD, the simulated objects are spatially discretized and the fields are solved for at sequential time points after an pulse of electromagnetic energy is inputted. A benefit of the FDTD method is because it is a time domain method, a single simulation gives broadband spectral information (from a Fourier transform of the result). A drawback is that the spatial discretization requires a rectangular grid, which imposes a significant trade-off between high spatial discretization and simulation speed.

FEM approaches also spatially discretize simulation objects, but instead of solving for the fields in the time domain, most implementations solve for the fields in the frequency domain [117]. Therefore, a significant drawback is that calculating spectra requires running a series of simulations at different frequencies. A major benefit of FEMs is that, unlike the FDTD method which is unique to electromagnetism, FEM is a general approach to numerically solving PDEs, and thus multiphysics simulations based on the FEM are straightforward to implement[5]. Another major benefit of FEM compared with FDTD is that the grid need not be rectangular, and thus high spatial discretization can be locally implemented, reducing the trade-off between high spatial precision and simulation time.

3.4.1 The FDTD Method

The FDTD method, introduced by Yee in 1966 [118], has become one of the most popular methods for numerically calculating electromagnetic phenomena [111]. Its popularity is partly due to its ease of use and high stability and accuracy. Here, I briefly overview the method, and in particular, detail how I use FDTD to calculate optical antenna phenomena in this thesis. For more detailed descriptions of the method, I reccommend [119–121].

In FDTD, the simulation objects are spatially discretized giving a discrete three-dimensional map of the permittivity and permeability, $\varepsilon(x, y, z)$ and $\mu(x, y, z)$. As illustrated in Fig. 3.8, the electric and magnetic fields are solved for in a leapfrog fashion throughout the sim-

---

[5] COMSOL Multiphysics is a very popular implementation of FEM capable of simulating a wide variety of physical phenomena.

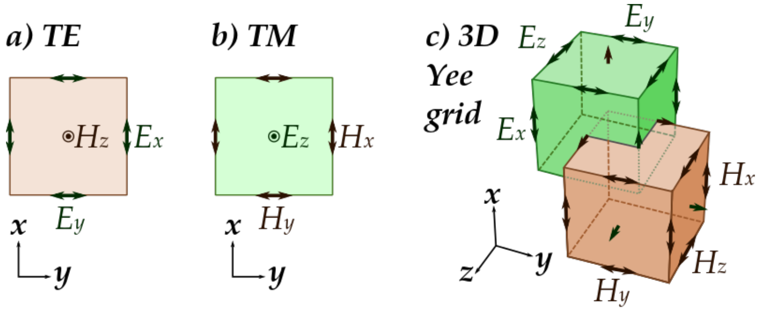

Figure 3.8: The FDTD Yee grid. The electric and magnetic fields are leapforgged to solve for each other throughout the discretized simulation space. Figure from FDominec under Creative Commons BY-SA 4.0 [122].

ulation space: one is solved for and used to update the other through Ampere's Law and Faraday's law (Eq. 3.1). Starting with the magnetic field at a given point, the electric field is solved for at the surrounding voxels, which then is used to solve for the new magnetic field values at the surrounding voxels, and so on. As a function of time, this process is repeated every half time-step so that the field values as a function of time are accounted for.

A source of electromagnetic energy must be input to the simulation. Typically, a short pulse of energy is input, giving a spectrally broadband response. The algorithm solves for the electric and magnetic fields at every voxel as a function of time until a stopping condition is met. The stopping condition can be something simple, like carrying out the simulation for a set amount of time (wall time *or* simulation time). Most typically though, the stopping condition is looking for an indication of convergence to the steady-state solution, for instance, the time derivative of the field components being very small. The somewhat surprising implication of this stopping condition, is that simulation times can depend strongly on the physical properties of the system being simulated, and in particular on how fast the pulse is dissipated.

The power of simulations is that you are free to precisely specify all of the parameters of the system under investigation, even if such arrangements are nearly impossible to create in a laboratory. This freedom though, does not extend to breaking relevant[6] laws of physics. An interesting example of this requirement is that in because FDTD is a time-domain method, material properties must obey the Kramers-Kronig relations, ensuring that causality is preserved [123].

In FDTD, like most other simulation techniques, the simulation volume is bounded. Therefore, simulation volumes must be truncated, and this truncation must be carefully implemented to ensure that it does not influence the simulation. An easy to way to see how this might happen is to consider the case of reflective boundary conditions. Such a situation is equivalent to placing the simulation objects inside of a cavity. So unless simulating a cavity is the goal, it is essential to ensure that boundaries have very little reflection. To approximate an open space in FDTD, typically absorbing boundaries are used, and the perfectly matched layer (PML) technique [124, 125] is the most popular choice. Periodic boundary conditions (in one or more dimension) can also be used to simulate periodic structures.

Finally, as I have already noted, in most FDTD implementations, the fields are solved for over a rectangular grid and this imposes a strict trade-off between accuracy, speed, and simulation size. A higher density of voxels (more grid points) gives a more accurate simulation. Due to the rectangular grid though, even if a local region is the only region in the simulation requiring high accuracy (for instance the confined fields about a plasmonic nanoparticle), the rectangular grid requires that the density of grid points along perpendicular dimensions is equal to the density in that region. The fields must be calculated at every grid point, so increasing the number of grid points means increasing the time required to run the simulation. Therefore, in order to keep simulation times reasonable, the simulation volume is kept as small as possible.

The implication of this trade-off between accuracy, speed, and simulation size is that

---

[6] By relevant, I mean relevant to the computational approach. For instance, in an electromagnetic simulation like FDTD, an object being at absolute zero temperature is inconsequential (for instance if temperature-dependent material properties are used), whereas trying to introduce a magnetic monopole would cause problems.

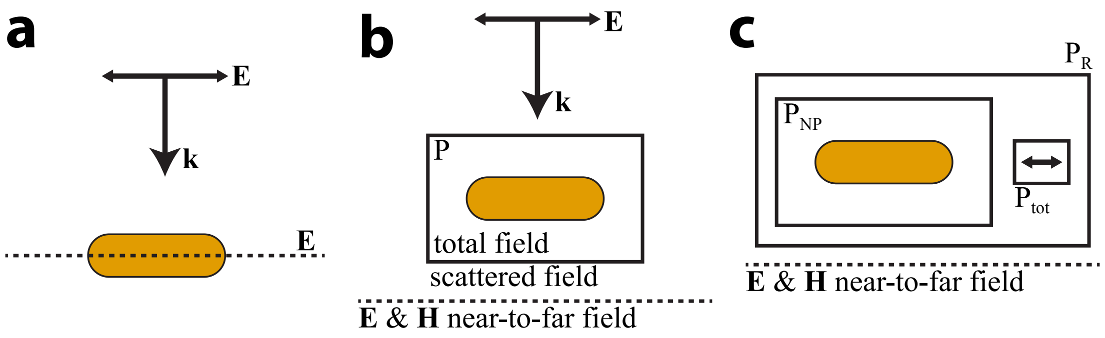

Figure 3.9: Optical antenna simulation geometries. (a) Simulating fields about a nanoparticle under planewave excitation. (b) Simulating nanoparticle scattering under planewave excitation. (c) Simulating emission modification from a dipole source. Dashed lines indicate field measurements and solid boxes indicate power flux, P, measurements.

the FDTD method is extremely well suited to studying localized phenomena—electromagnetic phenomena in the near field, the focus of nanophotonics[7]. However, if one wants to study far field effects of nanophotonics, there is a way around this problem. By solving for the fields in the near field and then employing near-to-far field transformations [126] based on the electromangetic equivalence principle [127], a compact FDTD simulation volume can accurately simulate far field effects.

In this thesis, I have exclusively used the commercial package *FDTD Solutions* by *Lumerical Inc.* [128].

3.4.2 Basic Simulation Geometries

The majority of simulation geometries I have used in this thesis can broadly be categorized into the three geometries shown in Fig. 3.9. These illustrations are simply meant to give a general sense of geometries, and are neither comprehensive nor detailed. Furthermore, FDTD solves **E** and **H** at all points in space and time, and the "measurements" I refer to are more like data analysis—pulling out specific pieces of information from the larger whole. That being acknowledged, *Lumerical FDTD Solutions* keeps simulation memory

---

[7] This specificity is one of the main reasons why I and many other researchers studying nanophotonics have chosen this technique over other choices.

down by not saving the fields at all space and time points. Rather, simulation “measurements” are instructions to the program about what data to save.

The first general geometry useful for simulating optical antennas is shown in Fig. 3.9a. This geometry is representative of how one might simulate the fields about an optical antenna under planewave excitation. This simulation represents the forward direction of Novotny’s definition of an optical antenna, a device which converts free-propagating optical radiation to localized energy. In the simulation, a planewave is used to mimic a far field excitation like a laser or a white light lamp. Then, the fields of interest are recorded. Fig. 3.9a indicates recording the electric field distribution through the center plane of a gold nanorod.

A second general category of simulation geometry is the scattering-type simulation shown in Fig. 3.9b. These simulations rely on the total-field/scattered-field formulation [126], which removes the incident field from outside of a given area leaving only the scattered fields. In this way, the scattered fields or power can be easily measured. This is extended to also give power absorbed by the antenna. Also, to more accurately simulate a real optical measurement [129], it is frequently more accurate to calculate the power scattered to the far field in a certain direction and for certain angles, using a near-to-far field transformation.

Scattering simulations provide a nice example of the importance of accurately representing the system being simulated. Measuring scattering from a single nanoparticle with a normally incident planewave, as shown in Fig. 3.9b, is not how single-nanoparticle scattering spectra are typically experimentally measured. In all of the papers that I have worked on for this thesis [35–37, 130], single-particle scattering spectra are measured in a dark-field configuration [131], as is typical for our field [95, 96]. Most dark-field configurations[8] use a highly-inclined annular excitation geometry. For particles whose scattering spectra is dominated by their dipole mode (i.e., for particle that meet the quasistatic

---

[8] Interestingly the dark-field configuration is not restricted to optical microscopy, electron microscopes for example can also be operated in such a dark-field configuration [132].

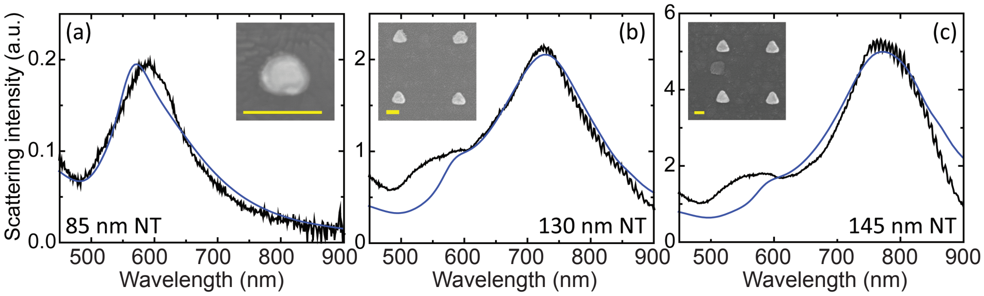

Figure 3.10: Gold nanotriangle scattering spectra. The black curves are measured dark-field scattering spectra and the blue curves are FDTD simulated scattering spectra. Nanotriangle side lengths are (a) 85 nm, (b) 130 nm, and (c) 145 nm. Insets are SEM images of the nanotriangles with 100 nm scale bars. From [36], ©American Chemical Society.

approximation), the difference in excitation geometry does not largely affect the result. However, in the case of larger particles, whose higher order modes are important, the difference is signifcant; this effect was first pointed out in [133] and is thoroughly detailed there.

Finally, Fig. 3.9c shows a typical geometry for simulating emission modification. An electric dipole source is used to simulate the light emitted from a point source. Keeping track of the power flux from the dipole source, the power absorbed by the nanoparticle, and the power radiated away, and comparing these values to a reference simulation of the dipole source alone, gives a full picture of the modified emission. I will present a thorough discussion of calculating emission modification in Chap. IV. Additionally, one may want to know the power radiated to the far field or the shape of the emission, in which case a near-to-far field transformation is imperative.

To end this section, I consider a specific example of simulating an optical antenna with FDTD. In [36], we studied gold nanotriangle (NT) optical antennas. Fig. 3.10 shows a comparison between the measured and simulated scattering scattering spectra. I simulated these triangles with a normal incidence source for simplicity. These triangles were fairly complex to simulate as their shape is not simple, they lay on top of a wetting layer made of Ti, and on a glass slide coated with indium tin oxide (ITO). Taking all of this complexity into account allowed for very accurate matches between the simulated and experimentally measured scattering spectra. In general the FDTD method allows for extremely accurate simulations of optical antennas, even for highly complex structures.

3.5 Gold Nanorods

In this section, I focus a specific plasmonic optical antenna, the gold nanorod (GNR). The first purpose of this section is to give an overview of GNRs, which are the predominant plasmonic optical antennas used in this thesis. Its second, and more general purpose, is to give an example of a specific plasmonic optical antenna, and show some of the complexity of its function as an optical antenna.

The GNR may be the most widely used, and scientifically and technologically important, plasmonic optical antenna. For an overview of the literature on GNRs see the following reviews [134–141], or any of the more general LSPR references I've cited in this thesis, for example [15–22, 26]. GNRs are are being used in applications ranging from computer memory [142, 143], to disease diagnosis and therapy [28, 29, 144], to fluoresence enhancement [145–147], to novel laser sources [148, 149]. Working on GNRs promises both a rich literature to build, on and broad impacts for new insights and developments. In my view, the main reasons that GNRs are so popular, are their facile synthesis (and thus inexpensive commercial availability), physical and chemical stability, tunable (relatively high Q) LSPR from the visible through the NIR, and broad chemical functionalizability.

A GNR is, as its name suggests, a rod-shaped nanoparticle made of gold. Fig. 3.11a and b show a reconstructed electron microscopy image of a single GNR, from [150]. As this figure shows, real GNRs have crystal faces, however GNRs are typically approximated as a cylinder with hemispherical caps. Fig. 3.11c shows a cartoon of a GNR illustrating the cetrimonium bromide (CTAB) bilayer that solubilizes most GNRs, including the ones used in this thesis.

An analytical solution for the polarizability of a small metal cylinder with hemispher-

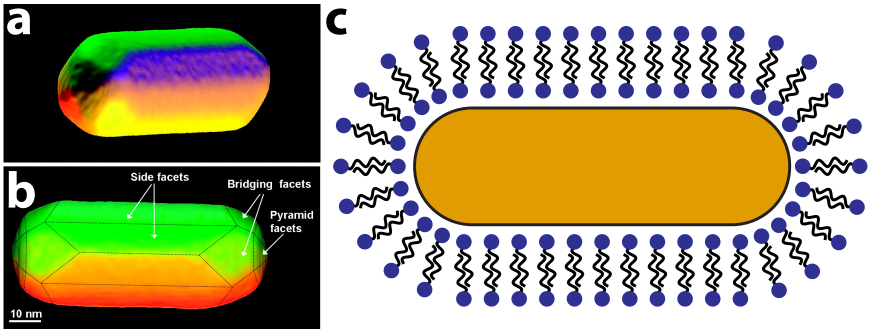

Figure 3.11: GNR morphology. (a) and (b) Scanning transmission electron microscope (STEM) images acquired with a high-angle annular dark field (HAADF) detector [132, 150]. From [150], ©American Chemical Society. (c) Cartoon showing CTAB bilayer around a GNR.

ical caps, similar to the derivation in Sec. 3.2.4 for a sphere, does not exist. However, if we approximate the shape as a ellipsoid, $\frac{x^2}{a_1^2} + \frac{y^2}{a_2^2} + \frac{z^2}{a_3^2} = 1$, with semiaxes a_1, a_2, a_3, we can derive the polarizability along each axis , α_i for $i = 1, 2, 3$, like Eq. 3.39 as [82, 92]

$$\alpha_i = 4\pi a_1 a_2 a_3 \frac{\varepsilon - \varepsilon_m}{3\varepsilon_m + 3L_i(\varepsilon - \varepsilon_m)} \tag{3.52}$$

where L_i is a geometrical factor given by [82, 92]

$$L_i = \frac{a_1 a_2 a_3}{2} \int_0^\infty dq \frac{1}{(a_i^2 + q)\sqrt{(q + a_1^2)(q + a_2^2)(q + a_3^2)}} \qquad i = 1, 2, 3 \tag{3.53}$$

where the three L_i aren't independent, since $\sum L_i = 1$. For a sphere, $a_1 = a_2 = a_3$ and $L_1 = L_2 = L_3 = 1/3$, and Eq. 3.52 reduces to Eq. 3.39. The resonance condition for Eq. 3.52 is

$$\mathrm{Re}(\varepsilon) = \varepsilon_m \left(1 - \frac{1}{L_i}\right) \qquad i = 1, 2, 3 \tag{3.54}$$

confirming the general principle for LSPRs mentioned earlier: that as shapes become less symmetric, degeneracy decreases, and LSPR modes are separated, resulting in the ellipsoid having three distinct LSPR modes.

A GNR has more symmetry than a general ellipsoid, with two equal semiaxes. Setting

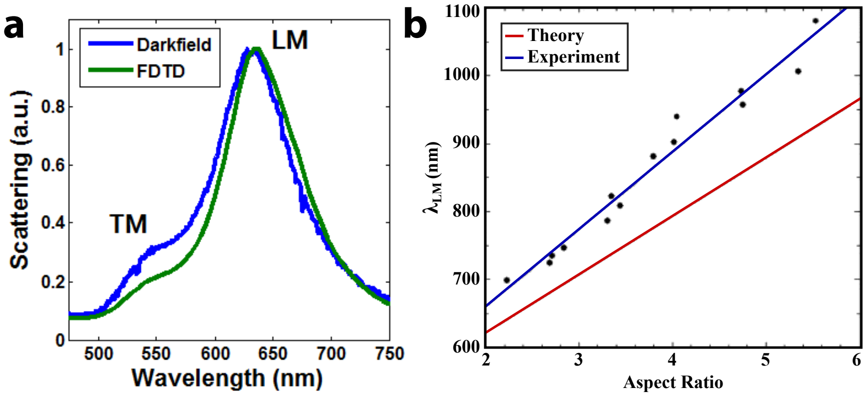

Figure 3.12: GNR scattering spectra and LM scaling. (a) Dark-field scattering spectra and FDTD simulated scattering spectra (b) Scaling relationship for the LM LSPR relative to GNR aspect ratio. b modified from [139] using data from [151], ©Elsevier B.V.

a_1 as the long axis and $a_2 = a_3 \Rightarrow L_1 > L_2 = L_3$, which in turn implies that the GNR has two LSPR modes. They correspond to plasma oscillations along the two symmetry axes. The mode corresponding to oscillations along L_1, the longitudinal (long) axis, is the longitudinal plasmon mode (LM), and the mode corresponding to oscillations along L_2, the transverse (short) axis is the transverse plasmon mode (TM). Fig. 3.12a shows a typical scattering spectra from a single GNR.

I mentioned that GNR LM is are easily tuned by synthesizing rods with varying aspect ratios, to see how this works, we evaluate Eq. 3.53 defining the ellipsoid eccentricity as $e = \sqrt{1 - a_2^2/a_1^2}$, giving [92]

$$L_1 = \frac{1 - e^2}{e^2}\left(\frac{1}{2e}\ln\frac{1 + e}{1 - e} - 1\right) \tag{3.55}$$

The takeaway is that L_1 depends on the eccentricity, e (or equivalently the aspect ratio a_1/a_2). Using Eq. 3.54 connects L_1 to the resonance, showing that for a GNR, the resonance depends only on the aspect ratio! If we substitute the metal permittivity with the Drude model Eq. 3.9 (which in wavelength is just $\varepsilon = 1 - \frac{\lambda_p^2}{\lambda^2}$) we can calculate how the LSPR shifts [139]

$$\lambda_{LM} = \lambda_p \sqrt{1 + \varepsilon_m \left(\frac{1}{L_1} - 1 \right)} \tag{3.56}$$

Fig. 3.12b (modified from [139]) shows a comparison between this theoretical analysis and experimentally measured LM resonances, using data from [151]. Though the theory consistently underestimates the LM wavelength, it does correctly predict the well known (approximately) linear relationship between the aspect ratio and LM wavelength. The TM does not move with aspect ratio, staying at the sphere LSPR frequency.

An essential fact about the GNR LSPR modes is they are polarized. Consider the LM, which corresponds to plasma oscillations along the long axis of the GNR. Such a plasma oscillation cannot be induced by a linearly polarized excitation polarized perpendicular to the longitudinal axis (parallel to the transverse axis) as no electric field oscillations occur in the direction of the such plasma oscillations! Similarly, to most efficiently excite the LM, a linearly polarized excitation should be polarized parallel to the longitudinal axis. The GNR polarization properties are easy to understand by recalling that the two GNR modes are dipole modes, meaning they absorb and radiate like electric dipoles. We can define an efficiency for exciting a LSPR, η_{ex}, which goes as

$$\eta_{ex} \propto |\mathbf{p} \cdot \mathbf{E}|^2 \tag{3.57}$$

where **p** is the LSPR dipole moment and **E** is the excitation electric field. The two modes also scatter and emit as an electric dipole, where a similar collection efficiency can be defined by replacing **E** with a vector along the collection angle(s). Fig. 3.13 shows the polarized nature of the GNR modes.

Fig. 3.13a shows the intense field confinement characteristic of plasmonic optical antennas. The field intensity decays away from the nanoparticle with a decay length of ~ 10 nm. Furthermore, the vector map in Fig. 3.13a shows the extreme field bending characteristic of the fields about a plasmonic nanoparticle. Recall that this extreme field bending

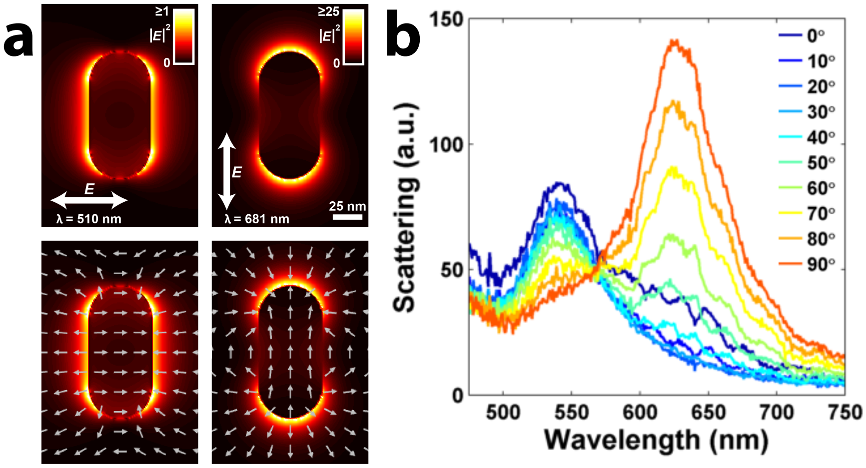

Figure 3.13: GNR field maps and polarized scattering. (a) Simulated field maps for a GNR under linearly polarized excitation and wavelength corresponding to each mode. (b) Measured dark-field scattering from a single GNR as a function of detection polarization (angle relative to the transverse mode).

inherently relaxes the phase-matching problem of the SPP, enabling LSPRs to couple directly to radiation.

In this section, we have seen that GNRs are an extremely popular and useful plasmonic optical antenna. They sustain two LSPRs, with the dominant mode, the LM, tunable from the visible through the NIR. Furthermore, like all plasmonic optical antennas, GNRs confine incident fields to extremely small volumes near their surface. The two GNR modes are high polarized (as dipoles) perpendicular to each other. In Chap. VII, I present a detailed investigation of how the excitation polarization affects the fluorescence of proximal (coupled) single molecules.

CHAPTER IV

Predicting Fluorescence Enhancement

The term fluorescence enhancement encapsulates many different modifications of fluorescence. Enhancement does not strictly mean an increase in the brightness of a fluorescent molecule, where brightness is the rate of photons emitted radiatively (photons emitted when an electron decays from $S_1 \rightarrow S_0$ in Fig. 2.5). Few optical antenna systems are successful in only *increasing* the brightness of coupled emitters, and never *decreasing* the brightness. Therefore fluorescence enhancement is usually understood to mean any change in brightness (increase or decrease), with enhancement > 1 meaning an increase in photons and enhancement < 1 meaning a decrease.

Fluorescence enhancement is a big field, with many researchers working on many different approaches to enhance fluorescence for many different applications and technologies. For an introduction to this literature, see the following reviews [8,107,152,153]. This chapter will focus specifically on predicting the enhancement of single-molecule fluorescence coupled to a plasmonic optical antenna.

This chapter will start with a discussion of how fluoresence enhancement is typically predicted. I will then point out the approximations that this approach relies on and then move onto detailing a complete theory. Next, I will cover my extensions and applications of this theory to accurately predict real experiments. Finally, the chapter will close with an example, applying this theoretical and computational framework to a real system, Cy5.5

coupled to a GNR in a PAINT experiment, which is the subject of the experiments presented in Chap. VII.

4.1 The Standard Approach to Predicting Fluorescence Enhancement

4.1.1 Fluorescence Near Metal Surfaces

Plasmonic fluorescence enhancement is an old field. Work going back to the 1960's has been investigating how fluorescence is modified by coupling to surface plasmons. As this work began far before the rise of nanotechnology, and even before microfabrication was very advanced, the early plasmonics literature was mostly concerned with how the fluorescence (or luminescence) of an emitter proximal to a metallic surface was modified. Interestingly, this work discovered that rough metal surfaces (which effectively produced LSPRs) had some different properties than smooth metal surfaces like a mirror.

The most well known example of this work is from Drexhage [154, 155] investigating the dependence of fluorescence brightness, lifetime, and angular emission, on distance to a metal surface. This kind of experimental work inspired Chance, Prock, and Silbey [156, 157] to develop a detailed theoretical model of the effect. Importantly, the model of Chance, Prock, and Silbey *did* explicitly include the emitted light coupling to SPPs. By using fit parameters in their model, they were able to accurately match experimental work. Fig. 4.1 shows Chance, Prock, and Silbey's theory fit to experimental data. Fig. 4.1 also shows a very important fact about fluorescence enhancement: the distance to the metal is essential. In this case, by simply varying the distance, the lifetime is either increased or decreased. For more information on understanding the fluorescence enhancement by a metallic surface see the following reviews [158,159], and in particular, I recommend [160].

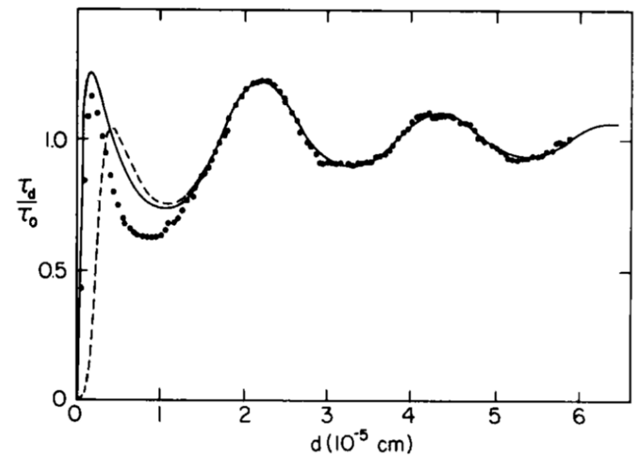

Figure 4.1: Fluorescence lifetime distance dependence near a mirror. Dots are experimental data, the dashed line is an approximate theory, and the solid line is the exact theory of Chance, Prock, and Silbey. From [156] ©John Wiley & Sons, Inc.

4.1.2 Plasmonic Optical Antennas

As nanotechnology matured, studies of fluorescence enhancement shifted from focusing on metal surfaces to plasmonic optical antennas. This section is focused on a general overview of how this coupling is typically calculated.

A typical expression for the measured fluorescence signal, S_0, from a fluorescent molecule with quantum yield, η_0, well below saturation, and excited monochromatically at ω_L is [152, 153, 161–163]

$$S_0 = \xi \eta_0 \left| \mathbf{p}(\omega) \cdot \mathbf{E}_0(\omega_L) \right|^2 \tag{4.1}$$

where ξ is the collection efficiency of the detection system. The molecule transition dipole moment is $\mathbf{p}(\omega) = |p(\omega)|\hat{\mathbf{p}}$, where $|p(\omega)|$ is the absorption (excitation) spectrum of the fluorescent molecule, and $\hat{\mathbf{p}}$ is its orientation. The excitation electric field is $\mathbf{E}_0(\omega_L)$. Because the excitation is monochromatic, the only value in the excitation spectrum that contributes is at $\omega_L \Rightarrow \mathbf{p}(\omega) \rightarrow \mathbf{p}(\omega_L)$.

We define the enhancement factor, g, as the ratio of this fluorescence signal in the presence of the plasmonic optical antenna, S, to the signal in its absence, S_0

$$g = \frac{S}{S_0} = \frac{\eta}{\eta_0} \frac{|\mathbf{p}(\omega_L) \cdot \mathbf{E}(\omega_L)|^2}{|\mathbf{p}(\omega_L) \cdot \mathbf{E}_0(\omega_L)|^2} \tag{4.2}$$

where ξ, from Eq. 4.1, has canceled out. We can break g into the product of the excitation and emission enhancement factors, g_{exc} and g_{em}, which highlights the utility of Novotny's definition of an optical antenna.

To calculate, g_{exc}, one compares the enhanced field about a plasmonic optical antenna to the original field. Because the field around an antenna changes very quickly over short distances, it is important to keep track of the location of the molecule. For a molecule at position $\mathbf{r}_0$, g_{exc} is [34, 40, 152, 161–167]

$$g_{exc}(\omega_L) = \frac{|\mathbf{p}(\omega_L) \cdot \mathbf{E}(\mathbf{r}_0, \omega_L)|^2}{|\mathbf{p}(\omega_L) \cdot \mathbf{E}_0(\mathbf{r}_0, \omega_L)|^2} \tag{4.3}$$

where $\mathbf{E}(\mathbf{r}_0, \omega_L)$ is the local electric field about the nanoparticle. The fields can be calculated any number of ways, with the simplest (and most complete) approach being to directly simulate them (for instance with an FDTD simulation as in Fig. 3.9a). This formulation is largely accurate, though its applicability to a wide range of experiments is limited. I will discuss this limitation in further detail in the next section.

Calculating the emission enhancement is less simple, and has been attempted with a variety of different approaches and approximations. The standard treatment is to determine a modified quantum yield η, often called the antenna efficiency, which is calculated similarly to the unmodified quantum yield η_0:

$$\eta_o = \frac{\gamma_{r0}}{\gamma_{r0} + \gamma_{nr0}} \tag{4.4}$$

where γ_{r0} and γ_{nr0} are the unmodified radiative and non-radiative decay rates respectively. It is well accepted that the intrinsic nonradiative decay rate of the molecule does not

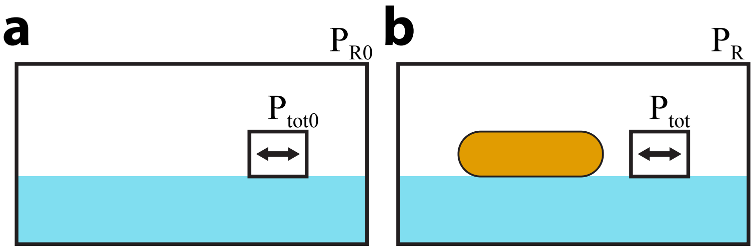

Figure 4.2: Classical dipole power flux calculation. Power radiated to the far field, P_R, is calculated as the flux through the outer box. The total power input into the simulation, P_{tot}, is calculated as the flux through a box around the dipole source. Appending 0 in the subscript indicates the reference calculation. (a) Reference simulation with no antenna (b) Actual simulation with the antenna. Adapted from [161] ©IOP Publishing

change upon coupling to a plasmonic optical antenna [34, 40, 152, 161–168]. However, the antenna has its own non-radiative decay pathways (for a metallic antenna, non-radiative pathways are dominated by Ohmic losses). To emphasize that this non-radiative pathway is radiative energy being transferred from the molecule to the antenna, which is then lost non-radiatively, we call this rate the energy transfer rate, γ_{ET}. Therefore, the modified quantum yield is

$$\eta = \frac{\gamma_r}{\gamma_r + \gamma_{ET} + \gamma_{nr0}} \tag{4.5}$$

Calculating fluorescence decay rates directly is a difficult quantum calculation. Instead, ratio equivalences with classical results are typically used. Calculating the power flux through the boxes drawn in Fig. 4.2 allows us to relate these classically defined quantities to the quantum decay rates as

$$\frac{P_R}{P_{R0}} = \frac{\gamma_r}{\gamma_{r0}} \quad \& \quad \frac{P_{ET}}{P_{R0}} = \frac{\gamma_{ET}}{\gamma_{r0}} \tag{4.6}$$

where the absorbed power is simply $P_{ET} = P_{tot} - P_R$. These equivalencies were rigorously derived in [169], and are the standard way to classically calculate the rates [34, 40, 152, 161–167]. The energy transfer rate is normalized relative to the radiative rate because the antenna does not modify the molecule non-radiative rate.

For simplicity, a single-frequency emission approximation is typically used—this is the main approximation we will correct in the following section. The frequency chosen is usually the emission maximum of the fluorophore, though, the LSPR of the antenna, or even the laser frequency, are also occasionally used. As the powers are evaluated at a single frequency, ω_{em}, under this approximation Eq. 4.6 is more precisely

$$\frac{P_R(\omega_{em})}{P_{R0}(\omega_{em})} = \frac{\gamma_r}{\gamma_{r0}} \quad \& \quad \frac{P_{ET}(\omega_{em})}{P_{R0}(\omega_{em})} = \frac{\gamma_{ET}}{\gamma_{r0}} \tag{4.7}$$

As we cannot classically directly calculate the rates, only the ratios as modified by the presence of the antenna, we have to rewrite Eq. 4.5. Dividing top and bottom by γ_{r0} and rearranging with Eq. 4.4 gives [164]

$$\eta = \frac{\frac{\gamma_r}{\gamma_{r0}}}{\frac{\gamma_r}{\gamma_{r0}} + \frac{\gamma_{ET}}{\gamma_{r0}} + \frac{1-\eta_0}{\eta_0}} = \frac{\frac{P_R(\omega_{em})}{P_{R0}(\omega_{em})}}{\frac{P_R(\omega_{em})}{P_{R0}(\omega_{em})} + \frac{P_{ET}(\omega_{em})}{P_{R0}(\omega_{em})} + \frac{1-\eta_0}{\eta_0}} \tag{4.8}$$

which is now cast in terms of the classically calculated power fluxes from Fig. 4.2 and the molecule's experimentally measured quantum yield η_0. Despite the single-frequency emission approximation, this model frequently does fairly well matching some experiments.

Fig. 4.3 shows two examples from the literature where this approximate theory predicts the experimentally measured fluoresence enhancement remarkably well. The first example, Fig. 4.3a - c from [167], shows an important feature of fluoresence enhancement, which is a strong dependence on the antenna resonance frequency. In the single-frequency approximation in Eq. 4.8, this spectral dependence is only dependent on how antennas with different resonances concentrate the laser ($\lambda_L = 633$ nm) and enhance the emission at the chosen emission frequency ($\lambda_{em} = 665$ nm, corresponding to the max of the dye Cy5). The second example, Fig. 4.3d from [165] shows the strong dependence on the separation between the fluorophore and the antenna, and importantly, the quenching (decrease in enhancement) at short separation distances.

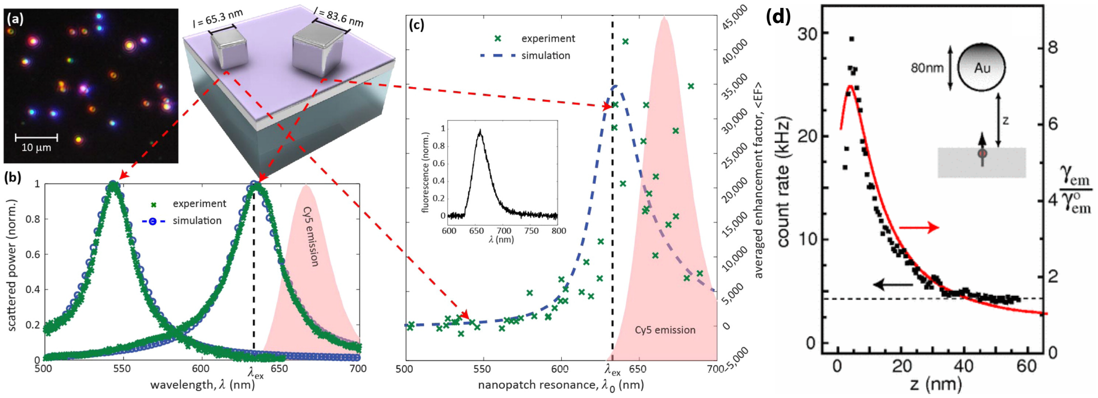

Figure 4.3: Comparing approximate theory with experiments. (a) Dark-field image and schematic of nanopatch antennas. (b) Simulated and experimental scattering spectra. (c) Comparison of theoretical and measured fluorescence enhancement as a function of nanopatch antenna resonance. (d) Comparison of theoretical and measured fluorescence enhancement as a function of separation, z, from a Au sphere. a - c from [167] ©American Chemical Society. d from [165] ©American Physical Society.

4.2 A Complete Theoretical Model

The single-frequency emission approximation is not well justified for most systems. Fluorescence emission spectra and LSPRs, are fairly broad. The broadness of these spectra, coupled with the fact that they have comparable bandwidths, indicate that it is not justified to approximate the emission enhancement as resulting from a single frequency of emission interacting with the antenna. The reason that the single-frequency emission approximation occasionally works, is that for some systems, the entire spectrum of fluorescence emission interacts with the antenna in the same manner, and thus the trend that a single frequency follows, predicts the trend for the rest of the emission spectrum. However, this condition is rarely mentioned, and *never* rigorously justified, before using the single-frequency approximation, and furthermore, it is generally not true for most antenna-fluorophore systems.

In addition to being poorly justified, as I will detail in this section, it is not particularly difficult to discard the single-frequency emission approximation and use a complete theory. The input required fields and power fluxes are calculated in exactly the same manner, the only difference being that now the power fluxes need to be calculated at many frequency points. The only new piece of information required is the intrinsic fluorescence spectrum of the emitter. Finally, using a complete theory provides the entire new fluorescence emission spectrum of the system, an interesting and useful quantity.

Though a complete theory of fluorescence enhancement has been detailed by a handful of research groups [34, 170–172], it is not in widespread use. In this section, I closely follow the formulation put forward in [34], and in the following section, I will detail my extensions to this framework to more accurately reproduce and predict experiments.

The fluorescence emission spectrum of the system is given by

$$F(\omega) = g(\omega)F_0(\omega) \tag{4.9}$$

where $F_0(\omega) = f(\omega)/f(\omega_{\max})$ is the amplitude normalized intrinsic fluorescence emission spectrum of the dye (in the absence of the antenna), and $f(\omega)$ is the intrinsic fluorescence emission spectrum of the dye in arbitrary units. We expand the total enhancement factor, $g(\omega)$, into the excitation and emission enhancement factors, respectively, as

$$g(\omega) = g_{exc}(\omega_L)g_{em}(\omega) \tag{4.10}$$

Note that the excitation and emission processes can be treated separately because there is no coherence between the two processes [34, 40]. A dye with excitation dipole moment $\mathbf{p}$ located at $\mathbf{r}_0$ will experience an excitation enhancement

$$g_{exc}(\omega_L) = \frac{\left|\mathbf{p} \cdot \mathbf{E}(\mathbf{r}_0, \omega_L)\right|^2}{\left|\mathbf{p} \cdot \mathbf{E}_0(\mathbf{r}_0, \omega_L)\right|^2} \tag{4.11}$$

where $\mathbf{E}$ & $\mathbf{E}_0$ are the local electric field in the presence and in the absence of the antenna respectively. The system is excited monochromatically at ω_L. Note that in this formulation, the absorption cross section of the dye and the excitation spectrum is encapsulated in $\mathbf{p}$.

By factoring into the magnitude and direction $\mathbf{p}(\omega) = |\mathbf{p}(\omega)|\hat{\mathbf{p}}$ we see that

$$g_{exc}(\omega_L) = \frac{|\mathbf{p}(\omega)|^2 \left|\hat{\mathbf{p}} \cdot \mathbf{E}(\mathbf{r}_0, \omega_L)\right|^2}{|\mathbf{p}(\omega)|^2 \left|\hat{\mathbf{p}} \cdot \mathbf{E}_0(\mathbf{r}_0, \omega_L)\right|^2} = \frac{\left|\hat{\mathbf{p}} \cdot \mathbf{E}(\mathbf{r}_0, \omega_L)\right|^2}{\left|\hat{\mathbf{p}} \cdot \mathbf{E}_0(\mathbf{r}_0, \omega_L)\right|^2} \tag{4.12}$$

and thus confirm that the excitation *enhancement* is only spectrally dependent on the laser frequency. The magnitude and spectral dependence of the dye excitation *does not* affect the enhancement.

The spectral probability density of the quantum efficiency (the probability density that an excited dye will emit a radiative photon at frequency ω) for a dye in the absence of the antenna is $\Pi_0(\omega) = \eta_0 f_0(\omega)$, where η_0 is the quantum yield in the absence of the antenna. The emission enhancement is then

$$g_{em}(\omega) = \frac{\Pi(\omega)}{\eta_0 f_0(\omega)} \tag{4.13}$$

where $f_0(\omega)$ is the integral normalized intrinsic fluorescence emission spectrum of the dye and we have defined $\Pi(\omega)$ as the spectral probability density of the coupled system. The quantum efficiency of radiative emission into a specific frequency is given by the rate of this specific transition, compared to all possible rates. *All possible rates* are not simply the radiative and the non-radiative rates at this specific frequency, but they also include the integral over all radiative transitions and all non-radiative transitions as well [34, 173].

To calculate the emission enhancement, we first define the decay pathways of the system. The radiated power enhancement factor is $g_r(\omega)$ and the energy transfered to the antenna (that does radiate into the far-field) factor is $g_{ET}(\omega)$. We can relate the classically calculated quantities to these rates through the ratios

$$g_r(\omega) = \frac{P_R}{P_{R0}} = \frac{\Gamma_R}{\Gamma_{R0}} \quad \& \quad g_{ET}(\omega) = \frac{P_{ET}}{P_{R0}} = \frac{\Gamma_{ET}}{\Gamma_{R0}} \tag{4.14}$$

Where, because “the electronic inhomogeneity in a liquid environment is randomized on a time scale smaller than the excited state lifetime" [34, 174], we integrate over all frequencies

$$\gamma_r = \gamma_{r0} \int_0^\infty f_0(\omega) g_r(\omega) d\omega \quad \& \quad \gamma_{ET} = \gamma_{r0} \int_0^\infty f_0(\omega) g_{ET}(\omega) d\omega \tag{4.15}$$

Bringing these quantities together we can calculate $\Pi(\omega)$

$$\Pi(\omega) = \frac{\gamma_{r0} f_0(\omega) g_r(\omega)}{\gamma_r + \gamma_{ET} + \gamma_{nr0}} \tag{4.16}$$

and now fully have the expressions for a complete theory of fluorescence enhancement, in the framework of [34], having discarded the single-frequency approximation.

It is straightforward to rewrite $g_{em}(\omega)$ with only the experimental inputs of η_0 and $f_0(\omega)$ and the computational outputs of $g_r(\omega)$ & $g_{ET}(\omega)$, by first looking at

$$g_{em}(\omega) = \frac{\Pi(\omega)}{\eta_0 f_0(\omega)} = \frac{1}{\eta_0} \frac{g_r(\omega)}{\gamma_r + \gamma_{ET} + \gamma_{nr0}} \tag{4.17}$$

and noting that can rewrite the quantum yield as

$$\frac{\gamma_{nr0}}{\gamma_r} = \frac{1}{\eta_0} - 1 \tag{4.18}$$

giving the implementable form

$$g_{em}(\omega) = \frac{1}{\eta_0} \frac{g_r(\omega)}{\frac{\gamma_r + \gamma_{ET}}{\gamma_{r0}} + \frac{1}{\eta_0} - 1} \tag{4.19}$$

4.3 Accurately Predicting Experiments

The complete theory of fluorescence enhancement laid out in the previous section accurately accounts for the modification of the light emitted from a fluorophore interacting with a plasmonic optical antenna. However, there are a number of extensions that need to be included to usefully and accurately match real experiments.

4.3.1 Dipole Orientation

Firstly, we can simplify Eq. 4.12 by simulating dipoles only oriented along our basis, *i.e.*, $\mathbf{p} = |\mathbf{p}|\hat{\mathbf{i}}$ and thus $\hat{\mathbf{p}} \cdot \mathbf{E} = E_i$ (e.g., in Cartesian coordinates $i = x, y, z$). Therefore in the simulations where the dipoles are only oriented along basis directions we need only the $\hat{\mathbf{i}}$ component of the magnitude of the field. Thus, Eq. 4.12 becomes

$$g_{exc,i}(\omega_L) = \frac{|E_i(\mathbf{r}_0, \omega_L)|^2}{|E_{i0}(\mathbf{r}_0, \omega_L)|^2} \tag{4.20}$$

An inspection of Eq. 4.20 or Eq. 4.12 shows that g_{exc} can diverge when the antenna reshapes the local field and $\hat{\mathbf{p}} \cdot \mathbf{E}_0(\mathbf{r}_0, \omega_L) = 0$ but $\hat{\mathbf{p}} \cdot \mathbf{E}(\mathbf{r}_0, \omega_L) \neq 0$. For a single dipole it is accurate, but not really useful, to say that such a dipole has an infinite enhancement. Furthermore, many experiments do not have such sufficiently controlled molecular dipole orientation that they can compare the enhancement for a single orientation. Here, I propose two different ways to calculate an excitation enhancement that is more realistic and useful.

The first option is to average the numerator and denominator independently,

$$g_{exc}(\omega_L) = \frac{\frac{1}{3} \sum\limits_{i=x,y,z} |E_i(\mathbf{r}_0, \omega_L)|^2}{\frac{1}{3} \sum\limits_{i=x,y,z} |E_{i0}(\mathbf{r}_0, \omega_L)|^2} \tag{4.21}$$

which is an easy to understand quantity that is useful as a metric for the average enhancement that a randomly oriented molecule would experience.

The other option, which preserves the granularity of a single dipole and thus is fully consistent with the emission side of this framework, is to compare the excitation of each dipole orientation to the average excitation of a dye in the absence of the antenna. We can thus define the excitation enhancement for each dipole orientation

$$g_{exc,i}(\omega_L) = \frac{|E_i(\mathbf{r}_0, \omega_L)|^2}{\frac{1}{3} \sum\limits_{i=x,y,z} |E_{i0}(\mathbf{r}_0, \omega_L)|^2} \tag{4.22}$$

which is now a non-divergent quantity that gives the excitation enhancement for a given dipole.

4.3.2 Detection Spectral Responsivity

The experimentally detected fluorescence spectrum is

$$F_{exp}(\omega) = \xi(\omega)F(\omega) \tag{4.23}$$

where $\xi(\omega)$ is the detection responsivity. We can calculate $\xi(\omega)$ by either accounting for all of the contributions individually or measuring it directly with a fluorescence standard. By using a standard which has an established published intrinsic spectrum $h_i(\omega)$, and measuring the fluorescence spectrum we get

$$h_{exp}(\omega) = \xi(\omega)h_i(\omega) \tag{4.24}$$

and can thus access $\xi(\omega)$ directly. Alternatively, we can account for the individual contributions to $\xi(\omega)$. The biggest contributions are likely the detector quantum efficiency $\eta_d(\omega)$, the filter(s) transmission $T_f(\omega)$, and the spectrometer grating efficiency $\eta_g(\omega)$, where

$$\xi(\omega) = T_f(\omega)\eta_g(\omega)\eta_d(\omega) \tag{4.25}$$

It is important to note that $\xi(\omega)$ depends on the particular experimental setup being used. Each filter combination will produce a different detection responsivity. Also $\xi(\omega)$ is different if we are imaging or measuring spectra, for the former, $\eta_g(\omega)$ would no longer be included.

4.3.3 Imaging Mode

In imaging mode, the measured intensity of a source with fluorescence spectrum $F(\omega)$ is given by

$$I = \int F(\omega)\xi(\omega)d\omega \tag{4.26}$$

and thus, the experimentally measured enhancement is given by

$$g_{exp} = \frac{I}{I_0} = \frac{\int F(\omega)\xi(\omega)d\omega}{\int F_0(\omega)\xi(\omega)d\omega} \tag{4.27}$$

4.3.4 Diverse Coupling Scenarios

Many of the theoretical investigations into optical antenna coupled fluorescence (including nearly all of the references in this chapter) study only a small number of emitter positions or orientations. Frequently, only one emitter position is studied and is meant to represent experiments. However, in reality, many experiments do not have such fine control over where the emitter is located relative to the antenna, and even fewer experiments control how the emitter dipole moment is oriented relative to the antenna and excitation polarization.

The PAINT experiments presented in this thesis emitters explore a wide range of positions and orientations. Therefore, to accurately predict experiments, it is important to simulate the diverse coupling scenarios. Instead of simulating every single possible coupling scenario, we take advantage of symmetry and knowledge of optical antennas to simulate a minimal number of emitters which can sufficiently capture the diversity of coupling scenarios.

To give an example, in [36] we studied dye molecules coupled to plasmonic nanotriangles in a PAINT experiment. I simulated the diverse coupling scenarios present in this experiment by placing a dipole source around the nano-triangle at each of the blue points

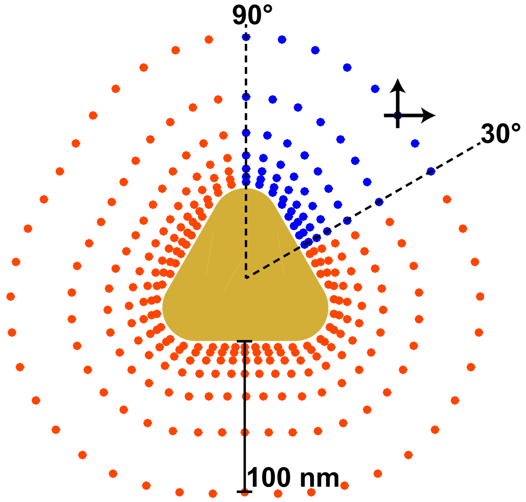

Figure 4.4: Simulation locations around a nano-triangle. Simulated dipole positions around a nano-triangle (blue dots), corresponding to the minimum symmetry unit of the triangle. At each position, two orthogonal dipole orientations were simulated, as indicated by the two arrows. The results for the blue dots were mapped to results for the red dots by symmetry. From [36] ©American Chemical Society.

shown in Fig. 4.4. By taking advantage of the symmetry of the triangle, it is sufficient to only simulate dipole positions from 30° to 90°. The results from this minimum symmetry unit can then be mapped to the rest of the area around the triangle indicated by the red dots in Fig. 4.4.

Both the excitation and emission enhancement change very quickly near the surface of the antenna and much more slowly further away (recall the discussions of field confinement in Chap. III). Therefore, we do not need to uniformly space the simulations in the area we are interested in; rather, by using a set of logarithmically spaced separation distances from the antenna, we can efficiently study the space. Logarithmic radial spacing ensures that we finely investigate the region near the surface of the antenna, and more coarsely investigate the region further away. Logarithmic spacing is justified by comparing with the exponential decay of the fields away from the antenna surface. Because the angular shape of the enhancement is more complicated in this case, equally spacing the points angularly is most appropriate. Finally, because the due molecules in the experiment could be oriented in any direction along the glass surface, at each one of those points, two orthogonal dipole orientations were simulated, as indicated by the two arrows. Using this approach, we ensured that we suitably mapped both the effect of emitter relative position and orientation.

Finally, in a PAINT experiment, we expect the dye molecules to stochastically and uniformly explore the entire surface. Therefore, to use these simulations to compare to statistical measurements of dyes in a PAINT experiment, some further data processing is required. The simplest approach is to interpolate the results from non-uniform simulated positions to a uniform map of positions or even a continuous function. To add some stochasticity to the results to better simulate an experiment, one can repeatedly randomly sample the results before or after interpolation (as long as spatial probability is considered) [35–37]. Using these approaches provides an accurate reproduction of experiments while using a minimal number of simulations.

Though one should try to use the smallest number of simulations possible by taking advantage of the considerations outlined in this section, the result is still a large number of simulations. For example, modelling the single antenna shown in Fig. 4.4, with seven radial separations, eight angular positions, and two dipole orientations, results in 112 separate simulations. If one included the z-oriented dipoles as well, it is 168. In [36] we studied five separate antennas, further increasing the number of simulations. Depending on the accuracy of the simulations, this collection of computations can take days or weeks to complete, highlighting the need for advanced computing approaches[1].

4.4 Simulating Gold Nanorod Fluorescence Enhancement

To end this chapter, I will walk through a specific example, showing some of the results that this theoretical and simulation framework can give. We consider a 50 × 85 nm GNR

---

[1] For example, I run most of my simulations on the University of Michigan's high-performance computing cluster, FLUX, which can greatly speed up calculations.

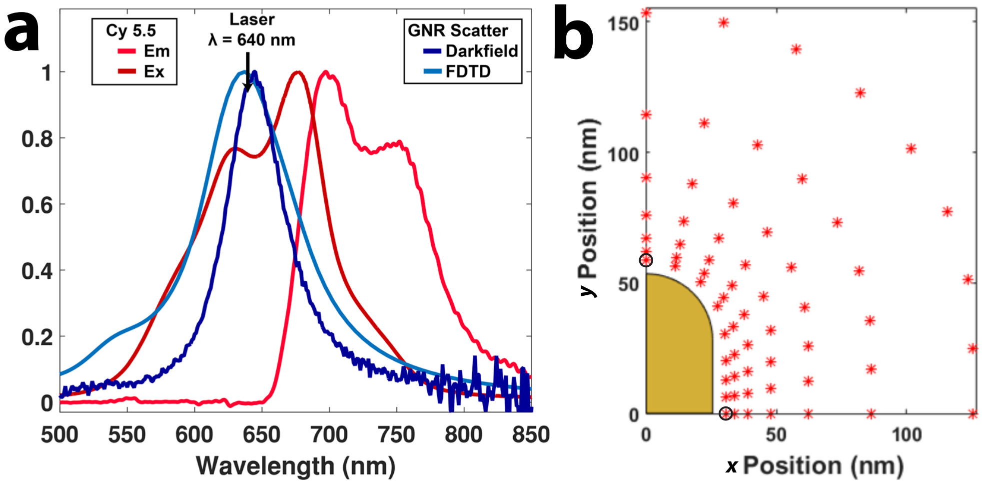

Figure 4.5: GNR simulation setup. (a) Cy5.5 excitation and emission spectra are shown in red. Measured dark-field and simulated scattering spectra for the GNR are shown in blue. (b) Simulation points around the GNR indicated by a red star. Spectra from the circled locations are shown in Fig. 4.6.

coupled to the dye Cy5.5 and excited with a 640 nm laser. Fig. 4.5a shows measured and simulated scattering for this GNR overlaid with the excitation and emission spectrum of Cy5.5. Based on the spectral relationship, we expect strong excitation enhancement and minimal emission enhancement. Dipoles were simulated at the positions around the GNR indicated by the red stars in Fig. 4.5b. At each position, three separate simulations were performed with the dipole source oriented along the three Cartesian axes, x, y, & z. The final experimental input into the simulation is the quantum yield (in Eq. 4.19) for Cy5.5, which is measured in the literature as $\eta = 20\%$ [175].

In this section, I will show results for the excitation laser polarized along both the longitudinal and the transverse axes. The fields look essentially the same as those previously shown in Fig. 3.13. For these simulations, a planewave (mimicking the laser excitation) excited the GNR from below and the electric field was recorded in the plane of the dipoles. Four simulations were run, corresponding to each polarization angle, with and without the GNR, giving $\mathbf{E}(\mathbf{r}_0, \omega_L)$ and $\mathbf{E}_0(\mathbf{r}_0, \omega_L)$ for Eq. 4.12.

Using the theory and computational framework described in Sec. 4.2, the complete fluorescence spectrum was calculated for each dipole position shown in Fig. 4.5b. Spectra

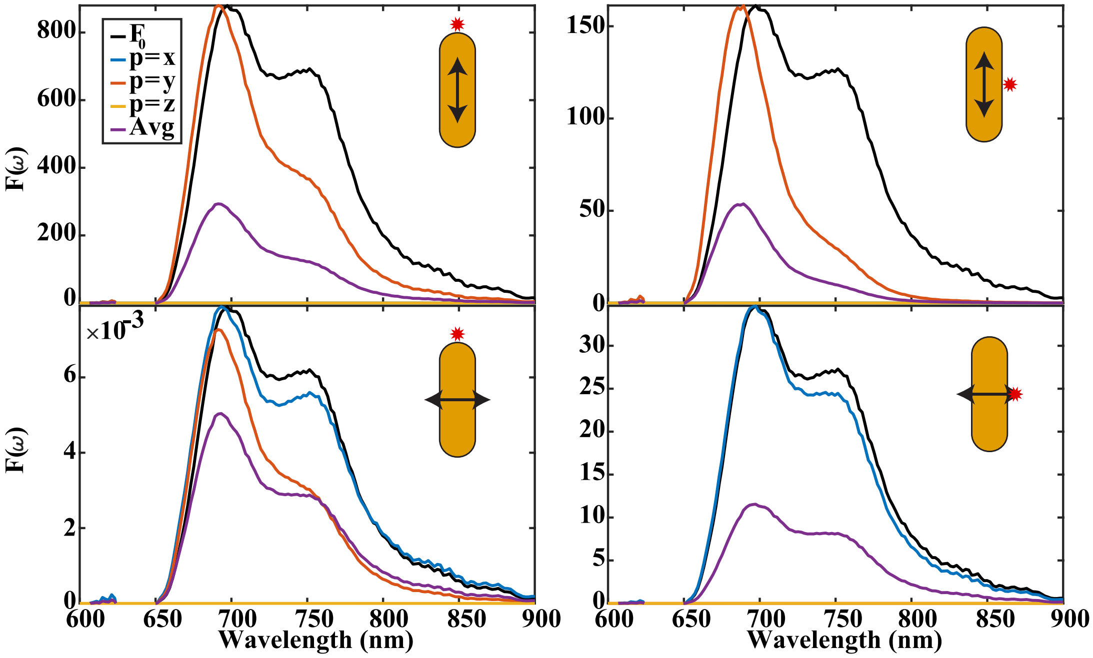

Figure 4.6: Example predicted fluorescence spectra. The dipole source is oriented in the x (blue), y (orange), and z (yellow) directions, along with the average of all three (purple). The intrinsic fluoresence spectrum (F_0) is shown in black, normalized to the plot maximum. The excitation is polarized along the longitudinal axis in a and b, and along the transverse axis in c and d. The dipole source is separated by 5 nm from the surface of the GNR, and located at the tip of the GNR in a and c, and along the side in b and d, corresponding to the circled locations in Fig. 4.5b.

from the circled locations in Fig. 4.5b are shown in Fig. 4.6

The spectra shown in Fig. 4.6 contain a lot of complexity, and highlight the diversity of results for different dipole orientations at different positions—all for just one antenna-dye-laser combination. Changing any one of those dimensions further multiplies the diversity of results, emphasizing the need for computations specifically matched to every unique system.

Fig. 4.6 contains several striking features. First and foremost, coupling a fluorescent emitter to an optical antenna reshapes the emitted fluorescence spectrum! The origin of this effect is that the light emitted at certain frequencies is enhanced or quenched differently. It is equivalent to describe this effect as resulting from modifying the probabilities of various radiative transitions differently. Secondly, Fig. 4.6 highlights the importance of

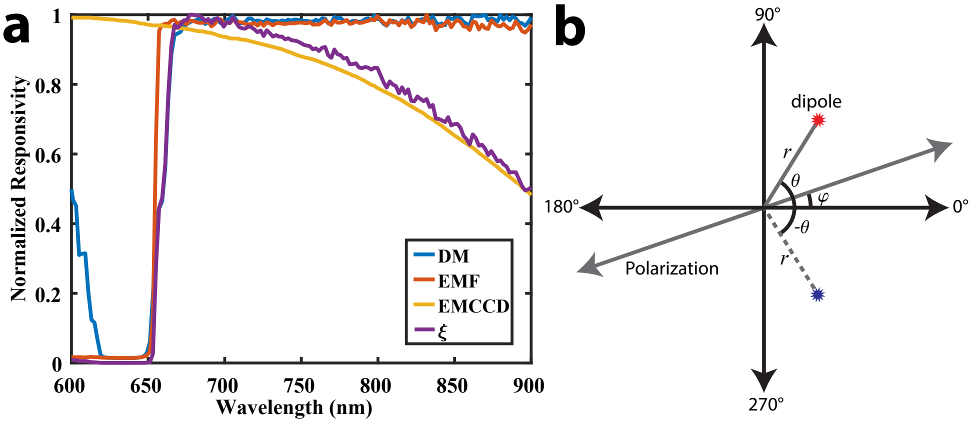

Figure 4.7: Spectral responsivity and simulation symmetry. (a) Transmission (responsivity) of the dichroic mirror (DM) in blue and emission filter (EMF) in orange. Spectral quantum efficiency of the EMCCD camera yellow. Overall system responsivity (ξ) in purple. (b) Schematic for mapping simulation points about a GNR by symmetry.

dipole orientation relative to the GNR field and relative to the excitation polarization. Finally, Fig. 4.6 shows that sometimes very large enhancements are possible, for example, in Fig. 4.6a the y-oriented dipole at the tip of the GNR excited with a longitudinal polarization gives a peak spectral enhancement of over 800×. Simultaneously, a lot of quenching occurs: for example, the same y dipole, with the transverse polarization is quenched by nearly a factor of 10^4 (the orange curve in Fig. 4.6a vs c).

Next, we need to incorporate the system detection spectral responsivity ξ (as in Eq. 4.23) to get the final predicted measurement enhancement (Eq. 4.27). For my experimental system (as described in Chapter VII), the main components that shape the spectral responsivity (combined as shown in Fig. 2.7) are the emission filter, the dichroic mirror, and the camera (EMCCD) spectral quantum efficiency. The transmission of the filters and the camera efficiency are multiplied to get ξ, shown in Fig. 4.7a.

Finally, to map out all possible coupling scenarios, we carefully consider the symmetry of emitters proximal to a GNR. The simulated points, in the region from 0° to 90°, as shown in Fig. 4.5b, are sufficient to capture all possibilities. However, we cannot simply map these points through reflections and rotations to 0° to 360°. To see why, consider that for a given

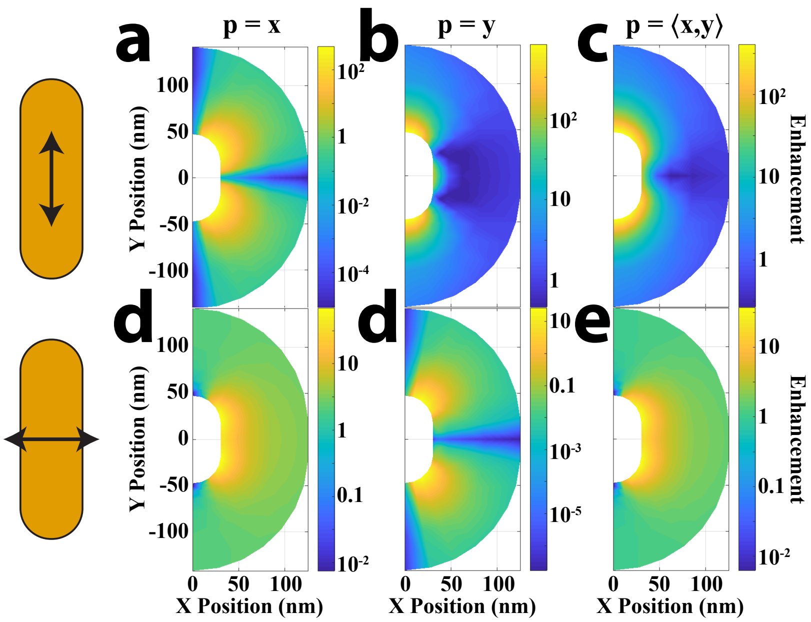

Figure 4.8: Enhancement maps around a GNR. The excitation is polarized along the longitudinal axis in a, b, and c, and along the transverse axis in d, e, and f. a and d are the results for $\mathbf{p} = \mathbf{x}$, b and e are the results for $\mathbf{p} = \mathbf{y}$, c and f are the average of the two dipole orientations.

polarization angle φ, a dipole located at (r, θ) (the red star in Fig. 4.7b) will experience a certain excitation enhancement, $g_{exc}(r, \theta, \varphi)$, and emission enhancement, $g_{em}(r, \theta)$. Its mirrored position across the x-axis (the blue star in Fig. 4.7b) will experience the same emission enhancement, $g_{em}(r, \theta) = g_{em}(r, -\theta)$, but because in general $\mathbf{E}(r, \theta) \neq \mathbf{E}(r, -\theta)$ $\Rightarrow g_{exc}(r, \theta, \varphi) \neq g_{exc}(r, -\theta, \varphi)$. The implication is that a unique set of enhancements need to be calculated for a region spanning 180°. To avoid running extra simulations, we can resolve this conundrum by calculating enhancements over the region from 90° to −90° using only the simulated points from 0° to 90°, shown in Fig. 4.5b. In the region from 0° to 90°, the enhancement is calculated as $g(r, \theta, \varphi) = g_{exc}(r, \theta, \varphi) g_{em}(r, \theta)$, and in the region from 0° to −90°, the enhancement is calculated as $g(r, \theta, \varphi) = g_{exc}(r, -\theta, \varphi) g_{em}(r, \theta)$.

Putting everything together allows us to calculate the full enhancement, g_{exp} (Eq. 4.27), for all points around the GNR. Interpolating gives a continuous map, as shown in Fig. 4.8 where again, we see a great diversity of enhancements for different coupling scenarios.

In an experiment, due to the mislocalization effect (briefly, the significant inaccura-

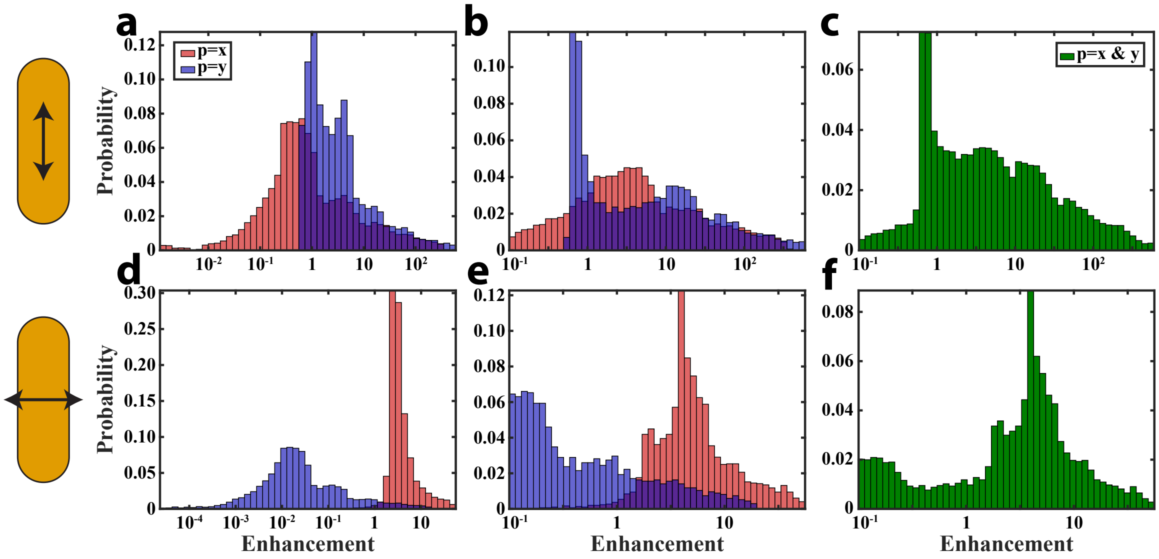

Figure 4.9: Predicted enhancement distributions. The excitation is polarized along the longitudinal axis in a, b, and c, and along the transverse axis in d, e, and f. a and b are all simulated points, d and e are realistically measured points, and c and f are combined distributions of $\mathbf{p} = \mathbf{x}$ and $\mathbf{p} = \mathbf{y}$, which in a, b, d, and e were labeled as red and blue respectively. Enhancement is g_{exp}.

cies in the super-resolved location of emitters coupled to an optical antenna, a detailed discussion of this effect is the subject of Chap. VI), it is not possible to actually make a map of the enhancement like in Fig. 4.8. Instead, it is more useful to look at the distribution of individual molecule enhancements (after interpolating to a uniformly spaced set of points). Fig. 4.9a and d show the enhancement distributions (g_{exp}, Eq. 4.27) for all simulated molecules. However, in a real experiment, it is unlikely that molecules with intensities well below the uncoupled intensity would still be detected. Thus to be consistent with experiments, all molecules with an enhancement less than 0.1 (10× dimmer than an uncoupled molecule) were removed from the distribution. Furthermore, for a PAINT experiment, mislocalization means that we cannot study just the molecules separated a certain distance from the GNR surface, which is the geometry simulated here. Instead, an experimentally feasible grouping of molecules is to consider all molecules which are separated from the GNR center within a given radius. Fig. 4.9b and e show the distributions of these more realistically measurable molecules. Finally, in a PAINT experiment, it is not possible to separate the $\mathbf{p} = \mathbf{x}$ and $\mathbf{p} = \mathbf{y}$ oriented dipoles from each other, and thus the actually measured distribution is the combined set, shown in Fig. 4.9c and f.

The physics of the polarization dependence of GNR coupled fluorescence is further explored in Chap. VII. Overall, this chapter has shown that it is essential to accurately model experiments, and not just test cases (as is typically done). By fully calculating the coupling of a fluorescent molecule to an optical antenna, and by accurately modeling experiments, one can gain deep insights into experiments and into the science being uncovered.

CHAPTER V

SMALL-LABS: An Algorithm for Localizing and Measuring Single Molecules in the Presence of Obscuring Backgrounds

This chapter presents a collaborative project, which is currently under review for publication as:

> B.P. Isaacoff, Y. Li, S.A. Lee, J.S. Biteen, "'SMALL-LABS: An algorithm for localizing and measuring single molecules in the presence of obscuring backgrounds," *submitted* (2018)

In this collaboration, I invented and originally developed the SMALL-LABS algorithm and the code implementing it, I created and analyzed the simulated data, and I wrote the first draft of the manuscript. Yilai Li performed the live-cell experiments and helped to analyze that data. Stephen Lee helped develop and refine the code to implement SMALL-LABS. Professor Julie Biteen advised and oversaw the entire project and especially helped to write the manuscript.

5.1 Abstract

Single-molecule and super-resolution imaging relies on successfully, sensitively, and accurately detecting the emission from fluorescent molecules. Yet, despite the widespread

adoption of super-resolution microscopies, most current single-molecule data processing algorithms fail to accurately localize and measure molecules in the presence of realistic backgrounds, which fluctuate significantly over time and space. Thus, samples or experiments that include obscuring backgrounds can severely—or even completely—hinder this process. To date, no general data analysis approach to this problem has been introduced that is capable of removing obscuring backgrounds for a wide variety of experimental modalities. To address this need, we present the SMALL-LABS (Single-Molecule Accurate LocaLization by LocAl Background Subtraction) algorithm, which accurately locates and measures the intensity of single molecules, regardless of the shape or brightness of the background. Accurate background subtraction is enabled by separating the foreground from the background based on differences in the temporal variations of the foreground and the background. We detail the function of SMALL-LABS here and validate this algorithm on simulated data as well as real data from single-molecule imaging in living cells.

5.2 Introduction

Single-molecule super-resolution imaging has revolutionized microscopy [1–3, 5, 6] through a variety of experimental modalities, such as stochastic optical reconstruction microscopy (STORM) [64], photoactivated localization microscopy (PALM) [62, 63], and points accumulation for imaging in nanoscale topography (PAINT) [61]. Yet, these imaging techniques all rely on accurately and precisely localizing single emitters with successful data processing algorithms [67–69, 176]. Realistic backgrounds vary in time and space and decrease the signal-to-noise ratio; these backgrounds can severely obscure super-resolution imaging by reducing the localization precision, introducing biases, and even preventing successful detection through both false-positive and false-negative errors.

Experimental measures can partially reduce backgrounds. Confined illumination via light sheets [177–179] and total internal reflection (TIRF) [180] reduce out-of-focus fluorescence, but ignore in-plane backgrounds. Longer wavelength probes decrease cellular autofluorescence [181], but sacrifice the resolution improvement of imaging at a shorter wavelength. Additional fluorescent objects incorporated into the sample for added functionality, such as plasmonic antennas for fluorescence enhancement or fiducial markers for drift compensation, improve imaging, but themselves produce a punctate spot in the background that can be misidentified as a fluorescent molecule (fluorophore) or that can obfuscate nearby fluorophores [26, 35, 182]. Moreover, these adaptations tend to complicate or restrict experiments. As a broadly applicable alternative to modifying experimental designs to reduce backgrounds, we report here a general data analysis solution: the SMALL-LABS (Single-Molecule Accurate LocaLization by LocAl Background Subtraction) algorithm, which accurately locates and measures the intensity of single molecules, regardless of the shape or brightness of the background. Accurate background subtraction is enabled by separating the foreground from the background based on differences in the temporal variations of the foreground and the background.

To our knowledge, no other background removal algorithm to date has enabled bias-free position determination (localization) and intensity measurements for a wide range of experimental systems (see Sec. 5.4 for more details). For instance, though several new approaches can accurately localize single molecules within a dense ensemble [67, 68] these algorithms all assume a background shaped like the image of an overlapping neighboring molecule and fail for arbitrary backgrounds. Additionally, such high-density approaches indiscriminately identify all signals that look like the system point spread function (PSF) as molecules regardless of their temporal dynamics. In general, approaches that attempt to subtract the background without first identifying the foreground [183] will inevitably introduce distortions by subtracting some of the image of a fluorophore from itself (discussed in detail in Sec. 5.6). SMALL-LABS provides the true background-subtracted image for single-molecule data by carefully distinguishing the foreground from the background; the only requirement is that the local background changes more slowly than the characteristic on/off timescale of the fluorophores. Here, we present SMALL-LABS and detail its function, we validate its performance on simulated single-molecule fluorescence data, and we demonstrate its capability on measured live-cell single-molecule data. Open-source Matlab code (GNU General Public License), is available at https://github.com/BiteenMatlab/-SMALL-LABS.

5.3 SMALL-LABS Operating Principles

The SMALL-LABS algorithm comprises a workflow described in detail below and summarized here. First, an *approximate background* calculated from the running average is subtracted from the raw movie, making single fluorescent molecules detectable with standard image analysis (Step *I*; Fig. 5.1a and b). This approximate background correction [183] removes the obscuring background, but will also subtract part of the true image from itself, reducing the apparent intensity and possibly introducing distortions (see Sec. 5.6). Therefore SMALL-LABS uses the approximate background subtraction only for this initial molecule detection step (Step *II*; Fig. 5.1b). Next, for each detection, SMALL-LABS identifies which frames contained detections at or near the position of the current detection. Fluorophores can turn on and off due to blinking, bleaching, or moving, so this check produces a list of "off" imaging frames in which no other molecule is detected in the local vicinity for each detected molecule (Step *III*). The *true local background* is defined in SMALL-LABS as the average of these "off" images at the molecule position. Finally, this true background is removed locally for each detected ("on" frame) molecule (Step *IV*; Fig. 5.1c). Importantly, this algorithm avoids subtracting the image of a molecule from itself, ensuring that further analysis of the background-subtracted image provides accurate super-resolution information and an unbiased measurement of each molecule's brightness (Step *V*).

The workflow for the SMALL-LABS algorithm is:

I Approximate background subtraction of the *raw_movie* to produce the *avgsub_movie*

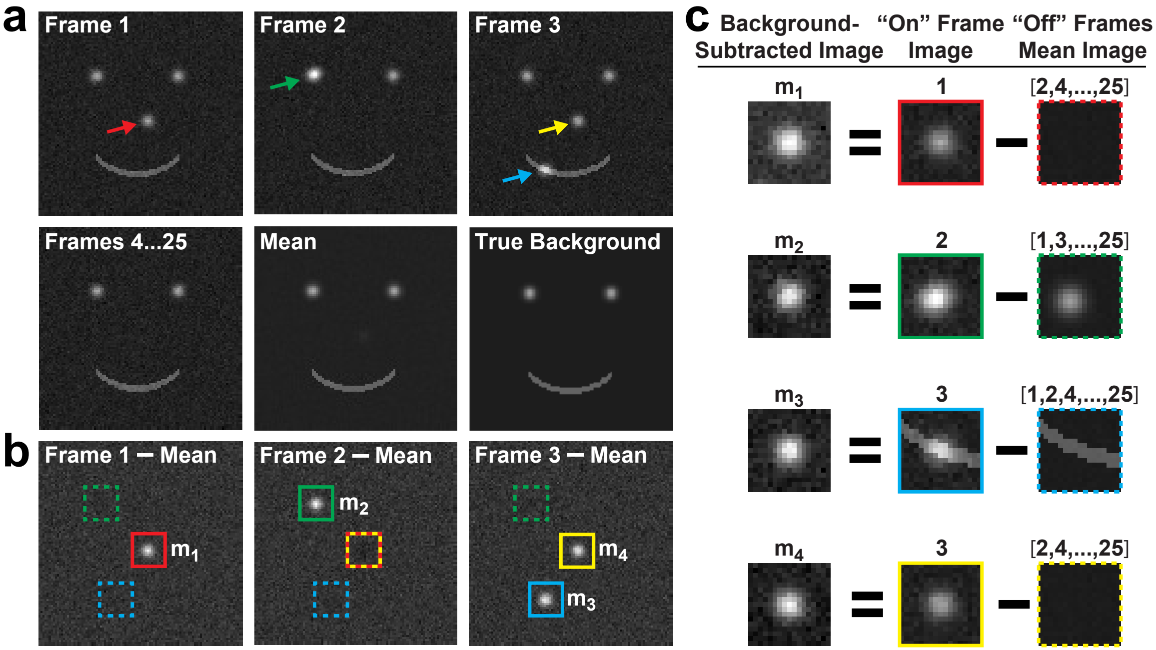

Figure 5.1: Schematic illustration of the SMALL-LABS algorithm. (a) Simulated raw data (imaging frames), the mean of the entire movie, and the true background (all on the same grayscale). Frames $1-3$ have fluorescent molecules, indicated with colored arrows; frames $4-25$ are identical except for detection noise, and only contain the background; the mean includes a faint image of the real molecules over the true background. (b) Molecule detection in the approximate background-subtracted movie. Solid colored boxes indicate a detected molecule, and dashed colored boxes indicate the local background for that molecule in "off" frames. Box colors correspond to the arrows in a. (c) The SMALL-LABS background subtraction process. The true image of each molecule is obtained by locally subtracting the mean of the "off" frames from the raw image.

II Molecule detection in the *avgsub_movie*

III "Off" frame identification for each detected molecule

IV Accurate background subtraction for each molecule

V Further analysis (position determination by peak fitting, motion characterization by tracking, etc.) of the true background-subtracted image of each molecule

I. Approximate background subtraction

A moving temporal mean (or median, or similar statistical measure) is calculated for the initial data (the *raw_movie*). This mean image is shown in Fig. 5.1a. For simplicity, the example shown in Fig. 5.1 uses the entire movie to calculate the average. In general, the characteristic on/off frequency of the molecules (from blinking, photobleaching, photoswitching, or motion) should be considered, and the choice of the window length over which to calculate an average (or median, or similar statistical measure) should be the longest window possible that doesn't include slow background changes at lower frequencies than this characteristic frequency. Having a long window time relative to the characteristic on/off time increases the accuracy of the approximate calculation of the background by minimizing contributions from molecules to the mean. The mean *raw_movie* image is then subtracted from each frame of the *raw_movie* to produce the approximate background-subtracted movie [35,145,183] called the *avgsub_movie*, as shown in Fig. 5.1b.

II. Molecule detection

An obscuring background in the *raw_movie* could produce a large number of false-positive or false-negative errors in single-molecule detection. The approximate background removal in Step *I* allows molecules to be identified in the *avgsub_movie* (Fig. 5.1b) with standard image analysis techniques. Though the accuracy and precision of these detections may be hindered by the approximate background (see Sec. 5.6), detecting molecules in the *avgsub_movie* rather than in the *raw_movie* greatly reduces the probability of false-positive and false-negative detection errors. In SMALL-LABS, as long as the false-negative rate is low and the false-positive rate is not excessive, the algorithm will be largely insensitive to any accuracy or precision loss in this detection step, as Step *IV* below repeats the characterization of each single molecule to provide high accuracy and precision measurements and allows for further false-positive screening. For example, molecular detection in the *raw_movie* would likely have missed molecule 3 in Fig. 5.1 to give a false-negative error. Similarly, single-molecule detection in the *raw_movie* would have incorrectly identified the eyes in the background smiley face in Fig. 5.1 as molecules, giving several false-positive errors. Doing molecule detection in the *avgsub_movie* avoids such errors.

III. "Off" frame identification

To accurately calculate the true background, it is essential to exclude the foreground (images of single molecules). For each molecule detected in Step *II*, a local "off" frame list is constructed; this list enumerates all frames in which no molecule was detected in the local region. Since we expect a diffraction-limited single molecule image with a shape given by the microscope point spread function (PSF), this local region is a box about the molecule position with side length approximately double the PSF width, though the local region can be changed for different imaging conditions like defocus. SMALL-LABS is agnostic to whether the same molecule is on in multiple frames. Rather, the "off" frames list depends only on if a molecule is detected in the same local region in other imaging frames, regardless of whether this molecule is the same molecule fluorescing for sequential frames, a molecule that blinks on and off, or distinct molecules that appear at the same location in different frames. The "off" frames list can be calculated over the entire movie, as in Fig. 5.1, or for a smaller number of frames, where the window length considerations discussed in Step *I* apply.

For example, in Fig. 5.1, molecule 2 (green arrow) appears in frame 2 and is the only molecule ever detected in that local region (green box); the "off" frames list for molecule 2 therefore consists of all the other frames in the movie, i.e., frames [1,3,. . . ,25]. Similarly, molecule 3 (blue arrow in Fig. 5.1) is only fluorescent in frame 3, and its “off” frame list is frames [1,2,4,…,25]. On the other hand, molecules 1 and 4 (Fig. 5.1) appear in the same local region (yellow and red boxes) in different frames, and thus the “off” frames list for each of those molecules excludes both the frame in which that molecule appears and the frame in which the other molecule appears (Fig. 5.1c).

IV. Accurate background subtraction

In this key step of SMALL-LABS, the true background is calculated by taking the temporal mean (or median or similar statistical measure) over only frames in the “off” frame list of the *raw_movie* in the local region around a molecule detection (dashed boxes in Fig. 5.1c). This accurate background does not contain partial images of the molecule itself or of any other molecule (the foreground). This accurate background is subtracted from the original *raw_movie* image of the molecule (solid boxes in Fig. 5.1c) to produce to a background-free image of the molecule (m_1, m_2, m_3, and m_4 in Fig. 5.1c). For example, for molecule 3 (Fig. 5.1c), the local region around the molecule in frames [1,2,4,…,25] is averaged to produce the true background, which is subtracted from the image of molecule 3 in the *raw_movie* frame 3, completely removing the background (part of the smiley face mouth).

V. Further single-molecule analysis

Once the background has been accurately removed, any further single molecule analysis can be performed. For instance, PSF-fitting the background-free single-molecule image provides super-resolution localization [1–3, 65] while avoiding any biases introduced by the background or an inaccurate background removal (see Sec. 5.6 for more details). In addition to enabling precise position determination, the emission intensity of each fluorescent molecule can be accurately measured based on PSF fitting or by summing pixel intensities after accurate background subtraction.

5.4 Background and Context

SMALL-LABS is, to my knowledge, the first general data analysis approach capable of accurately localizing single molecules and measuring their intensity, even in the presence of obscuring backgrounds. In this section, I'll review other background-removal techniques for single-molecule data to highlight their similarities and differences compared with SMALL-LABS.

5.4.1 SMALL-LABS Methodology and Advantages

SMALL-LABS localizes single molecules and measures their intensity regardless of the shape or extent of the background. This process is accomplished via three main operations. First, an approximate background removal allows molecules to be detected using standard image analysis techniques. Second, an "off" frame list is constructed; this list enumerates every other frame in which a molecule is not detected in the local vicinity of that detection. Third, the accurate background—an image that contains only "off" frame images and thus no molecules of interest—is specified and removed for each molecule.

The algorithm is very generalizable because it consists of several largely independent modular steps, which allow users to incorporate the most appropriate detection or post-subtraction analysis method (i.e., PALM/STORM, single-molecule tracking, single-molecule intensity measurements, etc.) for their specific application. Furthermore, SMALL-LABS is very flexible: users may specify all parameters. These two points ensure that this algorithm can handle a wide variety of backgrounds, imaging conditions, and experimental modalities. Finally, the only requirement for SMALL-LABS to successfully localize and measure single-molecules is that the local background must change more slowly than the characteristic on/off timescale of the emitting molecules being imaged. Overall, as discussed below, though some of the individual steps of SMALL-LABS are found in the literature, no one approach has put these features together into a cohesive and generalizable algorithm.

5.4.2 Literature Review and Comparisons

Approximate background removal

The first step of SMALL-LABS is to remove the approximate background to allow single-molecule detection. This initial subtraction is accomplished in SMALL-LABS by subtracting a running temporal mean or median. Though using a mean or a median can sometimes produce different results, they are conceptually very similar; therefore we do not distinguish between the two operations here. Previously, Hoogendoorn et al. subtracted a running temporal median (also referred to as median filtering) [183] and we subtracted a running mean (also referred to as mean filtering) [35, 145]. Chen et al. used box-car blurring to create a background image which was then subtracted from all frames [184]. These techniques provide a good statistical approximation under certain conditions (see Sec. 5.6 for more details). However, when the approximation breaks down due the stochastic nature of single-molecule data, the accuracy and precision of localization and brightness measurements will decrease. Furthermore, given the extreme precision achievable in single-molecule experiments and the deliberate circumvention of ensemble techniques to understand sample heterogeneities, it is essential to detect and accurately measure every single molecule. Importantly, SMALL-LABS uses the approximate background subtraction only for this initial molecule detection step.

"Off" frame subtraction only

SMALL-LABS is careful to locally subtract only background frames to leave behind the true foreground. Though this "off" frame subtraction is inspired by precedents in the literature, SMALL-LABS generalizes the concept to arbitrary backgrounds, which may have any shape or brightness and a wide variety of temporal dynamics. In 2014, faced with the challenge of subtracting a specific background—the photoluminescence of a plasmonic nanoparticle—Blythe et al. identified "on" frames based on an expected range of brightnesses for the nanoparticle and the molecules. Then, the specific features of this background were used: the authors fit the average of the “off” frames to a theoretical model of the nanoparticle, then subtracted the nanoparticle fit result from the rest of the frames [185]. In their subsequent 2015 work, Blythe et al. generalized this approach by subtracting the average image of the “off” frames immediately preceding and following each “on” frame instead of the fit [186]. Similarly, Zhou et al. addressed a related application—removing the image of a gold nanorod catalyst—by generating the background from a small number of “off” frames preceding each “on” frame [187].

SMALL-LABS increases the signal-to-noise ratio (SNR) of the selective background approach by subtracting *all* local “off” frames (within a user-specified window, to account for instance for a slowly changing background) rather than subtracting only a few frames. Moreover, by defining “on” and “off” in a local area instead of over the full image, SMALL-LABS provides more “off” frames and thus a better estimate of the background. Furthermore, because SMALL-LABS identifies “on” frames with flexible and modifiable molecule detection criteria, the algorithm can be very conservative to minimize the number of false-negative detections which would lead to faulty subtraction.

In an alternative approach, Zhou et al. identified “on” frames as well as the background intensity level from a 1D time trace [187]. Though this approach is perfect for single molecules confined to a specific region—for instance in single-particle catalysis—SMALL-LABS broadens the range of applications by avoiding two main limitations of this 1D signal analysis approach. Firstly, the 1D analysis requires the region of interest (ROI) to be identified *a priori*, whereas SMALL-LABS generalizes the approach to cases in which molecules are detected all over the field of view such that the tail of a given molecule’s image might obscure a certain ROI, complicating the statistical analysis. Secondly, SMALL-LABS uses the power of image analysis to identify molecules based on additional pieces of information (size, shape, sparsity, etc.) beyond merely intensity. Furthermore, modern image analysis takes advantage of new algorithms and GPUs to typically run much faster than serial 1D signal analysis of every pixel in the movie.

Combining an approximate background subtraction with "off" frame identification

In SMALL-LABS, we incorporate and further generalize background subtraction concepts introduced by generalized Single-Molecule High-Resolution Imaging with Photobleaching (gSHRImP) [188] and Bleaching/Blinking Assisted Localization Microscopy (BALM) [189]. The first step of gSHRImP and BALM removes an approximate background by sequential frame subtraction (frame $n' =$ frame $n -$ frame $(n + 1)$). This initial subtraction was also used by Blythe et al. to remove the obscuring background in their experiment before carefully identifying "on" frames [185]. The next step in gSHRImP and BALM identifies when a molecule turns off based on the resulting bright spot in the sequentially subtracted movie. Then these algorithms average groups of frames between sequential turn-off events; this background is subtracted from the detected "on" frames. However, these algorithms are specifically designed for localizing immobile but overlapping and blinking/bleaching fluorophores. If the molecule moves slightly (or changes PSF shape, for instance due to rotation or focus drift) between frames, this kind of subtraction and averaging will reduce the localization accuracy. Here, SMALL-LABS is designed for cases that are more general. SMALL-LABS can handle moving molecules, backgrounds not shaped like molecules, and especially highly obscuring backgrounds that are bright. Importantly, the *true* background in SMALL-LABS is mean (or median) filtered to increase the SNR relative to single background images.

5.5 Validating SMALL-LABS with Simulated Data

To test the scope and performance of SMALL-LABS, we simulated realistic single-molecule data with increasingly difficult realistic backgrounds and compared the measured results from the algorithm to the ground truth input to the simulations. Three different simulated movies were analyzed. The first movie (Fig. 5.2a) has only the simple intensity offset (nonzero dark counts) background common to most EMCCD and sCMOS cam-

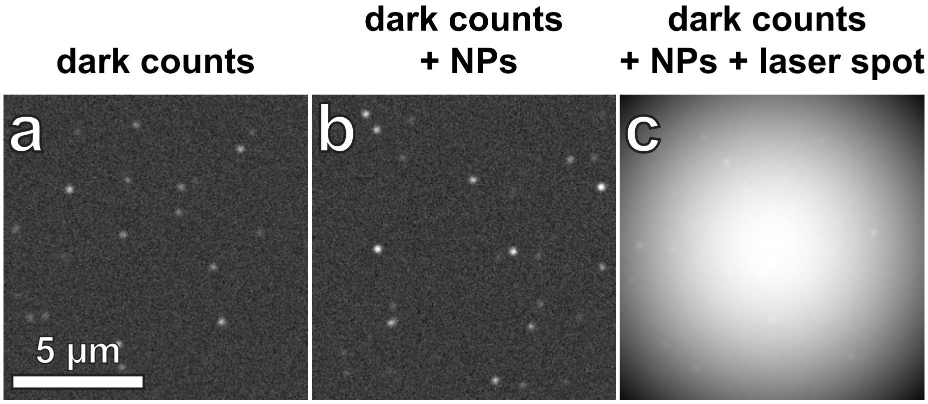

Figure 5.2: Simulated movies with realistic backgrounds.(a) The background consists of only dark counts. (b) The background contains dark counts and static fluorescent nanoparticles. (c) The movie has dark counts, static fluorescent nanoparticles, and a spatially varying background.

eras. In addition to the constant intensity offset Fig. 5.2a, the second movie (Fig. 5.2b) has several static bright background spots identical to fluorophore images in brightness and size, but invariant over time. This background condition is common when fiduciary markers or photoluminescent nanoparticles (NPs) are incorporated into a sample [36, 182, 190]. The third movie (Fig. 5.2c) contains the same background as in Fig. 5.2b, and additionally has a wide, bright Gaussian image overlaid on the entire movie, to mimic the spatially varying background that can result from spatial variations in the excitation laser beam.

The simulated movies were created with signal intensity distributions and noise parameters that realistically occur in single-molecule experiments with fluorescent probes detected on an EMCCD detector [35]. The purpose of this dataset is to test the background removal ability of SMALL-LABS and *not* to push the algorithm to find extremely low SNR molecules or to try to use the algorithm to achieve high-density localization, though these functionalities can certainly be incorporated into the general structure of SMALL-LABS. Thus, the simulated movies contained reasonable SNRs (here defined as the ratio of the single-molecule fluorescence amplitude to the standard deviation of the movie noise) ranging from 1.25 − 10 (see Sec. 5.5.1 for more details), and localizations were well spatially separated as in standard single-molecule data. Furthermore, in accordance with experiments, molecules could stay on for multiple frames (the duration of their emission was given by the absolute value of a normal distribution with a mean of one frame and a standard deviation of three frames). Finally, because their location was randomly determined, molecules could appear at the same location as a previous molecule (like molecules 1 and 4 in Fig. 5.1); in these cases, a simpler algorithm than SMALL-LABS would not remove the background accurately.

As a first measure of performance, we analyzed the ability of SMALL-LABS to accurately detect single molecules. The false-positive and false-negative rates were calculated along with the Jaccard index for the detection of the simulated molecules. The Jaccard index is the ratio of the cardinality (the number of elements in a set) of the intersection between the set of simulated molecules, *S*, and the set of detected molecules, *D*, to the cardinality of the union of *S* and *D* [68]:

$$\text{Jaccard}=\frac{|S\cap D|}{|S\cup D|}=\frac{|S\cap D|}{|S|+\ |D|-|S\cap D|} \tag{5.1}$$

The false-positive and false-negative rates, *FP* and *FN*, respectively, can be similarly expressed:

$$FP=\frac{|D|-|S\cap D|}{|D|} \qquad FN=\frac{|S|-|S\cap D|}{|S|} \tag{5.2}$$

The detection results (after false-positive filtering of the accurate background-subtracted data in Step *V*) of the three movies are presented in Table 5.1. In all three cases, SMALL-LABS performs well as evidenced by a high Jaccard index and low false-positive and false-negative error rates. In particular, *FP* does not increase upon addition in Fig. 5.2b of the

Background	Jaccard	FP rate	FN rate
dark counts	0.903	0.014	0.086
dark counts + NPs	0.905	0.001	0.089
dark counts + NPs + laser spot	0.878	0.016	0.100

Table 5.1: Simulated data detection results. Detection results: Jaccard index, false-positive (FP) error rate, and false-negative (FN) error rate for single molecules in the different simulated movies of Fig. 5.2.

NP background, which is identical in appearance to the molecules. Furthermore, in the case of the laser spot background (Fig. 5.2c), molecule detection without background removal would be extremely limited, whereas most molecules are correctly identified after accurate background subtraction by SMALL-LABS.

In addition to validating the success of SMALL-LABS in detecting molecules, we also analyzed the performance of SMALL-LABS in measuring some important properties of the simulated molecules. In particular, we analyzed how accurately a least-squares Gaussian fit of the background-subtracted molecule images measures the super-resolved molecular positions. We also analyzed how accurately SMALL-LABS measures the intensity of each molecule in each movie. The mean (μ) and standard deviation (σ) of the error distributions for each measured quantity for all molecules in each movie are tabulated in Table 5.2. Full distributions and further details are given in the following section. In all three movies, SMALL-LABS performs well (Table 5.2): all error distributions are centered near $\mu = 0$ and have small σ. Furthermore, the error distributions are fairly insensitive to the nature of the background: there is little change in the statistics between the three movies. Importantly, many approximate background removal approaches introduce a bias ($\mu \neq 0$) in these measured quantities, whereas SMALL-LABS does not introduce any such biases.

Background	x position error (nm)	y position error (nm)	Intensity % error
dark counts	$\mu = 0.165$ $\sigma = 13.7$	$\mu = 0.114$ $\sigma = 13.6$	$\mu = 0.821$ $\sigma = 20.6$
dark counts + NPs	$\mu = -0.112$ $\sigma = 13.7$	$\mu = -0.029$ $\sigma = 13.9$	$\mu = 1.12$ $\sigma = 20.5$
dark counts + NPs + laser spot	$\mu = -0.050$ $\sigma = 14.3$	$\mu = -0.185$ $\sigma = 14.4$	$\mu = 1.64$ $\sigma = 21.2$

Table 5.2: Error distribution characteristics (mean, μ, and standard deviation, σ) for the simulated movies. x and y position error is the difference between the measured and true positions of the molecule. The intensity percent error is [$100\% \times$ (measured − true)/true] for the summed pixel intensities in the local region around the molecule.

5.5.1 Additional Analysis and Simulation Details

The simulated data uses parameters taken from our experiments on the red dye Cy5 visualized at 20 fps in an epifluorescence microscope with a 1.40 NA 100× objective and a 3× beam expander after the objective; these conditions give a 50 nm pixel width on our Photometrics Evolve EMCCD detector. The simulated movies have a frame size of 256 × 256 pixels and are 300 frames long. As is the case for low-brightness optical measurements on an EMCCD camera, the noise was Poissonian (shot noise) for everything except the laser spot itself, which was is bright that it instead has uniformly distributed noise. The intensity offset (dark counts) in all movies is 1040 counts, for which Poissonian noise gives a standard deviation 32.25 counts.

Because most of our experiments are conducted in the red frequency range, each molecule is simulated as a symmetric 2D Gaussian spot with a width (standard deviation) of 100 nm = 2 pixels. The amplitude of the molecules is taken from a normal distribution with a lower bound (Fig. 5.3). We simulate a PAINT experiment, in which each molecule adsorbs non-specifically onto the coverslip at a random position. The integer number of molecules that appear in each frame is taken from a normal distribution with mean = 1 and standard deviation = 3. In a PAINT experiment, each adsorbed molecules will fluoresce for a finite amount of time before desorbing or photobleaching, the molecule on-times (integer number of frames) are also normally distributed with mean = 3 frames and standard deviation = 7 frames.

The fluorescent nanoparticle (NP) background (Fig. 5.2b) was simulated as seven randomly positioned fluorescent spots that were on throughout the entire movie. The NP brightnesses were normally distributed with mean = 350 (SNR = 10.9) and standard deviation = 100 (SNR standard deviation = 3.1). The laser spot background (Fig. 5.2c) was simulated as a Gaussian spot with width (standard deviation) of 200 pixels and amplitude of 2×10^4 counts. Because the laser spot is so bright, it falls outside the regime where Poissonian noise is dominant, and instead this background has simple readout noise, which

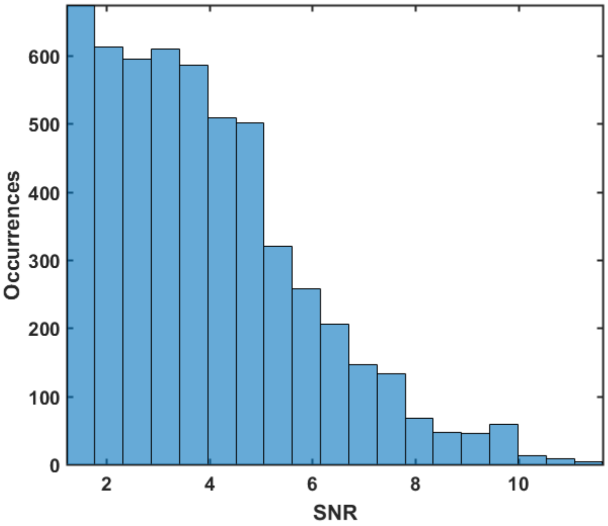

Figure 5.3: Simulated movie SNR distribution. Simulated molecule SNRs in no-background (the dark counts only) movie (Fig. 5.2a). The SNR is here calculated as the brightness (amplitude of the simulated Gaussian) normalized to the noise standard deviation. The molecule brightnesses in the dark counts + NPs and the dark counts + NPs + laser spot (Fig. 5.2b and c respectively) movies followed a similar distribution.

is uniformly distributed from 0 to 200 counts. Representative frames from each movie are shown in Fig. 5.2.

The movies were analyzed using SMALL-LABS. The Matlab function call to run SMALL-LABS to analyze the movies was:

```
SMALLLABS_main('SMALL-LABS\Test data and simulations',...
 7, 151, 100, 'do_avg', 0, 'do_avgsub', 0,'bpthrsh', 94.5)
```

As explained in the User Guide, this function call calculates a running median with a window of 151 frames to do the initial approximate background subtraction. After molecule detection, the accurate background is the median of all the local "off" frames within the surrounding 100 frames. Gaussian PSF fitting then super-resolves the location of the molecules, and the fit parameters are used in a series of checks to reduce to false positives; molecules that survived this check are called goodfits in the code and User Guide. The measured results were then compared to the ground truth input into the simulation.

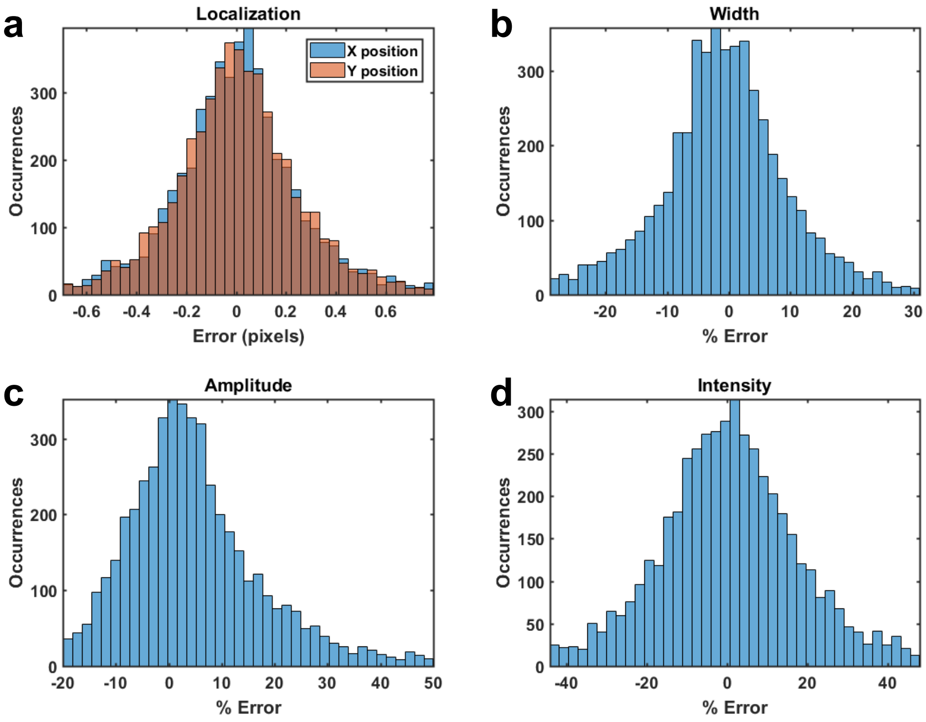

Figure 5.4: Single-molecule analysis for the dark counts only movie (Fig. 5.2a). **(a)** Distribution of the error (in pixels) on the localization (blue: x position, orange: y position). **(b)** Distribution of the percent error on the width. **(c)** Distribution of the percent error on the intensity from the fit. **(d)** Distribution of the percent error on the intensity as measured as the sum of the pixels of the molecule. The mean (μ) and standard deviation (σ) of the error distributions for each measured quantity for all molecules in each movie are tabulated in Table 5.2.

We analyzed detection results to determine how well a least-squares Gaussian fit of the accurate background-subtracted molecules measured the super-resolved positions of the molecules, their widths (Gaussian standard deviation), and the amplitude of the fitted Gaussian. We also analyzed how well SMALL-LABS measured the integrated fluorescence intensity of the molecule. Here, we show the full error distributions that correspond to the results shown in Table 5.2. The results of this analysis are show in Fig. 5.4, Fig. 5.5, and Fig. 5.6, in which the percent error is

$$\%\ \text{error} = 100\% \times (\text{true} - \text{measured})/\text{true} \tag{5.3}$$

Fig. 5.4, Fig. 5.5, Fig. 5.6, and Table 5.2 show that SMALL-LABS performs quite well in all

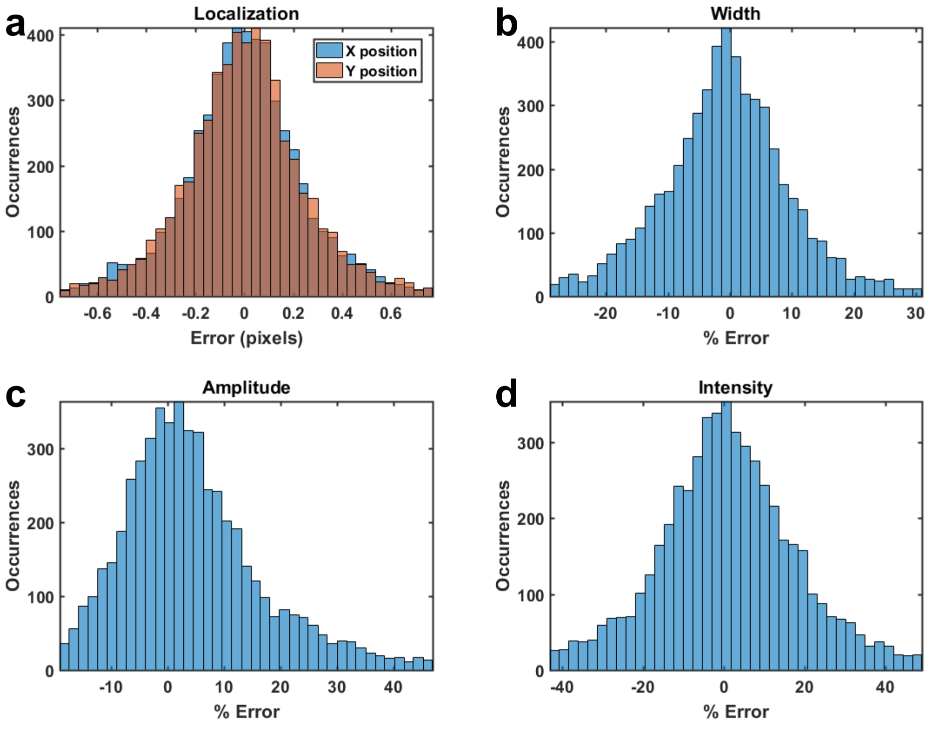

Figure 5.5: Single-molecule analysis for the NP movie (Fig. 5.2b). See the caption of Fig. 5.4 for details.

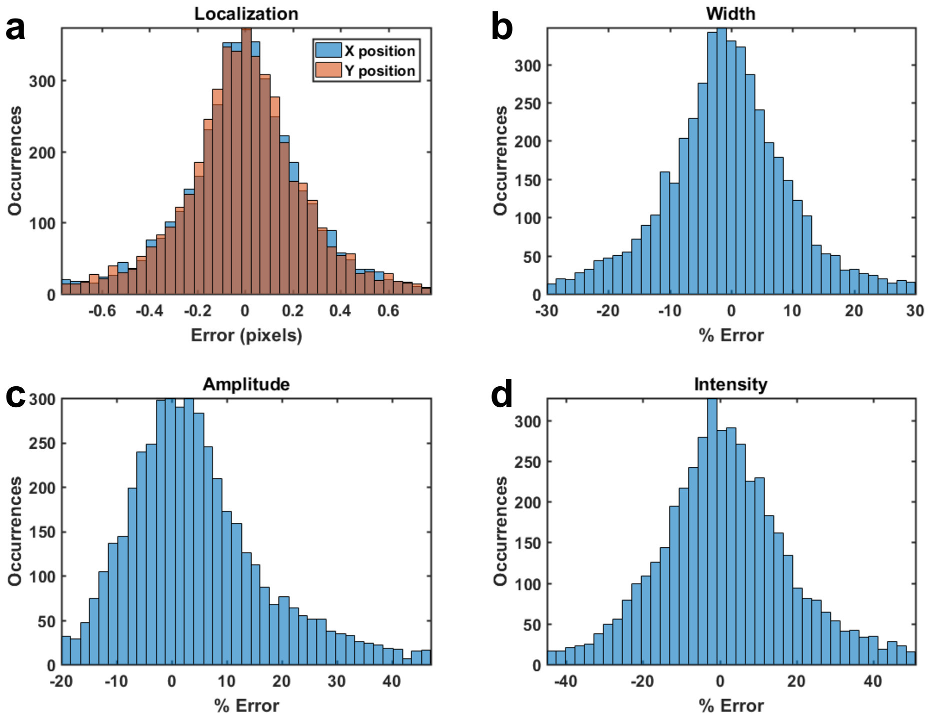

Figure 5.6: Single-molecule analysis for the laser spot movie (Fig. 5.2c). See the caption of Fig. 5.4 for details.

three cases. The measurement results are generally very accurate and bias-free (centered around mean, $\mu = 0$ error).

5.6 Biases Introduced from Incorrect Background Subtraction

The common approach to background subtraction is to subtract a temporal mean or median without first doing foreground detection. The assumption in this background subtraction is that because single molecules will only be emissive during a fraction of the temporal window over which the mean or median is calculated, the molecular fluorescence will not contribute significantly to the time-averaged image. However, the fluorescent molecule will contribute some signal, and the magnitude of the single-molecule localization and measurement biases introduced by this approximate background subtraction will increase with the fraction of temporal window during which the molecule fluoresces; this problem scales with the number and density of single molecules.

5.6.1 Avoiding Bias in a High Density of Single Molecules

To demonstrate how SMALL-LABS avoids bias (systematic offsets), consider the three-frame movie in Fig. 5.7a. In this movie, there is an obscuring background blob, and the fluorescent molecule is present in two of the three frames. When the approximate background is calculated based on a three-frame temporal window (Fig. 5.7b and c), this mean or a median filter gives significant biases in localization and intensity metrics.

Measurement results for the four cases shown in Fig. 5.7 are tabulated in Tables 5.3 and 5.4, where a 2D Gaussian fit gives the position, width (standard deviation), and amplitude. The sum is the sum of all pixel intensities in the local region around the molecule. Simply measuring the raw movie produces large errors in all measured quantities. The position, width, and amplitude from a fit of the data to a 2D Gaussian are inaccurate due to the obscuring background. The intensity calculated by summing the pixels is inaccurate due to both the obscuring background blob and the background intensity offset. Note that the

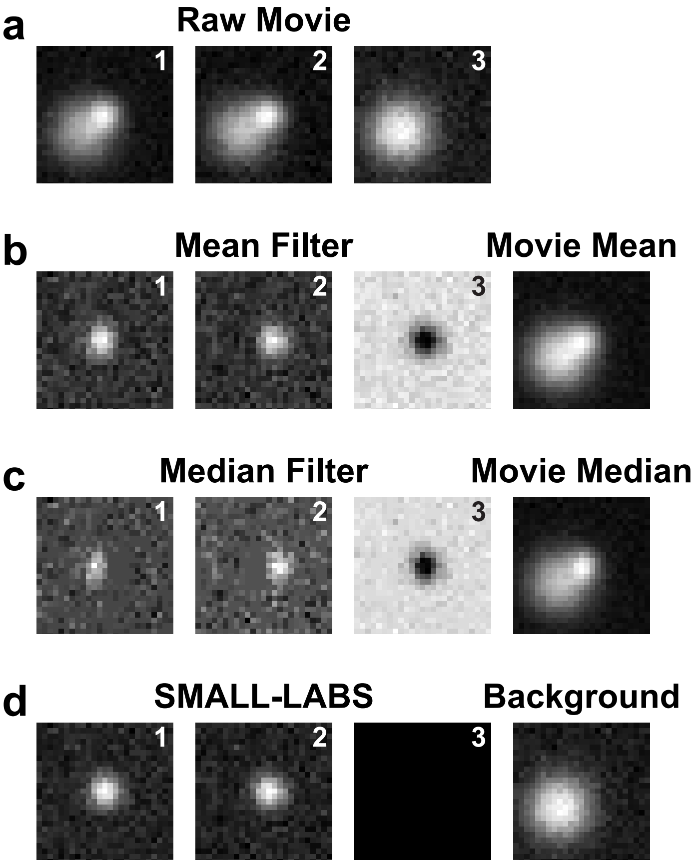

Figure 5.7: High molecule density comparison of BG subtractions. Comparison of different background-subtraction methods for a three-frame movie with a mobile fluorophore; numbers in the top right corners indicate the frame number. (a) The raw image frames of the movie. The fluorescent molecule in frame 1 moves to a slightly different position in frame 2 and then photobleaches in frame 3; all frames contain an intensity offset and an obscuring background blob (frame 3). (b) Approximate background subtraction by subtracting the movie mean (rightmost panel). (c) Approximate background subtraction by subtracting the movie median (rightmost panel). (d) True background subtraction using SMALL-LABS, which in this case this is equivalent to subtracting frame 3 in (a) from all frames.

	x position (px)	y position (px)	Width (px)	Fit Amplitude (a.u.)	Sum Intensity (a.u.)
Ground Truth	13.000	13.000	2.00	100.00	2496
(a) Raw Movie	14.298	11.358	3.50	149.81	6.37×10^5
(b) Mean Filter	13.083	12.311	1.89	39.49	800
(c) Median Filter	13.273	11.236	1.63	27.45	451
(d) SMALL-LABS	13.073	13.043	2.00	100.00	2453

Table 5.3: Measurement bias of molecule 1 for a high density of molecules. Measurements of the position and amplitude of the fluorescent molecule in frame 1 of Fig. 5.7 based on the background-subtraction approaches in Fig. 5.7a – d.

	x position (px)	y position (px)	Width (px)	Fit Amplitude (a.u.)	Sum Intensity (a.u.)
Ground Truth	13.000	14.000	2.00	100.00	2496
(a) Raw Movie	14.443	11.778	4.25	148.70	6.37×10^5
(b) Mean Filter	13.138	14.790	1.97	40.15	852
(c) Median Filter	13.198	15.929	1.62	31.09	502
(d) SMALL-LABS	13.100	14.037	2.06	100.36	2504

Table 5.4: Measurement bias of molecule 2 for a high density of molecules. Measurements of the position and amplitude of the fluorescent molecule in frame 2 of Fig. 5.7 based on the background-subtraction approaches in Fig. 5.7a – d.

ground truth of the sum is not equal to the analytical integral of the 2D Gaussian that was used to simulate the molecules; the volume, V, under a 2D Gaussian curve with these parameters is $V = 2\pi A\sigma^2 = 2513$, whereas the value of 2496 was obtained by summing discrete integer-valued (rounded) pixel intensities in the simulated 2D Gaussian.

Though Fig. 5.7, in which a molecule is on for two frames out of three, seems extreme, this ratio is becoming commonplace as the single-molecule imaging field progresses toward high-density super-resolution imaging by PALM, STORM, or PAINT and toward live-cell imaging of mobile molecules. Overall, detecting one or more fluorescent molecules at different places in the same local region for some number of consecutive frames is not necessarily rare; the likelihood of this occurrence highly depends on the specifics of the imaging and the experimental system. The advantage of SMALL-LABS is that it provides a bias-free measurement regardless of the frequency of occurrence of situations such as Fig. 5.7, and accurate measurements capable of achieving high precision can always be assured.

5.6.2 Decreased Bias in a Low Density of Single Molecules

Within the length of the filter window, if the number of “off” frames is much greater than the number of “on” frames, then the bias introduced by approximate background subtraction goes down significantly. To demonstrate this condition, consider a movie (Fig. 5.8a) which has the same “on” frames as the movie in Fig. 5.7a, but many more “off” frames (28 rather than just one). In this case, mean and median filtering perform quite well; median filtering gives essentially identical results to accurate background removal using SMALL-LABS. Measurements are tabulated in Tables 5.5 and 5.6, where a 2D Gaussian fit gives the position, width (standard deviation), and amplitude. The sum is the sum of all pixel intensities in the local region around the molecule.

	x position (px)	y position (px)	Width (px)	Fit Amplitude (a.u.)	Sum Intensity (a.u.)
Ground Truth	13.000	13.000	2.00	100.00	2496
(a) Raw Movie	14.336	11.354	3.48	148.95	6.37×10^5
(b) Mean Filter	13.030	12.990	1.98	93.91	2252
(c) Median Filter	13.027	13.028	1.98	99.70	2390
(d) SMALL-LABS	13.030	13.022	1.99	100.19	2416

Table 5.5: Measurement bias of molecule 1 for a low density of molecules. Measurements of the position and amplitude of the fluorescent molecule in frame 1 of Fig. 5.8 based on the background-subtraction approaches in Fig. 5.8a – d.

	x position (px)	y position (px)	Width (px)	Fit Amplitude (a.u.)	Sum Intensity (a.u.)
Ground Truth	13.000	14.000	2.00	100.00	2496
(a) Raw Movie	14.416	11.700	4.04	142.03	6.37×10^5
(b) Mean Filter	13.003	14.009	2.02	93.11	2334
(c) Median Filter	13.002	13.983	2.01	99.06	2472
(d) SMALL-LABS	13.005	13.976	2.02	99.38	2498

Table 5.6: Measurement bias of molecule 2 for a low density of molecules. Measurements of the position and amplitude of the fluorescent molecule in frame 2 of Fig. 5.8 based on the background-subtraction approaches in Fig. 5.8a – d.

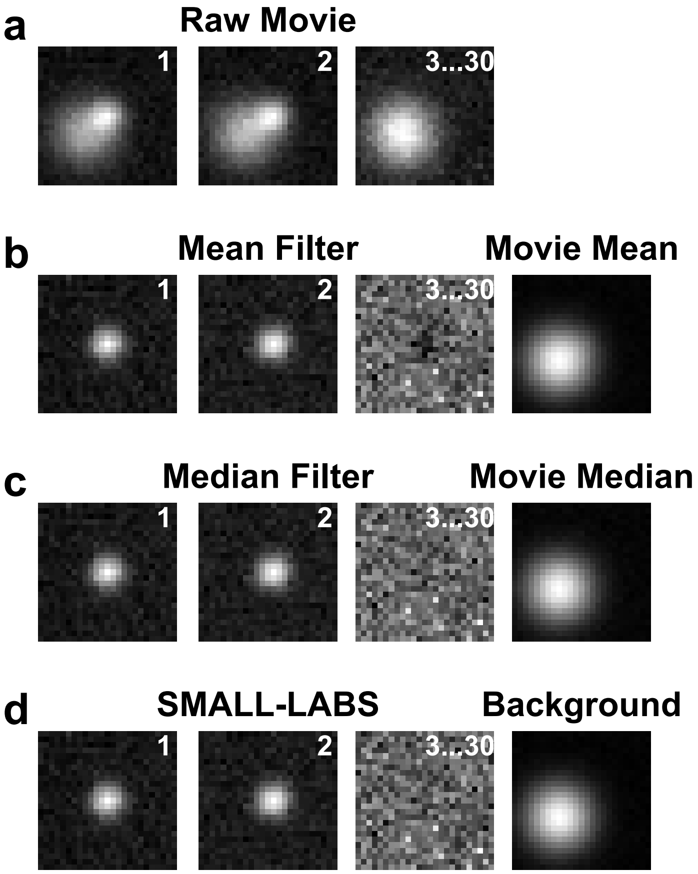

Figure 5.8: Low molecule density comparison of BG subtractions. Comparison of different background-subtraction methods for a thirty-frame movie with a mobile fluorophore; numbers in the top right corners indicate the frame number. (a) The raw image frames of the movie. The fluorescent molecule in frame 1 moves to a slightly different position in frame 2 and then photobleaches; all frames contain an intensity offset and an obscuring background blob (frame 3). (b) Approximate background subtraction by subtracting the movie mean (rightmost panel). (c) Approximate background subtraction by subtracting the movie median (rightmost panel). (d) True background subtraction using SMALL-LABS, which in this case this is equivalent to subtracting the mean of frames 3 to 30 in (a) from all frames.

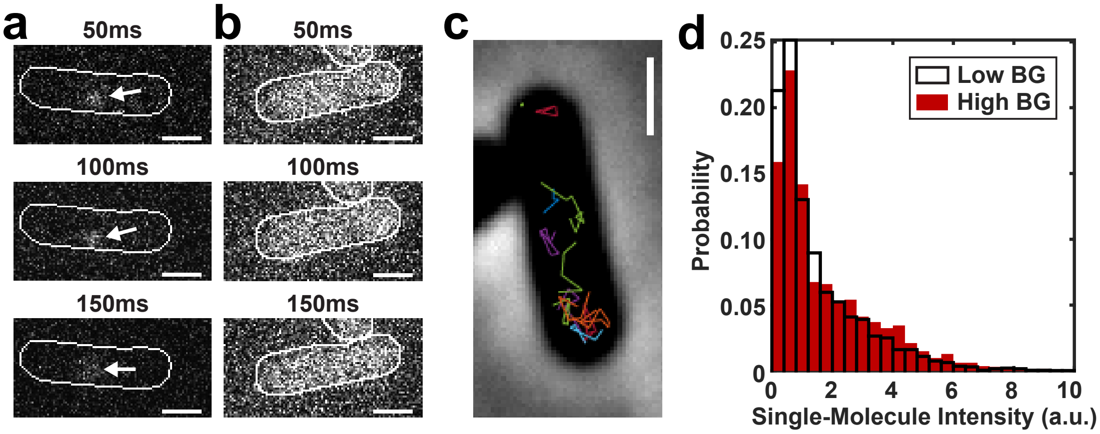

Figure 5.9: Tracking PolC-PAMCherry in living *Bacillus subtilis*. (a) Representative images of a single PolC-PAmCherry molecule (arrow) in a *B. subtilis* cell; the molecule is easily identifiable and can be tracked over time. (b) No PolC-PAmCherry molecules can be identified by eye in high-background experimental conditions. (c) Accurate background subtraction with SMALL-LABS enables single-molecules to be detected and localized from the high-background movie in b, and trajectories are obtained (colored lines). (d) Comparison of the measured single-molecule intensities of the fluorescent protein PAmCherry in live-cell movies with low background (white) and with a high background (red) as in a and b. Scale bars 1 μm.

In the limit that the ratio of "on" frames to "off" during the temporal window used for subtraction is small, mean or median filtering perform fairly well. However, this condition is not generally satisfied in single-molecule imaging due to fluorophores remaining "on" for multiple frames, and thus mean or median filtering will in general introduce significant biases. Therefore, the essential benefit of SMALL-LABS is that it does not rely on a potentially difficult-to-satisfy approximation to guarantee *true* background subtraction.

5.7 Validating SMALL-LABS with Live-Cell Single-Molecule Tracking

To validate SMALL-LABS and demonstrate its scope, we localized single fluorescent proteins in living bacteria cells under optimal single-molecule tracking conditions (Fig. 5.9a) and in conditions that preclude traditional single-molecule detection (Fig. 5.9b). We imaged *Bacillus subtilis* strains natively expressing the DNA polymerase PolC fused to the photoactivatable fluorescent protein PAmCherry as the sole source of PolC (strain JWS213). PolC is one of the two replicative DNA polymerases in *B. subtilis* and has been characterized in our group's previous work [191]. To produce the high background in Fig. 5.9b, a constant 15 W/cm^2, 488 nm laser illumination generated a strong autofluorescent background in the cells; this background was further complicated by its slow decay over time. By stochastically switching a small subset (1 − 3 molecules per cell) of the PolC-PAmCherry molecules into a fluorescent state at a time (in a single-particle tracking/-PALM experiment), we visualized the dynamics of 420 single PolC-PAmCherry molecules in 200 high-background cells (Fig. 5.9b) and 200 single PolC-PAmCherry molecules in 30 low-background cells (Fig. 5.9a).

We removed the subtle background from the low-background movies with SMALL-LABS and then analyzed the sub-cellular single-molecules with super-resolution PSF-fitting. The high-background movies were analyzed with the same algorithm. Whereas the background in Fig. 5.9b is sufficiently high to make single-molecule localization essentially impossible in the raw data, after SMALL-LABS background removal, PolC-PAmCherry could be detected in these cells. Both single-molecule localization data sets were then analyzed with the same single-molecule tracking algorithm: trajectories were determined (Fig. 5.9c) by optimizing all possible pairings of molecules between consecutive frames using the Hungarian algorithm [192–194]. Measured diffusion coefficients for PolC-PAmCherry in the high-background cells matched our previously reported measurements [191] (see Sec. 5.7.1 for more details). Single-molecule intensities, measured by summing the pixel intensities around each measured molecule, yielded nearly identical distributions in the high- and low-background movies (Fig. 5.9d). Both of these results show that SMALL-LABS successfully removed the background in this live-cell imaging experiment and enabled accurate, bias-free measurements of fluorescence intensity and position in a dataset that would have been impossible to analyze without background removal.

5.7.1 Live-cell Imaging and Analysis Details

B. subtilis cells were prepared as previously described [191]. Cells were grown at 30°C to OD ~0.55 – 0.65 in S750 minimal medium supplemented with glucose. 2 μL cell culture was pipetted onto a pad of 1% (wt/vol) agarose in S750, which was sandwiched between two coverslips that had been cleaned by oxygen plasma (Plasma Etch PE-50) for 20 min. The sample was then mounted on the microscope for imaging. In both high- and low-background experiments, PAmCherry was photoactivated by a 200 ms pulse of the 405 nm laser (power density: 100 W/cm^2; Coherent 405-100) and then imaged with a 561 nm laser (power density: 200 W/cm^2; Coherent Sapphire 561-50). The 488 nm laser was not used in the low-background case.

A wide-field inverted microscope (Olympus IX71) was used for imaging, and fluorescence emission was collected by a 1.40 NA 100× oil-immersion phase-contrast objective and detected on a 512 × 512 pixel EMCCD camera (Photometrics Evolve) at 50 ms/frame. Appropriate dichroic and band-pass filters (Semrock) were placed in the light path to reject scattered laser light and maximize the SNR.

The Matlab function call used to run SMALL-LABS to analyze all the live-cell movies was:

```
SMALLLABS_main('DataDirectory', 8, 51, 50, 'do_avg', 0, ...
 'do_avgsub', 0)
```

As explained in the User Guide, this function call uses a running median with a window of 51 frames to do the initial approximate background subtraction. After molecule detection, the accurate background subtraction was calculated as the median of the “off” frames within the surrounding 50 frames. The intensities of the “good fit” molecules from both high- and low-background cells were obtained by summing the pixel intensities in the accurate background-subtracted images of the individual molecules. We observe no significant difference of the intensity distributions in the high and low-background cells

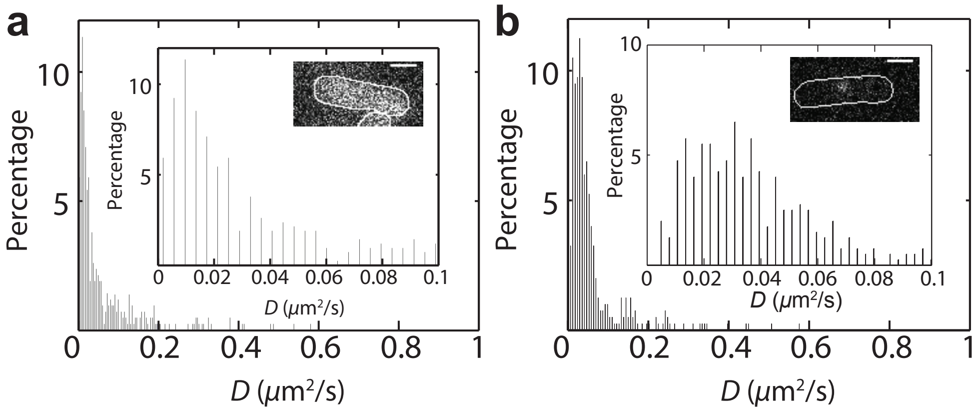

Figure 5.10: Diffusion of PolC-PAMCherry in living *Bacillus subtilis* cells. Apparent diffusion coefficients, *D*, of PolC-PAmCherry in live *B. subtilis* cells. **(a)** Distribution of PolC-PAmCherry diffusion coefficients in cells in high-background conditions. (Inset) Zoom-in on the 0 – 0.1 μm^2/s region of the histogram and a representative frame showing a high-background image. **(b)** Adapted from Liao et al. [191]. Distribution of PolC-PAmCherry diffusion coefficients in cells in low-background conditions. (Inset) Zoom-in on the 0 – 0.1 μm^2/s region of the histogram and a representative frame showing a low-background image. Scale bars: 1 μm.

(Fig. 5.9d).

High- and low-background data sets were analyzed with the same single-molecule tracking algorithm. The trajectories were determined by optimizing all possible pairings of molecules between consecutive frames using the Hungarian algorithm [192, 193, 195]. The likelihood that the two particles are the same molecule in different frames is described in the code by a merit value *m* (`trackparams(1) = 0.01`), which considers the spatial separation (`trackparams(4) = 9`), the intensity difference, and the temporal separation between the two particles (`trackparams(3) = 2.5`). The sum of *m* is maximized for each set of adjacent frames and this maximization is repeated until all frames are processed. The apparent diffusion coefficients, *D*, of single-molecule trajectories were then calculated from the mean squared displacement versus time lag [196]. All trajectories at least 5 frames long were analyzed. The distribution of PolC-PAmCherry diffusion coefficients in high-background cells (Fig. 5.10a) resembles the distribution characterized in low-background cells (Fig. 5.10b).

5.8 Conclusion

In conclusion, SMALL-LABS and the flexible and customizable code we provide can be rapidly implemented to detect and localize single molecules even in the presence of obscuring backgrounds. This data analysis approach requires no changes to experimental methods and in fact, SMALL-LABS relaxes experimental constraints: with its improved accuracy and sensitivity, SMALL-LABS opens up many systems previously inaccessible to super-resolution analysis due to difficult backgrounds. Here, we have demonstrated the scope and performance of SMALL-LABS by accurately and precisely measuring simulated data under a variety of realistic background conditions, and by successfully measuring and tracking single fluorescent proteins in a live-cell experiment under conditions that preclude traditional approaches.

Open-source Matlab code for implementing SMALL-LABS (GNU General Public License), full documentation (User Guide), and a quick-start guide with example data is provided. Code, resources, and further development and expansion of the code post-publication will be hosted at https://github.com/BiteenMatlab/SMALL-LABS.

CHAPTER VI

The Mislocalization Effect

Portions of the work in this chapter have been published in [35–37] as

> E. Wertz, B.P. Isaacoff, J.E. Donehue and J.S. Biteen, "Single-molecule fluorescence unravels the coupling of light to a plasmonic nano-antenna," *Nano Letters*, **14**, 2662-2670 (2015). DOI: 10.1021/acs.nanolett.5b00319
>
> E. Wertz, B.P. Isaacoff, J.S. Biteen, "Wavelength-Dependent Super-resolution Images of Dye Molecules Coupled to Plasmonic Nanotriangles," *ACS Photonics*, **3**, 1733-1740 (2016). DOI: 10.1021/acsphotonics.6b00344
>
> B. Fu, B.P. Isaacoff, J.S. Biteen, "Super-Resolving the Actual Position of Single Fluorescent Molecules Coupled to a Plasmonic Nanoantenna," *ACS Nano*, **11**, 8978-8987, (2017). DOI: 10.1021/acsnano.7b03420

In these works, I mainly contributed the theoretical and computational analysis of the mislocalization effect.

Super-resolution localization of an emitter coupled to an optical antenna results in an inaccurate measurement of the emitter position, we term this the mislocalization effect. I will start this chapter with a brief introduction and history of the mislocalization effect. I will then give a working definition and explain the origin of the effect. Instead of describing all details from our works on this subject (references [35–37]), I will instead focus on

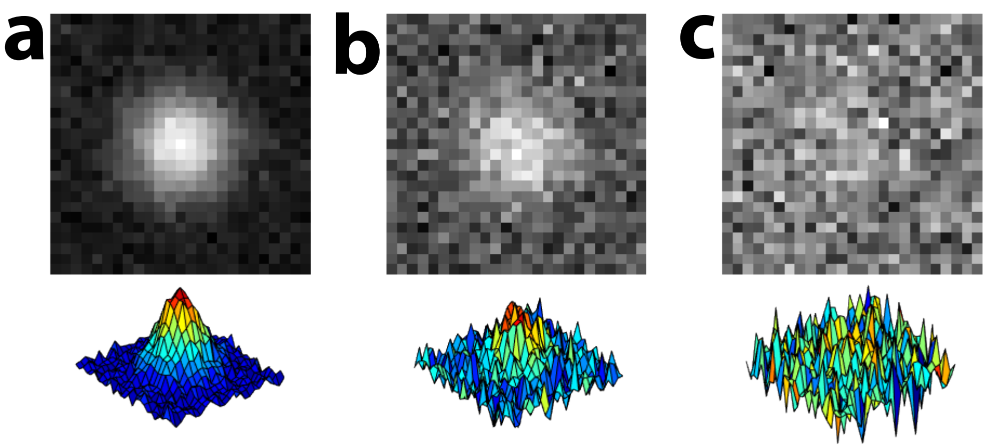

Figure 6.1: Images of molecules with varying SNRs. Top row: images. Bottom row: intensity maps. (a) High SNR (b) Moderate SNR (c) Low SNR.

the takeaways of each project and detail my specific contributions to these projects: the theoretical and computational analysis and prediction of the mislocalization effect.

6.1 The Promise of Plasmon-Enhanced Super-Resolution

As discussed in Chapter II, single-molecule super-resolution microscopy is a powerful technique allowing researchers to make profound impacts in a wide variety of fields. By super-resolving the emission from single emitters on length scales well below the diffraction limit, this technique has opened up many new avenues for scientific research and technological development.

Many realistic experiments (especially *in-vivo*) are unable to achieve the best possible resolutions due to SNR limitations. This was already discussed in the context of Eq. 2.11, which shows that increasing the SNR increases the localization precision. Fig. 6.1 qualitatively illustrates this result by showing images of molecules with varying SNRs. The molecule in Fig. 6.1a is extremely easy to detect, and can be localized with extremely high precision. The molecule in Fig. 6.1b is still fairly straightforward to detect, but will not be localized with as good precision as the molecule in Fig. 6.1a. The molecule image with the lowest SNR, shown in Fig. 6.1c, may be impossible to detect, and if it is successfully detected, will be imprecisely localized.

One approach to increasing the SNR is to increase the signal by increasing the brightness of emitters. As discussed in Chapters III and IV, plasmonic optical antennas *can* increase the brightness of coupled emitters. This idea of using plasmonics to increase the power of single-molecule super-resolution microscopy was (and still is) the impetus behind a lot of plasmon-enhanced fluorescence research [8, 26, 130, 145, 197–201].

On the other hand, as discussed in Chapter III, plasmonics, and optical antennas in general, are themselves technologically important and scientifically exciting. Single-molecule fluorescence super-resolution imaging can directly study the optical properties of plasmonic optical antennas, bringing new insights to this impactful field.

These two sides of the same coin, enhancing super-resolution microscopy with plasmonics and studying plasmonics with super-resolution microscopy, both rely on the assumption that single-molecule super-resolution microscopy provides an *accurate* and highly-precise measurement of single-molecule localization. As we will see in the following sections, when bringing optical antennas into the picture, this assumption breaks down.

6.2 Early Evidence of the Mislocalization Effect

There was early interest in using single-molecule fluorescence super-resolution imaging to map out the subwavelength field confinement about a plasmonic hotspot. Cang et al. [202] used PAINT on rough Al surfaces and on Ag nanoparticle clusters and claimed to have mapped the electric field around the plasmonic hotspot with nm-scale resolution. Their results, shown in Fig. 6.2a and b, generated a lot of excitement. The problem is that a PAINT experiment stochastically and *uniformly* interrogates a surface, eventually giving a near constant spatial density of localizations. However, in Fig. 6.2a from [202], the density of localizations is clearly not uniform, and is in fact highly concentrated near the the hotspot (red circle). They did not mention or explore this puzzling result.

One of the first researchers to raise the alarm about the mislocalization effect was Pro-

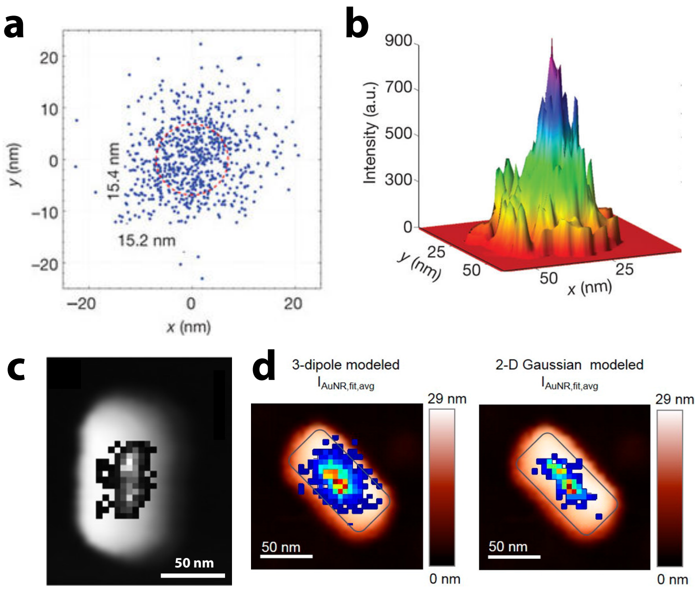

Figure 6.2: Early evidence of the mislocalization effect. (a) PAINT localizations near a hotspot of a rough Al film. (b) Fluorescence intensity of the molecules in a. a and b from [202] ©Macmillan Publishers Limited (c) Density of single-molecule localizations superimposed on an AFM image of a GNR from [185] ©Wiley-VHC (d) Same as c, comparing different fitting functions from [186] ©American Chemical Society.

fessor Katherine Willets. Willets and coworkers noticed systemic biases in reconstructed images of fluorescent dyes attached to GNRs. In these experiments, the dyes were attached to the surface of a GNR and stochastically turned on. One would expect that reconstructing an image from these localizations would accurately reproduce the shape, size, and orientation of the GNR, or possibly over-estimate the size (as the dyes lay outside the GNR). However, what Blythe et al. [185] (Fig. 6.2c) found was that they could accurately reproduce the GNR shape and orientation, but the reconstructions consistently under-reported the GNR size! In their follow-up work Blythe et al. [186] (Fig. 6.2d), tried using modified fitting functions to overcome this bias, but the effect remained. In retrospect, references [186] and [185] are among the earliest (and clearest) evidence in the literature showing the mislocalization effect.

In 2015 Ropp et al. [203] studied the emission from single quantum dots coupled to a plasmonic nanowire, and for the first time, correctly pointed out the mislocalization effect. Very shortly thereafter, we published [35], providing clear evidence and explanation of the mislocalization effect for the more widely applicable system of single fluorescent molecules coupled to plasmonic optical antennas.

6.3 The Mislocalization Effect

A working definition of the mislocalization effect I propose is:

> The **mislocalization effect** refers to the significant inaccuracies in super-resolution localization of an emitter introduced by coupling (even very weakly) the emission from that emitter to an optical antenna.

The mislocalization effect means that if an emitter is at all coupled to an optical antenna, a high-precision super-resolution localization procedure (like PSF fitting) will not return an accurate measurement of where that emitter really is. The most common manifestation of the mislocalization effect is to have the apparent emission shifted towards the antenna position. This shifting towards the antenna explains why the results in Fig. 6.2a (from [202]) failed to show a uniform density of localizations, and instead showed most of the emission coming from the hotspot (antenna) location. It also explains why the results in Fig. 6.2c and d (from [185] and [186] respectively) under-reported the GNR size.

The simplest and most general explanation for the mislocalization effect is that the assumptions underlying super-resolution localization for a free emitter no longer apply when the emission is coupled to an optical antenna. Specifically, for nearly all systems usually under consideration in super-resolution experiments, in the absence of an optical antenna (or photonic cavity) the LDOS around an emitter is nearly uniform and isotropic. Thus, the emitter is free to radiate spherical wavefronts (or dipolar emission, etc.) in any direction equally. Therefore, as discussed in Sec. 2.4.1, such wavefronts produce a diffraction limited imaged shaped as the system PSF. But, because of the anisotropic and nonuniform LDOS around an optical antenna, a single emitter no longer emits in the same way as a free point source, and thus the system PSF *does not* represent the shape of the emission. Therefore, fitting coupled emission to the system PSF gives an inaccurate measurement of the emitter position: mislocalizing the emitter.

6.4 Single-Molecule Fluorescence Unravels the Coupling of Light to a Plasmonic Nano-Antenna

This section is a presentation of the work and results in a collaborative project which we published [35] as:

> E. Wertz, B.P. Isaacoff, J.E. Donehue and J.S. Biteen, "Single-molecule fluorescence unravels the coupling of light to a plasmonic nano-antenna," *Nano Letters*, **14**, 2662-2670 (2015). DOI: 10.1021/acs.nanolett.5b00319

In this collaboration, I developed the theory and performed the calculations. Esther Wertz performed the experiments and analyzed the data. Jessica Flynn (née Donehue) assisted with the experiments. Professor Julie Biteen advised and oversaw the entire project. In this section, I am not reproducing the manuscript, but instead giving an overview of the results within.

6.4.1 Demonstration of the Mislocalization Effect

In [35], we studied the coupling of Cy5.5 dye molecules to electron-beam lithography (e-beam) patterned circular Au nano-island (NI) (a plasmonic optical antenna) in a PAINT experiment. Fig. 6.3a shows a representative SEM image of 90 nm diameter NIs. All NIs were 30 nm thick, and we swept the NI diameter from 60 to 180 nm. As the NI diameter increases, the LSPR redshifts[1] as shown in Fig. 6.3c. The NI LSPR is resonant with both the excitation and emission of Cy5.5 for the 90 nm diameter NI. Fig. 6.3b show the scattering

---

[1] The mechanism of this redshifting is the same as the aspect ratio scaling of a GNR LSPR discussed in Sec. 3.5.

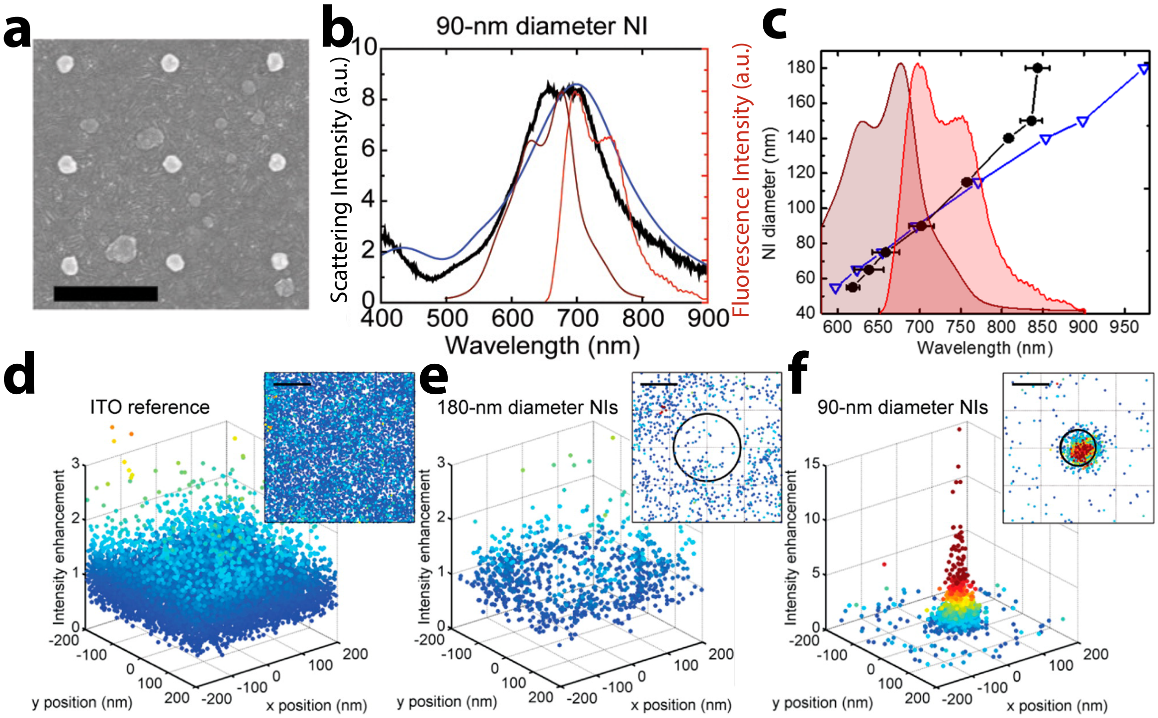

Figure 6.3: Mislocalization on Au nano-islands. (a) SEM image of 90 nm NI, scale bar 500 nm. (b) Scattering spectrum of the 90 nm diameter NI overlaid with the excitation and eimssion spectrum of Cy5.5 (c) Scattering peaks for all NI overlaid on Cy5.5 spectra. In b and c, black is the measured dark-field result and blue is the simulated scattering result. (d) - (f) Single-molecule localization maps. (d) No NI (on the ITO substrate). (e) Off resonance, for a 180 nm NI. (f) On resonance, for the 90 nm NI. Adapted from [35], ©American Chemical Society.

spectrum of the 90 nm diameter NI overlaid with the excitation and emission spectrum of the Cy5.5.

In the absence of a NI, as shown in Fig. 6.3d, dyes adsorbed on the bare substrate (in this case ITO on glass) shows what we expect in a PAINT experiment—a uniform density of localizations. When dyes physically touch a bare metal, their emission is quenched through a charge transfer to the metal [162,165,204,205]. Thus the result in Fig. 6.3e for the 180 nm diameter NI (far off resonance), showing a nearly uniform density of localizations around the NI, and very few localizations on the antenna, is expected. However, in Fig. 6.3f, we see exactly the opposite effect! On resonance, even though we know no dyes can be located on the NI and still emit, nearly all of the emission from the dyes in this PAINT experiment appear to come from the NI location.

This anomalous finding is due to the mislocalization effect. When there is non-negligible overlap between the dye emission spectrum and the optical antenna spectrum—when the emission is coupled to the antenna—the apparent position of emission does not reflect the true position of the emitter. We studied the spectral dependence of this effect in [36], which will be discussed in Sec. 6.5. In the next section, I will detail the Two-Gaussian model, the initial approximate model we developed to predict mislocalization.

6.4.2 The Two-Gaussian Model

The Two-Gaussian model is an approximate model. The biggest approximation is that the model assumes that the measured coupled emission intensity can be modeled as the sum of two 2D Gaussian functions (approximating Airy disks). Indeed, the emission from a single point emitter, such as a single fluorescent molecule *or* a single optical antenna, is well approximated by a 2D Gaussian function, as discussed in Sec. 2.4.1. Thus, in the Two-Gaussian model, we imagine the system like a FRET (Förster resonance energy transfer) system with the emission from the dye centered at the dye position and the emission from the NP centered at the NP. The relative amplitudes of these emissions, like in FRET, are

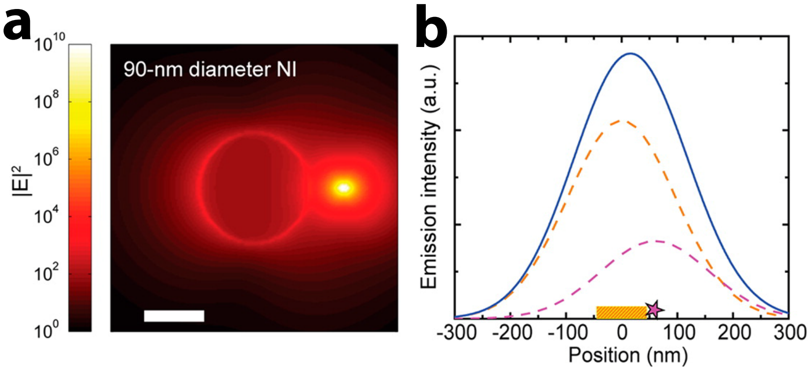

Figure 6.4: Schematic of the Two-Gaussian model. (a) Simulation of the local field intensity around a 90-nm NI excited by a dipole oriented in the x-direction, at a dipole to NI edge distance of 30 nm. Scale bar: 50 nm. (b) The Two-Gaussian model: a Gaussian located at the dye position (purple curve) and a Gaussian located at the NI positon (orange curve) sum to give the coupled emission intensity (blue curve). Adapted from [35], ©American Chemical Society.

given by the extent of coupling; as the coupling increases, so does the energy transfer rate, and thus the Gaussian centered at the NP is given a greater amplitude. The coupled emission is then the sum of these two emission processes. It turns out this model is not generally accurate, and the Two-Gaussian model fails to predict some mislocalization phenomena, though correctly predicting others. This model is however, a good starting point for understanding trends in mislocalization and developing understanding of the effect.

The concept of the Two-Gaussian model is shown in Fig. 6.4. The dye emission process is simulated in the standard manner, by exciting the NI with a dipole source (as in Fig. 3.9c). The electric field intensity distribution about a resonantly excited NI is shown in Fig. 6.4a. Due to the circular symmetry of the NI, we only simulate dipole positions along the radial direction, and similarly, we can perform all of the mislocalization analysis on 1D Gaussian functions, instead of the full 2D Gaussian functions. Using the power fluxes from the simulation (Fig. 6.4a) for a given dipole position and orientation, we calculate (as described below) the amplitude for a Gaussian function located at the dipole position and one located at the NI position. These two Gaussians are then summed to predict the coupled emission intensity. The coupled emission (no longer a pure Gaussian function) is

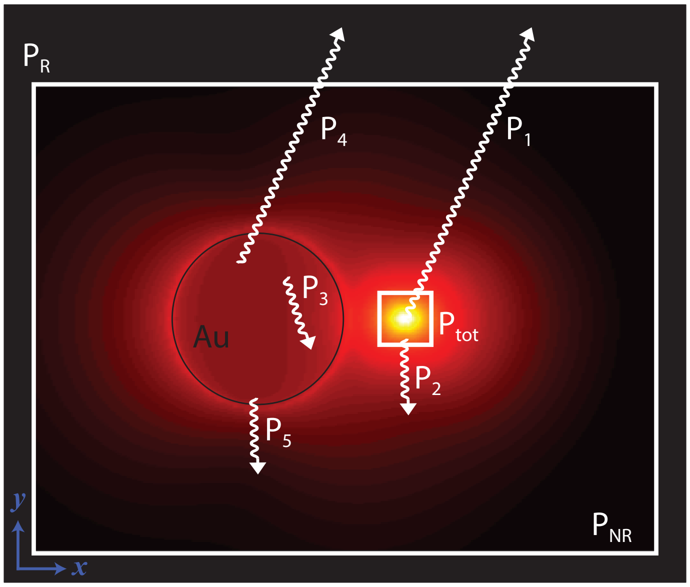

Figure 6.5: Power radiation and dissipation pathways. Pathways overlaid on the field maps from Fig. 6.4a. Adapted from [35], ©American Chemical Society.

then fit to a Gaussian, as in super-resolution localization, to predict the measured apparent emission position.

To calculate the amplitudes of the two Gaussians, we track all of the power radiation and dissipation pathways in the system. The different paths are schematically illustrated in Fig. 6.5. The total power radiated into the far field ($P_R = P_1 + P_4$) and the total power in the simulation ($P_{tot} = P_R + P_{NR} = P_1 + P_2 + P_3 + P_4 + P_5$) are measured in the presence of the NI, and the corresponding reference quantities ($P_R^0 = P_1^0$) and ($P_{tot}^0 = P_R^0 + P_{NR}^0 = P_1^0 + P_2^0$) are measured for a dipole on an ITO substrate. The different dissipation and radiation pathways are:

P_1: power radiated into the far-field directly from the dipole

P_2: the power lost due to nonradiative energy transfer to the environment from the dipole

P_3: the power coupled to the NI and then dissipated due to Au material losses

P_4: the power coupled to the NI and then radiated into the far-field

P_5: the power coupled to the NI and then lost due to nonradiative energy transfer to the environment

The radiated power enhancement, R, is

$$R = \frac{P_R}{P_R^0} = \frac{P_1 + P_4}{P_1^0} \tag{6.1}$$

and the efficiency modification, H, is

$$H = \frac{\eta_a}{\eta_a^0} = \frac{P_r}{P_{tot}}\frac{P_{tot}^0}{P_R^0} = \frac{P_1 + P_4}{P_1 + P_2 + P_3 + P_4 + P_5}\frac{P_1^0 + P_2^0}{P_1^0} \tag{6.2}$$

The power coupled to the NI then radiated to the far field, P_4, normalized by the reference radiated power, P_1^0, is defined as $A_P = P_4/P_1^0$, and as detailed below, in the limit where the dipole is very close or very far from the NI edge, the amplitude of the Gaussian located at the NI, A_p, can be simplified as

$$A_P \approx R - H \tag{6.3}$$

Case 1: Small Dipole Separation Limit

In the limit where the dipole is very close to the NI, there is a lot of coupling. Here, $P_{tot} \gg P_R$ becaues the Au material losses, P_3, scale with the amount of coupling. Additionally, since P_{tot}^0 and P_R^0 differ only by the small losses to the ITO (P_2^0), $P_{tot}^0 \approx P_R^0$, and thus $\frac{P_{tot}}{P_R} \gg \frac{P_{tot}^0}{P_R^0}$. Using this inequality and Eq. 6.2 gives

$$H = \frac{P_R}{P_{tot}}\frac{P_{tot}^0}{P_R^0} \ll 1 \tag{6.4}$$

In this limit, most of the light emitted from the dipole is reradiated through the NI ($P_4 \gg P_1$). Moreover, $P_4 \gg P_1^0$, due to plamson enhanced emission. Then,

$$R = \frac{P_1 + P_4}{P_1^0} \approx \frac{P_4}{P_1^0} \gg 1 \tag{6.5}$$

Combing these two results, we find that

$$R - H \approx \frac{P_4}{P_1^0} = A_P \tag{6.6}$$

Case 2: Large Dipole Separation Limit

In the limit where the dipole is very far from the NI, there is very little coupling between the dye and the plasmon. This implies that $P_3, P_4, P_5 \approx 0$ and therefore $P_1, P_2 \gg P_3, P_4, P_5$. As a result:

$$R \approx \frac{P_1}{P_1^0} \quad \& \quad H \approx \frac{P_1}{P_1 + P_2} \frac{P_1^0 + P_2^0}{P_1^0} \tag{6.7}$$

Furthermore, in this limit, the dipole approaches its reference case behavior where $P_1 \approx P_1^0$ and $P_2 \approx P_2^0$, and so $R \approx H \approx 1$ and consequently, $R - H \approx 0$. Which is consistent with the behaivor of A_P where

$$A_P = \frac{P_4}{P_1^0} \approx \frac{P_4}{P_1} \approx 0 \tag{6.8}$$

and thus in this limit as well

$$R - H \approx A_P \tag{6.9}$$

6.4.3 Applying the Two-Gaussian Model

To apply the Two-Gaussian model, the amplitude of the Gaussian function located at the dipole position is given by H (Eq. 6.2), and the amplitude of the Gaussian function located at the NI is given by A_P (Eq. 6.3). We calculated these quantities at a series of radial separations from the NI edge, r_e. At each location, we simulated x, y, and z oriented dipoles, and then averaged the three results. The Gaussians with amplitude H and A_P were then summed to give a total coupled emission intensity profile, which was fit to a symmetric Gaussian function, and the fit result center of the Gaussian was taken as the prediction for the experimentally measured apparent emission position.

We can now compare the results of the Two-Gaussian model to experiments. Fig. 6.6 compares the experimentally measured radial density of localizations relative to NI cen-

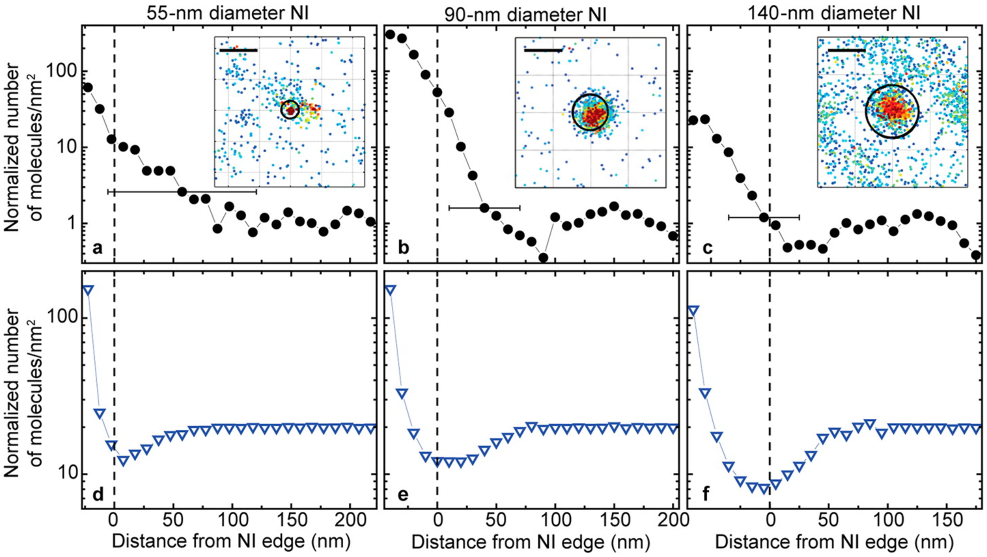

Figure 6.6: Denisty of apparent emission positions. (a-c) Experimentally measured density of Cy5.5 fits as a function of distance from the nearest NI edge for three different NI diameters: (a) 55, (b) 90, and (c) 140 nm. The insets show the corresponding super-resolution maps; the black circles indicate the position of the NI. Scale bars: 100 nm. (d-f) Corresponding simulated results using the Two-Gaussian model. Dashed lines indicate the NI edge positions. From [35], ©American Chemical Society.

ter to the simulated results with the Two-Gaussian model. For all diameters, in both the experimental and simulated data, the maximum number of molecules is found at the center of the NIs, and a depletion ring (dip) appears as a result of the balance of the direct emission from the dye molecule and the coupled emission through the NI plasmon mode. In the simulations, the density far away from the edge of the NI is overestimated compared to the experiments due to the lower detection probability of these dim, uncoupled molecules in the experiments.

Overall, despite being an approximate model, the Two-Gaussian model qualitatively predicts mislocalization. Furthermore, it helps to highlight that the origin of the effect is from variable coupling which produces a false apparent position. In the next section, covering our work in [36], I discard the Two-Gaussian model, and use an exact numerical formulation to predict the measured intensity profile of coupled emission. This new, exact approach, reveals several new insights that the Two-Gaussian model misses.

6.5 Wavelength-Dependent Super-Resolution Images of Dye Molecules Coupled to Plasmonic Nanotriangles

This section is a presentation of the work and results in a collaborative project which we published [36] as:

> E. Wertz, B.P. Isaacoff, J.S. Biteen, "Wavelength-Dependent Super-resolution Images of Dye Molecules Coupled to Plasmonic Nanotriangles," *ACS Photonics*, **3**, 1733-1740 (2016). DOI: 10.1021/acsphotonics.6b00344

In this collaboration, I developed the theory and performed the calculations. Esther Wertz performed the experiments and analyzed the data. Professor Julie Biteen advised and oversaw the entire project. In this section, I am not reproducing the manuscript, but instead giving an overview of the results within.

6.5.1 Spectral Dependence of Mislocalization

In [36], we studied the spectral dependence of the mislocalization effect. We considered three dyes of different colors (Cy3, Cy5, and Cy5.5), excited with four different laser wavelengths (515, 532, 561, and 640 nm), and coupled to a range of gold nanotriangle (NT) with increasing sizes—and therefore increasing LSPR wavelengths—to investigate how the dependence of the fluorescence enhancement on excitation and emission wavelengths affects the emission pattern, and thus the mislocalization, from the coupled dye-nanoparticle system using super-resolution imaging in a PAINT experiment. We fabricated gold NT arrays by e-beam lithography on an ITO-coated glass coverslip. Each of the eight arrays consisted of 50 nm thick NTs arranged with a 500 nm center-to-center pitch and a specific NT side length between 75 and 145 nm, such that each NT array was characterized by a distinct LSPR frequency. Fig. 6.7 shows the spectra of the systems investigated, highlighting the different spectral overlaps and coupling regimes accessible. For instance, Fig. 6.7h suggests that we would see strong excitation enhancement for the 100

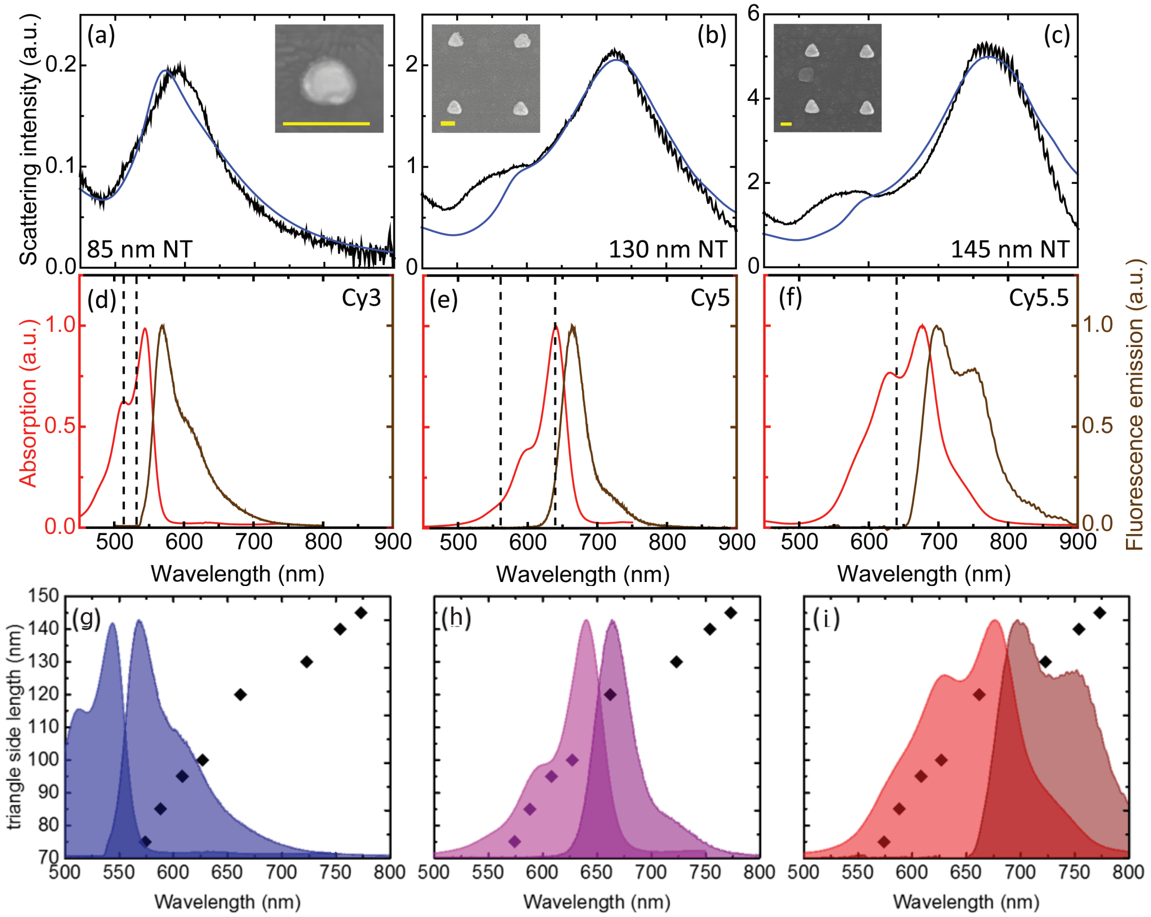

Figure 6.7: NT and dye spectra. (a) – (c), representative NT scatting spectra: measured dark-field in black and simulated in blue. Insets SEM images of NTs, scale bar: 100 nm. (d) – (e), dye spectra with lasers indicated by vertical dashed lines. (g) – (i), dye spectra with LSPR peaks overlaid for different NT sizes. From [36], ©American Chemical Society.

nm NT with the 640 nm laser exciting Cy5, and minimal emission enhancement. Similarly, Fig. 6.7g suggests that for Cy3, excited with either the 515 nm or 532 nm laser, there will be minimal excitation enhancement for NTs, good emission enhancement for NTs smaller than 100 nm, and minimal coupling for the larger NTs. For Cy5.5, Fig. 6.7i suggests that there will be both excitation and emission enhancement for most triangles.

Mislocalization arises from the light emitted by the fluorophore coupling to the antenna. We can therefore take our intuition about emission enhancement, developed in Chap. IV, as our starting point for hypothesizing the spectral dependence of mislocalization—which is mainly dependent on spectral overlap between the LSPR and the fluorescence emission spectrum.

We measured the mislocalization of dyes coupled to the NTs in the same manner as discussed in Sec. 6.4 ([35]). Briefly, we used a PAINT experiment to super-resolve the location of dyes. In a PAINT experiment, the dyes stochastically and uniformly interrogate the surface being studied. Furthermore, if a dye molecule directly touches the bare metal of the NTs, it will be quenched, not emitting any light, and we will not detect the molecule. Therefore, an emission map with a non-uniform density of localizations, and especially any localizations which appear to be located on top of the NT, indicates mislocalization.

The localization maps for some of the different NT-dye-laser combinations are shown in Fig. 6.8. Fig. 6.8a shows the control PAINT experiment on an ITO substrate, with no NT. As expected, the control shows a uniform density of dye localizations. In contrast, when dye molecules couple to the NTs, a strong change in the emission map is observed. For the case of Cy5.5 with 640 nm excitation, Cy5 with 640 nm excitation, and Cy5 with 561 nm excitation (Fig. 6.8b – d, respectively), significant mislocalization is observed. Indeed, though molecules that actually are on top of the NT will be quenched and not detected in the fluorescence microscope, in all three cases, the maximum emission enhancement is observed from molecules that appear from their fits to be on top of the NT, clearly demonstrating the effect of coupling on the far-field radiation pattern. In fact, even when

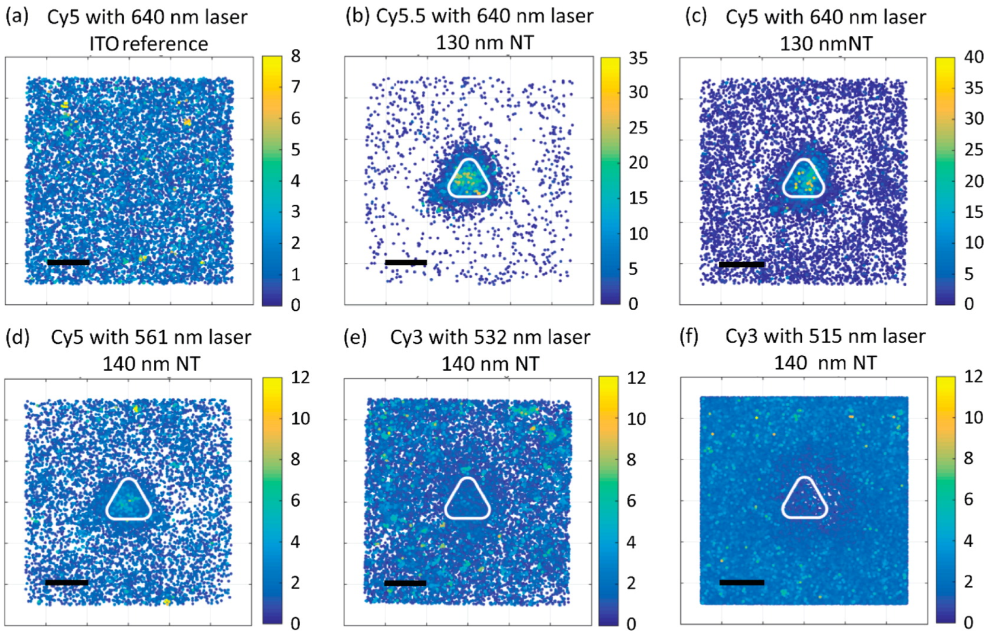

Figure 6.8: Measured dye localization maps about several NTs. (a) Cy5 on ITO reference with 640 nm excitation, (b) – (f), dye molecules near NTs with fluorescence excitation wavelength and NT sizes as indicated. Scale bars: 100 nm. Color bars: Fluorescence intensity enhancement. The white triangles in (b) – (f) indicate the NT position. From [36], ©American Chemical Society.

very little enhancement is observed (Fig. 6.8d), most of the fluorescence fits are located on top of the NT, and fewer molecules appear from their fits to be at the periphery of the NT, indicating that the emission from molecules physically located around the NT is overall shifted toward the NT center. This shifting of the emission toward the NT center happens even when very little enhancement is observed (Fig. 6.8d) and for molecules located up to ~ 100 nm away from the NT, illustrating the robustness of this effect. Additionally, the resulting radiation pattern clearly reproduces the triangular shape of the NTs, giving us structural information on the substrate that is masked by the diffraction limit in standard optical microscopy.

Surprisingly, for the case of Cy3 coupled to a 140 nm NT (LSPR at 750 nm), shown in Fig. 6.8e and f, where there is very little spectral overlap between LSPR and the dye emission spectrum, we still observe mislocalization! The effect is much smaller than in the other cases. For instance, the depletion region showing a lower density of localizations

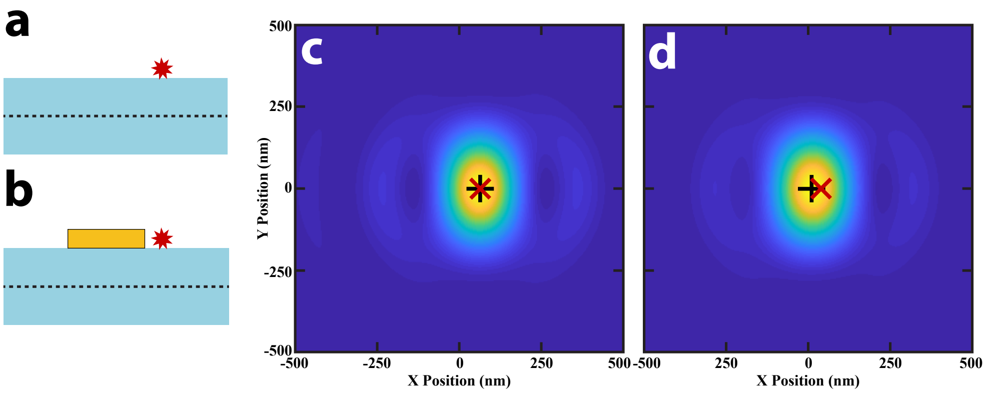

Figure 6.9: Exact mislocalization calculation schematic. (a) The radiation from a dipole source is projected to the far-field from below (measured at the dashed line). (b) Same as (a), now coupled to an antenna. (c) The far-field diffraction limited image of a. (d) The far-field diffraction limited image of b. In c and d, the red × indicates the actual position of the dipole source and the black cross indicates the apparent position of emission.

around the NT is minimally visible in Fig. 6.8e and is not detectable in Fig. 6.8f. However, we still observe many localizations appearing to originate from the NT location, indicating mislocalization.

6.5.2 Exactly Predicting Mislocalization

Though the Two-Gaussian model for predicting mislocalization was successful in matching some of the experimental results in [35], it is an approximate model. Here, I replace the Two-Gaussian model, with an exact numerical approach to simulating the coupled emission. This exact approach has revealed a number of new insights, discussed below.

To exactly predict mislocalization, it is necessary to be able to exactly predict the PSF of the microscope. There has been extensive progress in using electromagnetic simulations, and in particular FDTD simulations, to simulate a microscope—see [129] for a comprehensive review and tutorial on this subject. The basic idea is shown in Fig. 6.9a and b. The radiation from a dipole source is collected in the simulated direction of the objective lens, in this experiment, that means the direction below the source. The radiation is projected to the far field using a near-to-far field transformation. Only the far-field radiation within a certain NA, to match the experiment, is kept; in this case the NA is 1.4. This (truncated hemispherical) far-field radiation pattern is then focused to a plane by spatially Fourier transforming the radiation pattern [129]. The result is a diffraction-limited image of a point source, accurately showing the system PSF.

The calculated diffraction-limited image is then numerically analyzed just as in a super-resolution experiment, in this case by fitting to a 2D Gaussian function. The super-resolved fit result can be compared to the actual position of the dipole source to determine how much, if any mislocalization occurred due to coupling with an antenna. The radiation from a dipole not coupled to an antenna, Fig. 6.9a, is shown in Fig. 6.9c. The fit location (black cross) is exactly located at the true dipole position (red ×), as expected. When the dipole is proximal to an antenna, Fig. 6.9b, the super-resolved fit position, the black cross in Fig. 6.9d, is separated from the true dipole position, showing mislocalization. This simulation approach is now the standard approach to investigating the mislocalization effect [203, 206].

6.5.3 Predicting Spectral Dependence of Mislocalization

To understand the spectral dependence of mislocalization in this experiment, I simulated dyes coupled to the NTs and calculated the mislocalization. Two single dipole emitters (with dipole orientations in the x direction and the y direction, respectively) were placed one at a time about the NT at each position indicated by a blue dot in Fig. 6.10a and mapped by symmetry to the complete set, plotted as red dots. The apparent emission positions of each dipole are plotted as dots in Figure 4b – e after randomly sampling interpolated results to yield the expected distribution of molecule localizations at three different wavelengths corresponding to the emission maxima of the three dyes (700, 670, and 570 nm for Cy5.5, Cy5, and Cy3, respectively). Although no dyes were positioned less than 5 nm away from the NT edge to mimic strong quenching at these very short distances, the simulations clearly reproduce the experimentally observed mislocalization

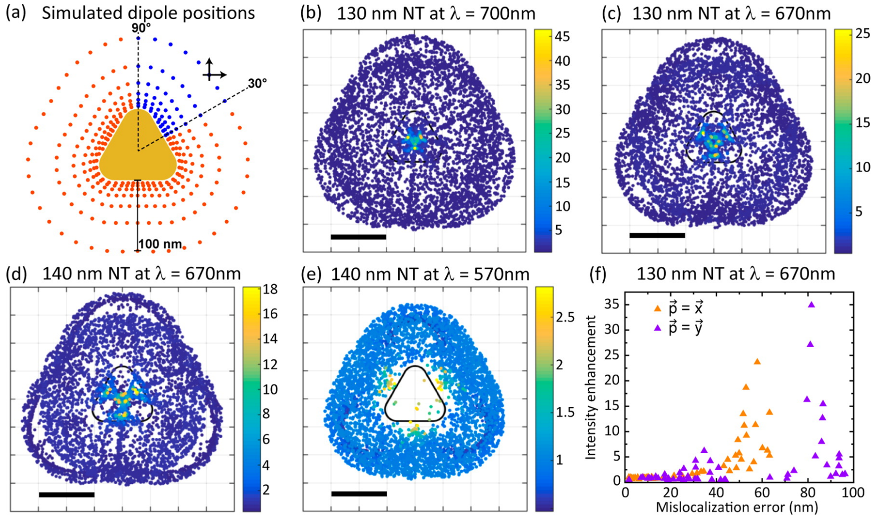

Figure 6.10: Simulations of dipoles coupled to a NT. (a) Simulated dipole positions around an NT (blue dots) were mapped to results for the red dots by symmetry. (b) – (e) Simulated apparent emission positions at three different wavelengths, (c, d) 670 nm/Cy5, and (e) 570 nm/Cy3. Scale bars: 100 nm. Color bars: Intensity of the simulated single-molecule emission. The black triangles indicate the NT position. (f) Simulated intensity enhancement vs. mislocalization error magnitude for dipoles oriented along the x-axis (orange) or the y-axis (purple) at 670 nm near 130 nm NTs as in (c). From [36], ©American Chemical Society.

shown in Fig. 6.8. In all cases, many dye molecules at the NT periphery appear to emit from on top of the NT. For the case of Cy5 coupled to 130 nm NTs (Fig. 6.10c), the simulated intensity enhancement is plotted in Fig. 6.10f against the magnitude of the mislocalization error (the difference between the actual dipole position and the fitted position). Consistent with our experimental results, a strong enhancement correlates with a large shift in apparent position; however there is still significant shifting even in the absence of enhancement.

This exact approach to simulating mislocalization revealed that the mislocalization effect comes from the combined effect of the emission of dyes close to the antenna shifting toward the NT and the emission of dyes far from the antenna predominantly shifting away, resulting in a low density of localizations in the intermediate region. This insight of shifting, both toward and away from a plasmonic antenna, could not have come out of the Two-Gaussian model. To explore this effect in depth, it is instructive to see how each

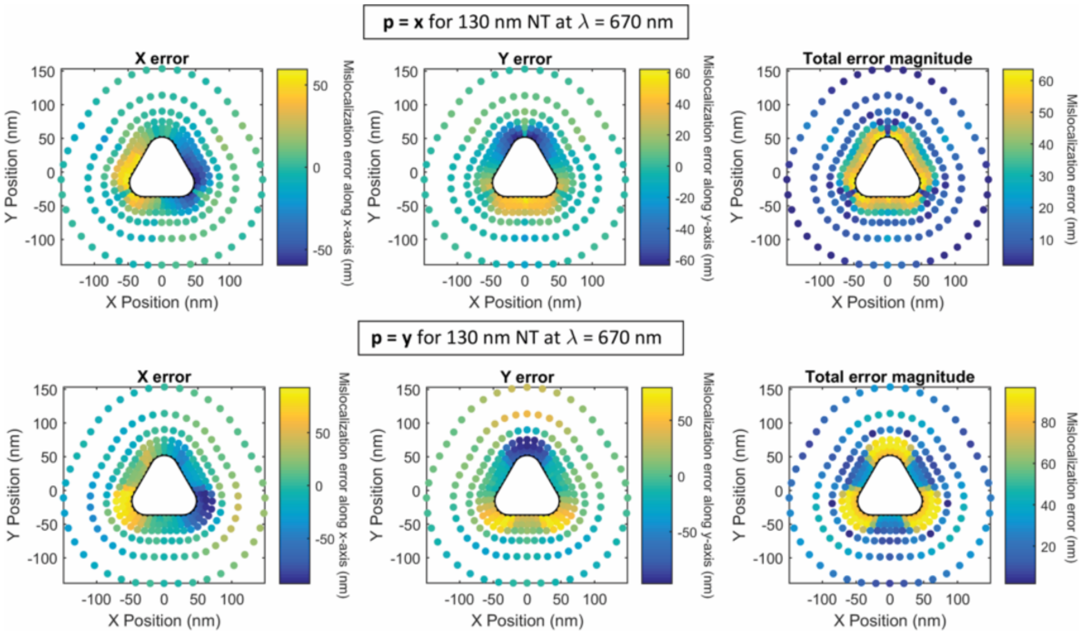

Figure 6.11: Details of mislocalization about a NT. The position error is the difference between the position of the fit and the actual position of the dipole source, i.e., +X indicates that the apparent position is to the right of the actual position. The magnitude of the total error is the length of the vector between the fit position and the position of the source. From [36], ©American Chemical Society.

dipole individually appears to shift from its true position. In Fig. 6.11, the shifting away from the NT occurs predominantly for the dipoles located further away from the NT. Conversely, for the dipoles located near the NT, the shifting is predominantly towards the center of the NT. These simulations also reveal the complex nature of the mislocalization effect, where the mislocalization vector changes quickly over short distances and is highly dependent dipole orientation.

6.6 Super-Resolving the Actual Position of Single Fluorescent Molecules Coupled to a Plasmonic Nanoantenna

This section is a presentation of the work and results in a collaborative project which we published [37] as:

B. Fu, B.P. Isaacoff, J.S. Biteen, “Super-Resolving the Actual Position of Single Fluorescent Molecules Coupled to a Plasmonic Nanoantenna,” *ACS Nano*, **11**, 8978-8987, (2017). DOI: 10.1021/acsnano.7b03420

In this collaboration, I developed the theory and performed the calculations. Bing Fu performed the experiments and analyzed the data. Professor Julie Biteen advised and oversaw the entire project. In this section, I am not reproducing the manuscript, but instead giving an overview of the results within.

6.6.1 Predicting Mislocalization of DNA-Bound Dyes

In [37], we studied the mislocalization of single fluorescent molecules coupled to gold NPs with precise distance tuning via double-stranded DNA. We developed an analytical framework to uncover detailed spatial information when direct 3D imaging is not accessible. Overall, we demonstrated that by taking measurements on a single, well-defined, and symmetric dye/NP assembly and by accounting explicitly for artifacts from super-resolution imaging, we could measure the true nanophotonic mislocalization. We measured up to 50 nm mislocalizations and showed that smaller separation distances lead to larger mislocalizations, also verified by electromagnetic calculations. Overall, by quantifying the distance-dependent mislocalization shift in this gold NP/dye coupled system, we showed that the actual physical position of a coupled single emitter can be recovered.

Here, I will not go into detail discussing the results of the paper, and how we were able to experimentally relate the mislocalized position to the actual position, all of which is described in [37]. But rather, here I will focus on showing that this exact method for predicting mislocalization can be successfully applied to a very different system than the two previously discussed in this chapter. I will also show some surprising new insights that this theoretical framework uncovered.

In the previous two sections, we looked at mislocalization of dyes resolved in a PAINT experiment coupled to e-beam fabricated antennas. In this section, we studied mislocal-

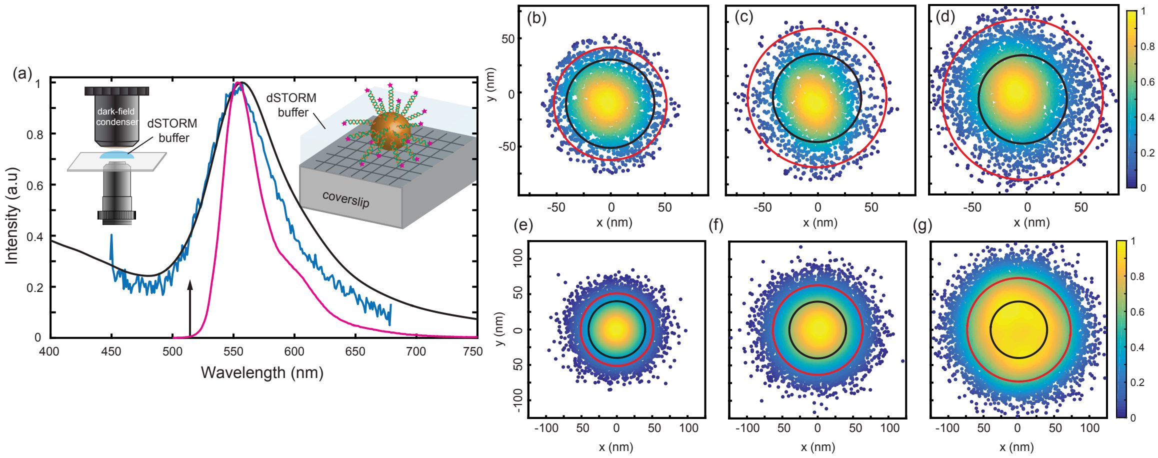

Figure 6.12: Mislocalization of DNA-bound dyes. (a) Scattering of Au NP, measured dark-field in blue, simulated in black, overlain with ATTO532 emission spectrum. Insets are schematics illustrating experimental design. Dyes are dound to a Au nanosphere with a DNA linker in a dSTORM setup. (b) – (d), localizations about a 78.6 nm NP/dye assembly with a 11 nm (b), 22.8 nm (c), and 32.6 nm (d) dsDNA spacer. (e) – (g), simulations of (b) – (d). From [37], ©American Chemical Society.

ization of dyes bound to the surface of a colloidal Au nanosphere with variable length double-stranded DNA (dsDNA) linkers. Emission from single molecules was achieved in a direct-STORM (dSTORM) experiment. Fig. 6.12a shows the basic experimental setup: ATTO532 dye molecules (pink stars) are attached with dsDNA to the Au nanoparticle (NP) and single-molecule imaging was accomplished by inducing blinking with a dSTORM buffer [207–210]. The emission spectrum of ATTO532 overlaps with the LSPR of the NP, shown in Fig. 6.12a, and thus we expect to observe significant mislocalization.

From our previous studies of mislocalization, we know that the separation between the emitter and the antenna is a crucial parameter affecting mislocalization. Fig. 6.12b – d shows the localization density in the xy plane about the Au NP for varying lengths of the dsDNA spacer, where the sphere surface is shown by the black circle and the dye location in the same plane is shown by the red circle. Fig. 6.12e – g show the simulated results for the same system. Though there are some differences, largely, the simulations accurately reproduce the experimental results, showing that this mislocalization calculation method

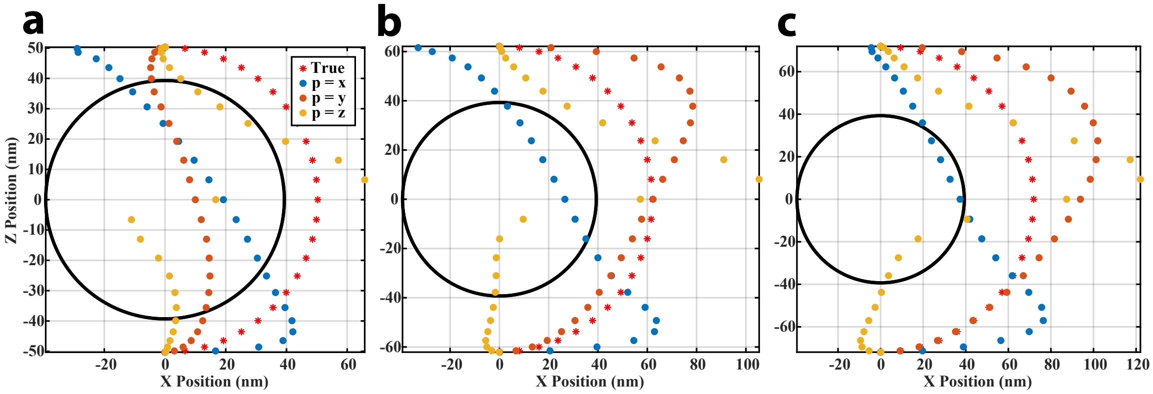

Figure 6.13: z-dependence of mislocalization about a sphere. The true position of the dipole source is shown with a red star, the mislocalized position of the $\mathbf{p} = \mathbf{x}$ (blue), $\mathbf{p} = \mathbf{y}$ (orange), and $\mathbf{p} = \mathbf{z}$ (yellow) dipoles are overlaid. dsDNA linker length is (a) 11 nm, (b) 22.8 nm, and (c) 32.6 nm.

can be applied to diverse systems interrogated with different single-molecule techniques.

One of the main difference between this dSTORM experiment and the PAINT experiments described in the previous sections, is that we were able to investigate 3D effects of mislocalization. The 3D aspects were in fact a big part of how we were able to back out the true position, even in the presence of significant mislocalization in [37]. What I want to focus on here though, is a surprising result we found by looking in three dimensions.

Due to the high symmetry of a sphere, to sufficiently simulate all possible positions of dyes attached to the sphere surface for a given length of linker, we only needed to simulate positions along a concentric circular arc at the appropriate radius. Our coordinate system in this experiment is defined as the coverslip (Fig. 6.12a) lying in the xy plane, and the optical axis along the z axis. Therefore, our system is entirely symmetric in x and y, but the objective lens (imaging from below, along the z axis) breaks the symmetry in z. The simulated points were spaced along a concentric circular arc in the xz plane (where x is now an arbitrary axis orthogonal to z), and all measurable (in the simulation) mislocalization occurred in x direction. Fig. 6.13 shows the z-dependence of the mislocalization for dipole sources oriented along all three Cartesian coordinate directions (x, y, and z) and for the three different linker lengths. Previously, we had understood that the main geometric consideration for a given dipole orientation was simply its separation from the antenna. However, in this experiment, the dyes are always located the same distance from the antenna. Fig. 6.13 clearly shows, that the objective lens breaking the symmetry vertically has a huge effect. There is a big difference in mislocalization for a dipole above and below the antenna. Furthermore, as the z-position changes, the mislocalized result changes rapidly, and as before, this effect is strongly dependent on the dipole orientation.

In this chapter I introduced and described the super-resolution emission mislocalization effect. I presented three of our works on this subject: [35–37]. In this chapter I detailed how to theoretically and computationally understand and predict the mislocalization effect. In order to realize the potential benefits of incorporating optical antennas into super-resolution experiments, the mislocalization effect will need to be overcome. The work presented in this chapter is an important starting point for achieving this goal.

CHAPTER VII

Polarization Dependence of GNR Coupled Fluorescence

In Sec. 3.5, I introduced gold nanorods (GNRs) and detailed why they are scientifically and technologically important plasmonic optical antennas. In this chapter, I describe experiments I performed studying the excitation polarization dependence of fluorescence enhancement of single molecules coupled to single GNRs, and I compare these experimental results with theoretical predictions I calculated using the framework laid out in Chap. IV.

This study is important to undertake along several dimensions. Firstly, given the level of specificity and precision these experiments achieve, they present an unparalleled opportunity to compare with theoretical predictions. Secondly, they add depth to a range of applications involving optical antennas and GNRs. Many GNR applications and technologies rely on the polarization response of the GNR [135, 138, 139, 142, 211, 212], and in particular, polarization is essential to the vast range of GNR based orientation sensor technologies [213–218]. Understanding how the GNR polarization response affects coupled single emitters therefore opens new avenues for these established approaches. Conversely, many applications coupling single emitters to optical antennas have not yet used polarization as an additional dimension of control or information—this work adds a new tool to expand these already established applications.

7.1 Experimental Methods

GNR samples were fabricated by drop casting GNRs onto a labeled-grid microscope coverslip (discussed below) and then rinsing to remove any GNRs not strongly attached to the surface. Colloidal GNRs, CTAB solubilized, were purchased from Nanopartz Inc. The GNRs have a diameter of 50 nm. The particles were synthesized to have a length of 100 nm, which would put their LSPR around 700 nm. However, the nanoparticle synthesis is inexact and produces a range of lengths (the diameter is well specified in this process) and corresponding LSPRs.

Measuring specific nanoparticles over the course of many different experiments is an extremely challenging task without the appropriate tools. To ensure that I was able to repeatedly come back to the same nanoparticles, I needed to use a micron-scale reference system. All of the available commerical products for this purpose were either too large, with features on the length of scale of hundreds or thousands of microns, or they were not compatible with our microscope (for instance a TEM grid). To address this need I developed a photolithography protocol for fabricating a micron-scale labeled grid on a thin glass coverslip. Fig. 7.1 shows an image taken in dark-field of the labeled grid with GNRs. Each grid point is composed of an asymmetric cross with two numbers. One number indicates the row and the other number indicates the column. The cross and numbers are together chiral, ensuring that this grid provides unambiguous location and orientation regardless of the coverslip orientation (rotation, viewed from above or below, etc).

The LSPR of individual GNRs were characterized using dark-field scattering spectroscopy. GNRs were illuminated with white light from a tungsten-halogen lamp through a dark-field condenser (NA $= 1.2 - 1.4$) and the scattered light was collected with a 100× adjustable objective set to NA $= 0.6$. The collected light was dispersed through a spectrometer (SP2300, Princeton Instruments) onto an EMCCD camera (Ixon3 897, Andor Technologies, Ltd). Spectra were corrected by dividing the background-subtracted raw GNR scattering by the bright-field white light spectrum (collected with NA = 1.3). The

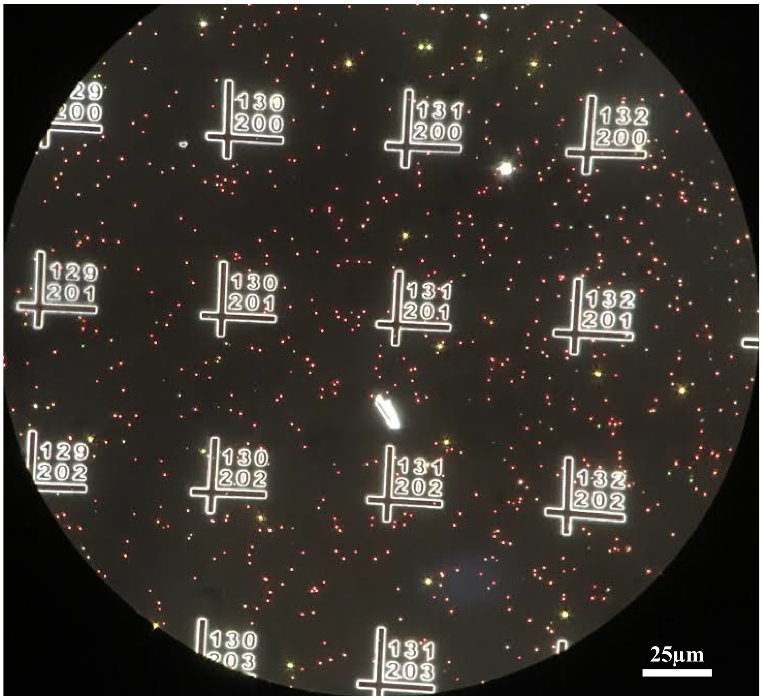

Figure 7.1: Labeled grid with GNRs. In dark-field, the GNRs (red dots) and the grid are easily visible. The labeled grid allows individual nanoparticles to easily be located in a range of different experiments.

scattering peak locations were determined by Lorentzian fits.

Widefield epifluorescence images of single Cy5.5 molecules were acquired with an Olympus IX-71 inverted microscope. The sample was illuminated by a 100×, NA =1.49 oil-immersion microscope objective with 640 nm CW laser excitation (Coherent CUBE 640-40C) at 570 μW; the single-molecule fluorescence was collected through the same objective. An appropriate long-pass filter (Semrock BLP01-635R) and dichroic mirror (Semrock Di01-R635) in the collection pathway rejected scattered laser light, and the image was projected via a 3× beam expander onto an EMCCD camera (Ixon 887, Andor Technologies, Ltd). Images were recorded at an integration time of 100 ms, with electron-multiplying gain set to 255. Laser polarization was set with a linear polarizer (LPVISB050, Thorlabs Inc.), and rotated with a half-wave plate (AHWP10M-600, Thorlabs Inc.).

Single-molecule imaging movies were recorded in a PAINT experiment. Briefly, a low concentration dye solution (1 nM) was placed on top of the GNR sample. As dyes diffused in solution they moved too fast to be imaged as single punctate spots. However, upon adsorbing to the surface, dye molecules were stationary long enough to be detected. Individual movies were 4000 frames long. For each movie the laser linear polarization was fixed, and the polarization was changed from movie to movie. Continuous measurements over weeks was enabled by RoboScope, detailed in the following section.

7.1.1 RoboScope

As introduced in Chap. IV, plasmon-enhanced fluorescence is an extremely local phenomenon (on the scale of nanometers). For a given polarization, most of the large enhancement occurs within just a few nanometers of the GNR surface and in only a small angular region. Therefore, in a PAINT experiment where the dye concentration needs to be low to ensure single molecules are isolatable, it takes a long time to record a sufficient number of events to give statistical information about the distribution of enhancements about a GNR. To address this difficulty, I developed an automation system to run the experiments and manage the microscope. I call this system RoboScope.

RoboScope is open-source Matlab software, which is easily adaptable to wide range of single-molecule experiments, RoboScope is available at https://github.com/bpisaacoff/RoboScope. Roboscope uses Micro-Manager [219, 220] (open source Microscopy software) for several tasks. With RoboScope, these experiments are able to run unsupervised for days at a time. The important components of RoboScope necessary for this experiment are shown in Fig. 7.2.

To keep the dye solution maintained, both replacing solution that evaporated and replenishing the dye molecules on the sample to replace bleached molecules, syringe-pumps were used to add dye solution. A custom mL-scale reservoir was placed on top of the coverslip and sealed with vacuum grease. The reservoir had an entrance and exit port for tubes connected to two 60-mL syringes, each with their own pump. RoboScope maintained the dye solution by removing a small amount of dye (150 μL) with the waste syringe and

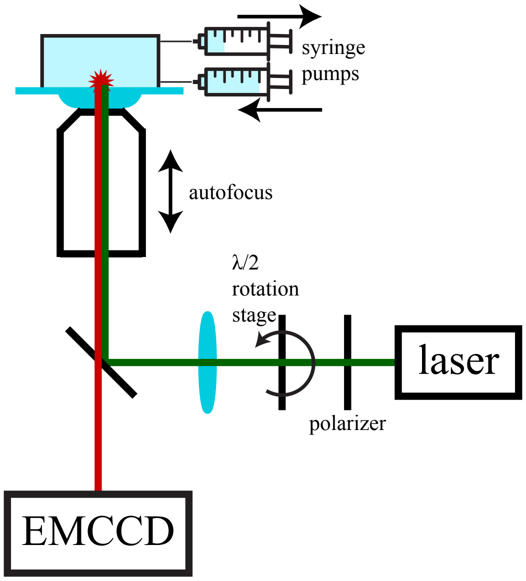

Figure 7.2: RoboScope schematic.

then adding that same amount of dye from the fresh syringe. Because only a very small amount of dye was added, the 60 mL syringe held enough dye for several days of experiments. Emptying and refilling the syringes was the limiting factor for how long the experiments could run unsupervised.

RoboScope is capable of autofocusing the microscope for a range of samples. The autofocus procedure I developed for RoboScope uses image analysis, and thus is compatible with all imaging experiments. The only additional hardware needed for autofocusing is a piezo stage which can move the objective towards and away from the sample or move the sample relative to the objective. The autofocus algorithm takes an image (or a series of images for better SNR) at a series of z planes defined by the user.

For each z plane, an autofocus scoring metric is calculated. To use RoboScope to autofocus different samples, one simply needs to select an appropriate scoring metric. I found that standard autofocus scoring metrics, for example the kind that are used in modern cameras, which usually are based on variants of line or edge sharpness maximization did not work for single-molecule imaging (due to the low SNR and lack of extended features). Instead, I developed a simple autofocus score which, when maximized, reliably focuses a single-molecule imaging experiment. The score is the standard deviation of pixel brightnesses for the top 10% of the brightest pixels. The z plane with the maximal score is then further precisely determined by fitting a Gaussian function to determine the exact score peak location.

RoboScope was also connected to a motorized rotation stage (PRM1Z8, Thorlabs Inc.) to automatically rotate the half-wave plate, and could therefore set the excitation polarization angle for each movie. Finally, RoboScope was connected to the EMCCD camera and was capable recording movies.

7.2 Experimental Details

In this experiment, I measured three specific GNRs. Dark-field scattering spectra showing the LSPR of each GNR is shown in Fig. 7.3a – c. These GNRs were chosen because their LM LSPRs are resonant with the 640-nm laser. The GNRs have LM LSPRs (as measured by fitting a Lorentzian to the LM peak) at 635 nm (GNR #1, Fig. 7.3a), 645 nm (GNR #2, Fig. 7.3b), and 650 nm (GNR #3, Fig. 7.3c). Though each GNR has a slightly different LSPR, they are sufficiently close to be approximated as having the same resonance, and thus single-molecule measurements coupled to each individual GNR are collapsed to a single set of measurements. I simulated the GNR with diameter 50 nm and length 85 nm. The length was chosen by matching the simulated the scattering spectrum to the measured dark-field spectra.

In this experiment looking at the excitation polarization dependence of fluorescence enhancement, it is most meaningful to compare the polarization angle to the angle to the GNR longitudinal axis. To determine the orientation of the GNR longitudinal axis, I measured the GNR intrinsic photoluminescence (PL) intensity as a function of excitation polarization angle. PL was recorded in an imaging experiment as described above, with movies at each polarization angle recorded for 100 frames. The median intensity (sum of pixels in a 7×7 pixel box about the GNR) of each GNR was calculated for each movie. The

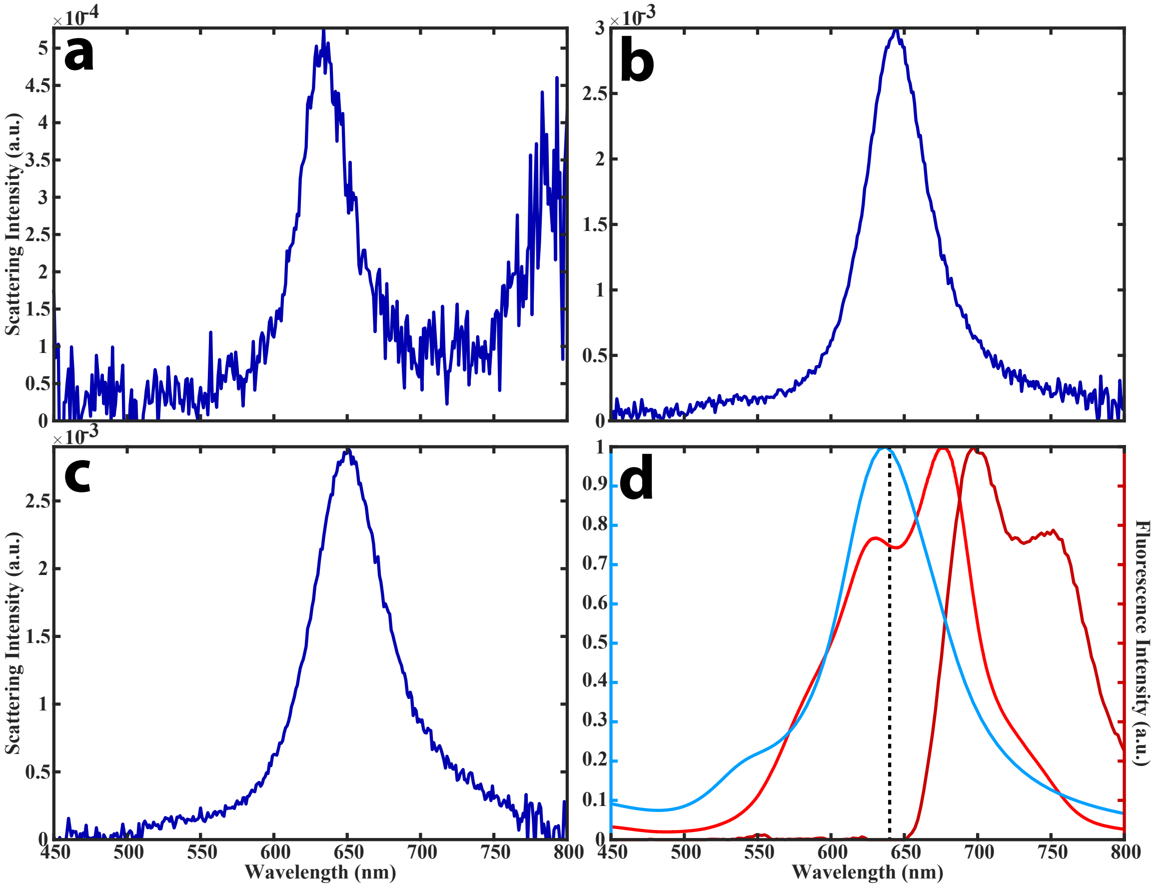

Figure 7.3: GNR and Cy5.5 spectra. (a) – (c) Dark-field scattering spectra of (a) GNR #1, (b) GNR #2, and (c) GNR #3. (d) Simulated GNR scattering (light blue) of a 50 × 85 nm GNR, and measured Cy5.5 excitation (light red) and emission (dark red) spectra. The excitation laser wavelength is indicated by the dashed line.

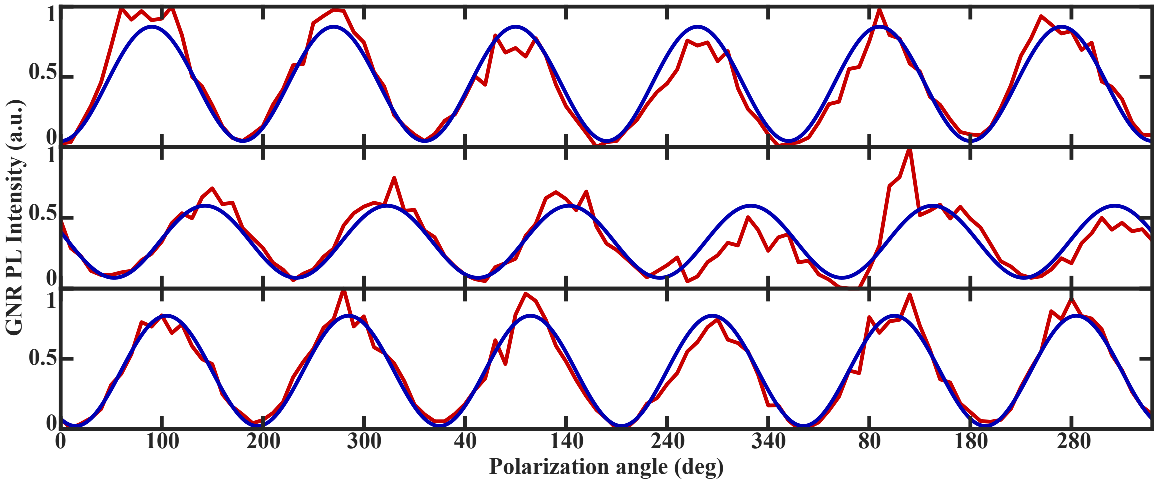

Figure 7.4: GNR PL as a function of excitation polarization. Top plot: GNR #1 (Fig. 7.3a). Middle plot: GNR #2 (Fig. 7.3b). Bottom plot: GNR #3 (Fig. 7.3c). The measured data is in red, and the fits are in blue.

excitation polarization angle was changed by rotating a half-wave plate after a fixed linear polarizer. Fig. 7.4 shows the measured intensity for each GNR as a function of excitation polarization angle. Each PL measurement was fit to a sinusoid with amplitude I_0 and offset I_{off},

$$I(\varphi) = I_0 \cos^2(\varphi - \varphi_{\text{GNR}}) + I_{\text{off}} \tag{7.1}$$

where φ_{GNR} is the GNR longitudinal axis orientation in the excitation polarization basis. It is important to note that the period in Eq. 7.1 is fixed at 180°, enforcing the symmetry of the GNR. Though this fit can provide some interesting information about the GNR PL and the GNR 3D orientation [221], I am only concered with its 2D orientation (azimuthal angle), and φ_{GNR} is the only fit parameter kept. The three GNRs are oriented at at 90° (GNR #1, Fig. 7.3a), 140° (GNR #2, Fig. 7.3b), and 100° (GNR #3, Fig. 7.3c). In this chapter, I maintain the coordinate system laid out in Chap. IV, where the GNR longitudinal axis is oriented along the y-axis (90°), and thus GNR #2 and #3 will have their coordinate systems adjusted accordingly (for example, an experiment for GNR #3 at 70° will be shifted to 60° for the combined group).

The GNRs were coupled to Cy5.5 in a PAINT experiment as described above. The excitation and emission spectra of Cy5.5 are shown in Fig. 7.3d. The excitation spectrum of Cy5.5 is resonant with the GNR LSPR, which also overlap with the laser. Therefore, we expect to see a strong effect from the excitation polarization, because the main mechanism of enhancement is excitation enhancement, and we would expect little emission enhancement.

The experiments were performed using RoboScope to record a series of movies at different excitation polarization angles, keep the movies focused, and replenish the dye. The workflow for this experiment is as follows. To avoid any biases, the different excitation polarization angles were investigated in a random order (halfwave plate 0° to 90° in 5° steps, giving polarization angles of 0° to 180° in 10° steps). After each set of polarization angles was completed, a new random set was generated. After every two movies, spent dye solution was removed and fresh dye solution was added. After the dye was added, the autofocus procedure was run, using a goodness of fit criterion on the Gaussian fit to autofocus scores to ensure that the image was truly optimally focused.

7.3 Data Analysis

Single-molecule movies were analyzed using SMALL-LABS (Chap. V). A running median with window length of 150 frames removed the approximate background, and the median of off-frames over a 100 frame window removed the accurate background. Single-molecule intensities were measured as the sum of pixel intensities over a 735 nm (15 pixel) side length square region around each molecule.

Recorded single-molecules were grouped into the set of coupled (on-GNR) molecules for each GNR, and the set of uncoupled (off-GNR) molecules for the entire movie. The on-GNR region was defined as the region within a 100 nm radius of the super-resolved GNR location (whic reports the center of the GNR) and the off-GNR region was defined as every position further than 490 nm from the GNR location. Each GNR position is therefore a crucial piece of information. To locate the GNR position, I fit the GNR intrinsic PL to the microscope PSF to super-resolve its location. However, the GNR PL vanishes (for a 640 nm laser) when the excitation polarization is polarized perpendicular to the GNR longitudinal axis. To overcome this problem, I developed a pattern-matching algortihm using tracked locations of the GNRs in each movie. Briefly, the time median of each movie was calculated to emphasize the image of the GNRs and minimize the images of molecules in the movie. These images were then put together as the frames for a movie, which was fit with the SMALL-LABS software (without doing background subtraction) and the GNR fits were tracked using a single-particle tracking algorithm [194] based on the Hungarian method [195]. The GNR tracks were made to match the pattern the three GNRs were positioned in. Using this approach, I measured the super-resolved position of each GNR in each movie, including in movies where the GNR PL was faint or nonexistent.

The single-molecule intensity enhancement was calculated by first calculating the median of the off-GNR set, and then normalizing the on-GNR set for that movie to this value. The set of measured molecules from all movies taken at the same polarization angle were collapsed to give one enhancement distribution for each GNR for polarization angle. The datasets for each GNR were then shifted to a relative polarization angle coordinate system, so that each GNR longitudinal axis was oriented at 90° in the collapsed set.

7.4 Results

Before analyzing the experimental results, we should first bring in the final predicted results. The calculations in Sec. 4.4 were carried out for excitation polarization angles from 0° to 90° in 5° steps, these results were mapped to 90° to 180° by reflection. To match the experimental detection lower bounds, molecules predicted to have an enhancement less than 0.5 (molecules whose brightness is less than half the off-GNR median brightness) were excluded from the distribution. The distributions for all excitation polarization angles are shown in Fig. 7.5

The measured enhancement distributions are shown in Fig. 7.6. The distribution in

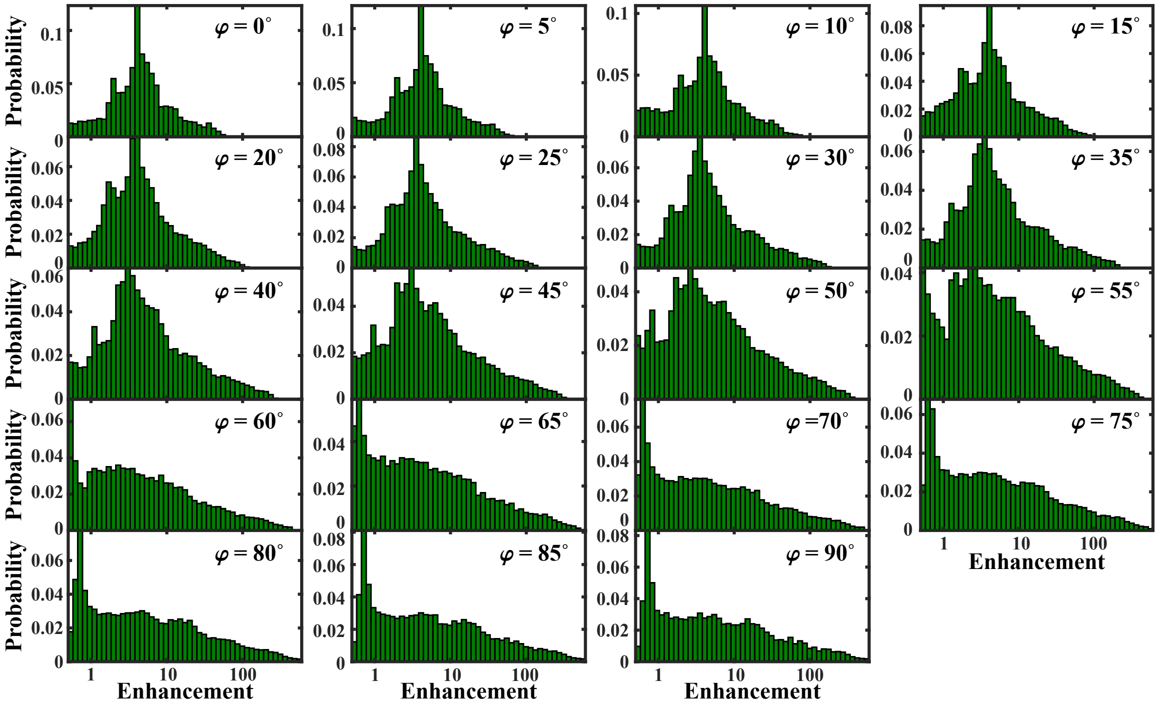

Figure 7.5: Predicted enhancement distributions. The excitation polarization angle, φ, is indicated for each distribution.

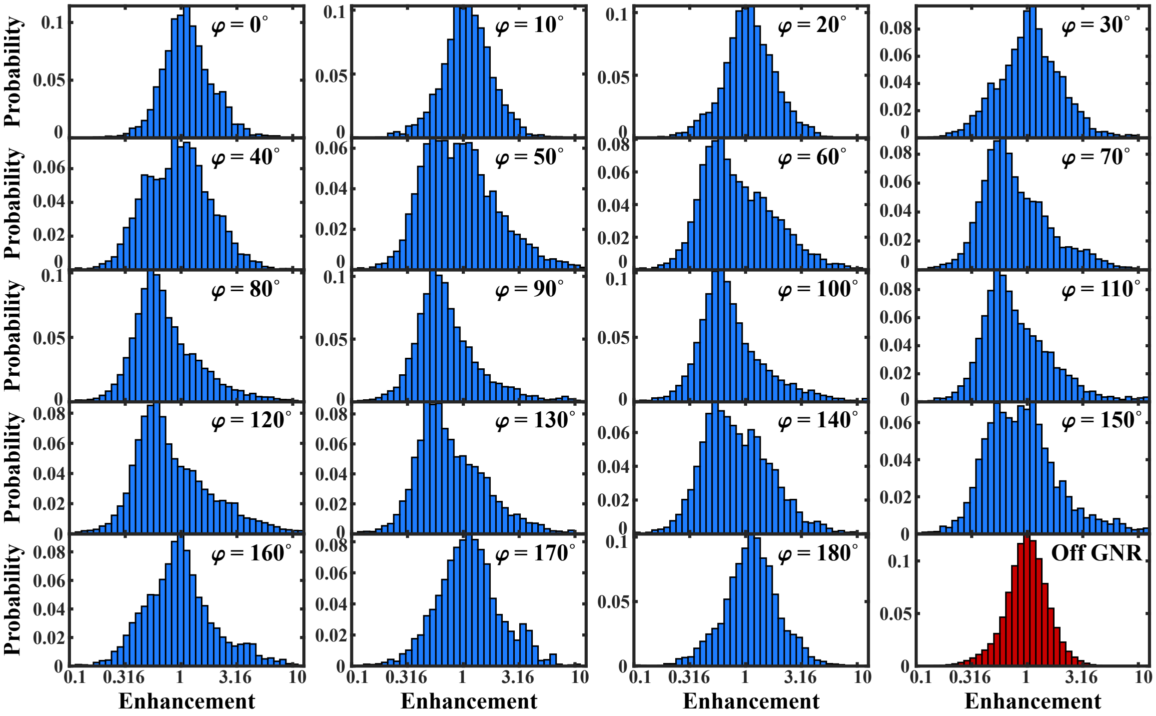

Figure 7.6: Enhancement distributions. The excitation polarization angle, φ, is indicated for each distribution. A representative off-GNR distribution (scaled to its own median) is shown in red.

red shows a representative off-GNR distribution, showing that in the absence of an optical antenna, single molecule brightnesses are well characterized as a log-normal distribution [200]. The off-GNR distribution also shows a tightly grouped brightness distribution, relative to the on-GNR distributions. The significant deviations in the on-GNR distributions from the off-GNR distribution arise from coupling to GNR.

The measured distributions shown in Fig. 7.6 always contain a large portion of unenhanced molecules matching the off-GNR distribution. The predicted distributions also contain a large portion of unenhanced molecules (a peak at enhancement of 1), but this population appears to be a smaller portion of the overall distribution than in the measured distributions.

In addition to this large portion of unenhanced molecules, the measured and predicted distributions show quenched and enhanced populations, which appear in variable amounts depending on the excitation polarization angle. In both the measured and the predicted distributions, this quenched population produces a second peak in the histograms whose location and magnitude increases to a maximum as the excitation polarization nears 90°. This is a very surprising result, that there are more quenched molecules than enhanced molecules when the polarization is parallel to the longitudinal axis.

To more quantitatively analyze the measured and predicted trends of the distributions shown in Fig. 7.6 and Fig. 7.5, we look at statistical measurements of each distribution. Fig. 7.7 shows several measurements of the trends in both the experimentally measured and theoretically predicted distributions.

In Fig. 7.7a and d, the mean enhancement for each polarization angle is shown. The measured mean enhancement shows a small change ($\sim 25\%$) the minimum mean enhancement occurs for $\varphi \approx 90^\circ$, parallel to the LM. The predicted enhancement mean shows a larger change ($\sim 125\%$), and with the opposite trend: that the mean enhancement is maximal when the excitation laser is polarized perpendicular to the longitudinal axis. The theoretical results matches a previous study on bulk fluorescence coupled to a single

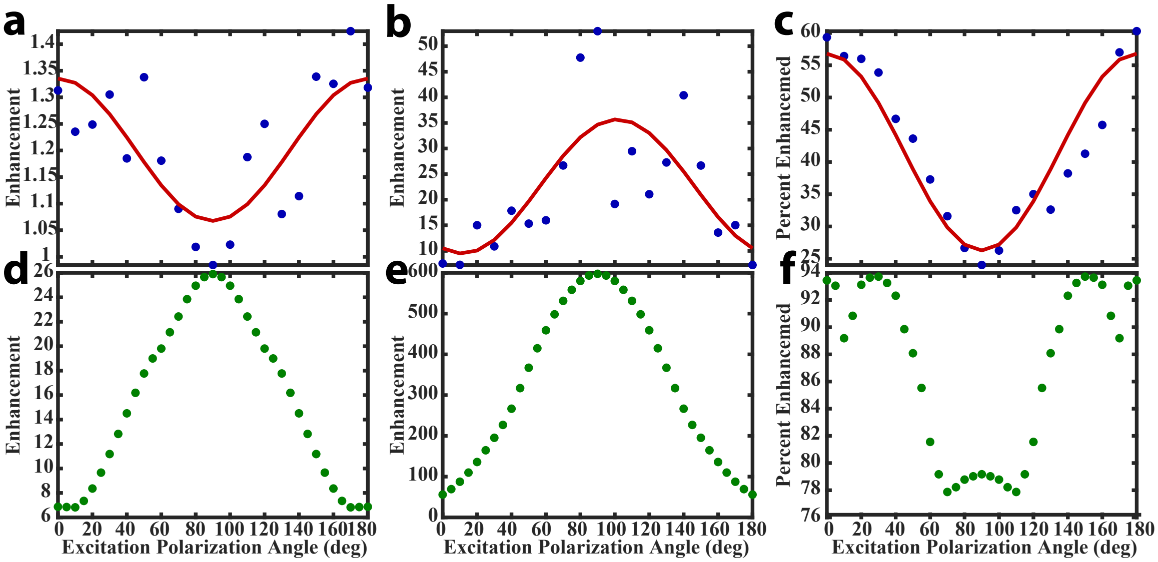

Figure 7.7: Enhancement trends as function of polarization. a – c: experimental results in blue and fit result to Eq. 7.1 in red. d – f: theoretical predictions. a and d: mean enhancement. b and e: maximum enhancement. c and f: percentage of molecules enhanced (enhancement > 1).

GNR [222].

This surprising result can be understood in the context of Fig. 4.8, which shows the predicted map of enhancements around a GNR. The highest enhancements occur in a very small region near the surface of the GNR. The experiments appear to have undercounted these extremely highly enhanced molecules relative to the simulations. This could be because there simply were not enough measured molecules to statistically sample this very small region. It could also be something in the experiments precluded molecules from adsorbing on the surface very near to the GNR. One possibility is that the GNR was coated in something other than a single CTAB bilayer, as was our assumption in the simulations, preventing any molecules from adsorbing very close to the GNR surface.

With this limitation in mind, we can still compare other aspects of the measured and predicted distributions. Even if the very highest enhancements were not statistically, or even at all, measured, the highest measured enhancement values should still arise when the polarization is parallel to the GNR longitudinal axis. Fig. 7.7b and e show the measured and predicted maximum enhancement, respectively. The theory now matches the experiment, with the maximum maximum enhancement occurring for $\varphi \approx 90^\circ$. This finding supports our hypothesis that the excitation enhancement is the dominant source of enhancement in this system, and as the laser is resonant with LM, we see maximal enhancement for the excitation polarization polarized parallel to the GNR longitudinal axis. Also consistent with the experiments missing the very highest enhancements, the measured values of maximum enhancement are far smaller than the predicted values.

Because of the spatial distribution of enhancement and quenching, in Fig. 4.8, it is instructive to look at how many molecules are enhanced versus quenched. Fig. 7.7c and f show the percentage of molecules enhanced (enhancement > 1). The remaining molecules are quenched (enhancement ≤ 1). Overall we determine that a higher percentage of molecules are enhanced when the excitation is polarized along the GNR transverse axis. This trend is consistent with the enhancement maps, which show that the highest enhancements come from a very small region of highly enhanced fields. The quenching has two causes: firstly, the field reshaping causes the field in large areas around the GNR to actually be smaller than its unperturbed value. Secondly, GNRs are very lossy antennas, and especially in this case where the Cy5.5 emission is not resonant with the LSPR, the dye molecules will experience a small emission enhancement at best, and possibly a large quenching of their emission. If the excitation enhancement is insufficient to balance this effect, the net effect is quenching. Because the fields are more tightly confined when the excitation polarization is polarized parallel to the GNR longitudinal axis, this effect is more pronounced at 0°, leading most molecules to be quenched when the laser is polarized parallel to the longitudinal axis.

Overall, these single-molecule experiments uncover the richness of the physics underlying fluorescence modification by a plasmonic optical antenna. These results show that excitation polarization can be used to change the brightness of an emitter, and that the nature of this modification depends on a multiple of factors. These experiments also show the utility of the theoretical framework I laid out in Chap. IV, which was essential for understanding these experimental results.

CHAPTER VIII

Conclusions and Future Directions

I began this thesis on the theory, methodology, and measurement of modifying single-molecule fluorescence with a plasmonic optical antenna, by introducing single-molecule fluorescence super-resolution microscopy in Chap. II, and then introducing plasmonics and optical antennas in Chap. III.

In Chap. IV, I presented a new theoretical approach to understand the interaction of a single fluorescent molecule with an optical antenna. The potential future applications of this theory go beyond the examples in this dissertation. For example, this theoretical work was partially motivated by preliminary experiments in our lab by Esther Wertz, who measured how coupling single fluorescent molecules to plasmonic optical antennas modifies their spectra. Indeed, the theoretical framework does predict this surprising result; for example, Fig. 4.6 shows predictions of how the emission spectrum of Cy5.5 molecules change upon coupling to a GNR. Ongoing work by my labmate Stephen Lee has furthered these experiments. Fig. 8.1 shows results from the hyperspectral dual single-molecule imaging and spectroscopy setup that Stephen developed. When these experiments conclude, we will compare his experimental results with theoretical predictions using the framework laid out in Chap. IV.

In Chap. V, I presented the SMALL-LABS algorithm, which I invented to locate and measure single molecules, even in the presence of obscuring backgrounds. To imple-

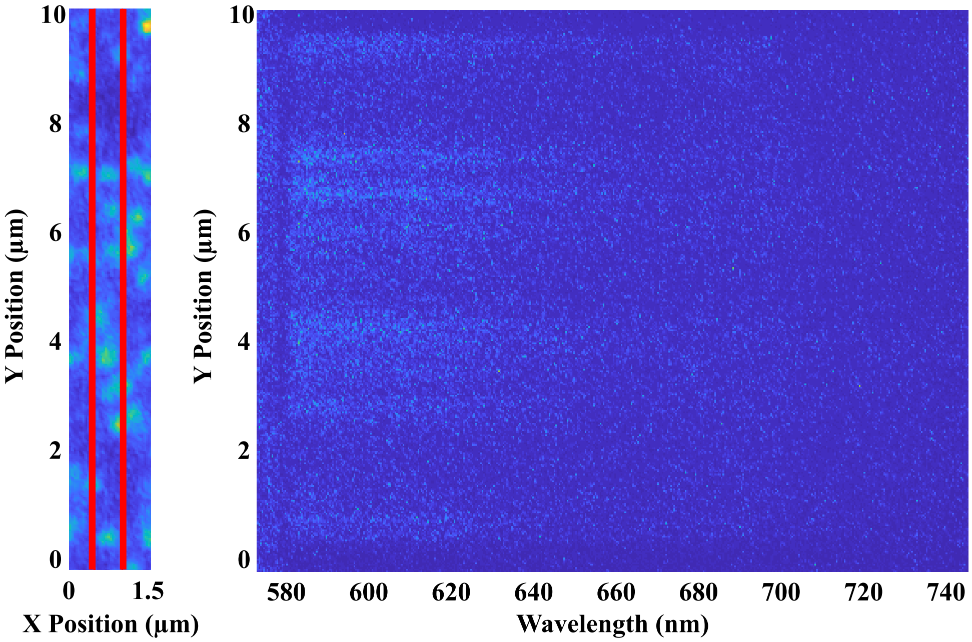

Figure 8.1: Hyperspectral dual single-molecule imaging and spectroscopy. Left: Single molecule imaging; red lines indicate the region spectra are recorded from. Right: corresponding single-molecule spectra. Figure courtesy of Stephen Lee.

ment the SMALL-LABS algorithm, we developed open-source Matlab software, available at https://github.com/BiteenMatlab/SMALL-LABS. The SMALL-LABS code is written as highly modular software for the express purpose of being easily adapted and expanded. I am hopeful that other researchers will find the SMALL-LABS code useful for single-molecule analysis (even if not using background subtraction) and possibly expand it. One easy expansion is to implement a GUI, which will make adoption easier for new users. Another obvious extension is to use machine learning algorithms to help with some tasks. For example, molecule detection (guessing) and false-positive filtering should be straightforward problems for machine learning approaches to tackle, for example implementing, or extending, similar recent developments [223–225].

In Chap VI, I explained the origin of the mislocalization effect and detailed our investigations of the effect, focusing on my theoretical predictions and computational approaches to mislocalization, published in [35–37]. The mislocalization effect presents a fundamental barrier to using optical antennas to enhance the resolution of single-molecule super-resolution microscopy. Given the immense impact that super-resolution microscopy has already had, if the resolution can be further improved, the impact would be tremendous. Therefore, finding a means of overcoming or avoiding mislocalization is a critical area of ongoing research, and our work on this subject has spurred a huge amount of interest and follow-up, see for example [201, 206, 226–232]. One framing of this problem is as an attempt to solve the inverse problem that mislocalization presents, therefore using insights from other fields which have grappled with inverse problems [233–235] may be a promising approach.

In Chap. VII, I detailed my experimental and theoretical investigations of the excitation polarization dependence of fluorescence enhancement for single molecules coupled to a GNR plasmonic optical antenna. This experiment could be easily extended to study the effect of circularly polarized light on the modification of single-molecule fluorescence by chiral optical antennas [236–242], which would be an interesting study.

I have been collaborating with my labmate Tiancheng (Curly) Zuo to study the complementary problem to the excitation-side research in Chap. VII; Curly has been investigating how coupling to a GNR modifies the emission polarization of single-molecule fluorescence. Curly's results, shown in Fig. 8.2, show a clear modification effect by the GNR on the coupled single-molecule emission polarization. These results may be a useful part of solving the emission mislocalization inverse problem.

In these experiments on GNR-modified emission polarization, we separated the emitted polarization into its S and P polarization components by using a birefringent crystal to separate the image of one molecule into two. This same principle can be extended to an arbitrary separation of polarization component images by using a metasurface [243–251] instead of a birefringent crystal. The advantage of the metasurface is that it can allow all polarization information to be measured, not just intensity in the S and P channels, and therefore using a single metasurface achieves full single-molecule polarimetry in an imaging experiment. Furthermore, given the customization a metasurface affords, it would

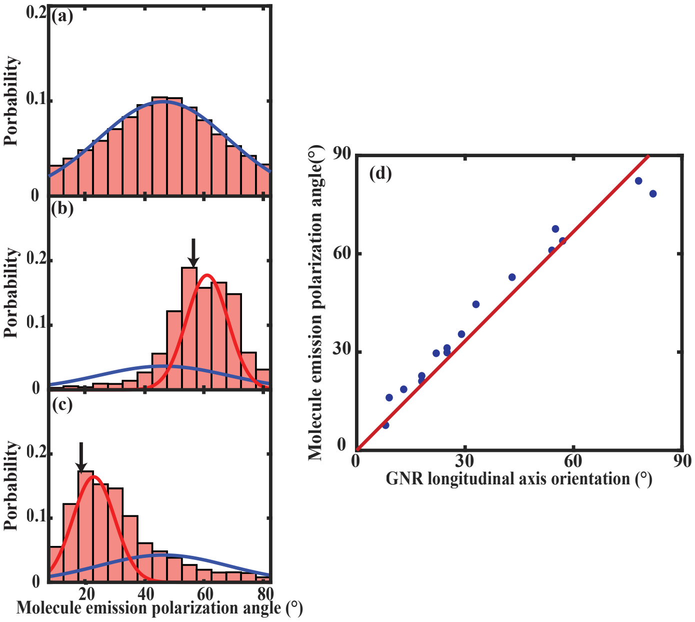

Figure 8.2: Molecule emission polarization of GNR coupled fluorescence. Emission polarization distributions for (a) off-GNR, (b,c) Example on-GNR. The black arrow in (b,c) indicates the GNR long-axis orientation. The blue curves in (a) – (c) are a fit to background, and the red curves in (b,c) are fit to the modified molecules. (d) Data and linear fit of all distributions. Figure courtesy of Tiancheng Zuo.

allow experimentalists fine control and customization over the polarization separation—allowing optimization of any experimental setup.

Finally, in Chap. VII, I discussed RoboScope, the microscope automation platform I developed. Open-source code for RoboScope is available at https://github.com/bpisaacoff/-RoboScope. Like the code for SMALL-LABS, RoboScope is also written as modular code, in the hope that other researchers will adapt and expand it for additional experiments. My experiments in Chap. VII were only feasible to perform by using RoboScope, and I expect that a number of new experiments which were previously infeasible, can now be attempted using RoboScope.

By bringing together single-molecule fluorescence super-resolution microscopy and plasmonics, this dissertation supports two synergistic directions for applications: enhancing the resolution of single-molecule fluorescence super-resolution imaging and using a novel technique to directly study how a single emitter interacts with an optical antenna. This work advances the fundamental science of nanophotonics and will pave the way for next-generation super-resolution imaging and optical antenna technologies.

BIBLIOGRAPHY

BIBLIOGRAPHY

[1] B. Huang, M. Bates, X. Zhuang, “Super-Resolution Fluorescence Microscopy”, *Annual Review of Biochemistry* **78**, 993 (2009). DOI: 10.1146/annurev.biochem.77.061906.092014.

[2] M. A. Thompson, M. D. Lew, W. Moerner, “Extending Microscopic Resolution with Single-Molecule Imaging and Active Control”, *Annual Review of Biophysics* **41**, 321 (2012). DOI: 10.1146/annurev-biophys-050511-102250.

[3] C. Joo, H. Balci, Y. Ishitsuka, C. Buranachai, T. Ha, “Advances in Single-Molecule Fluorescence Methods for Molecular Biology”, *Annual Review of Biochemistry* **77**, 51 (2008). DOI: 10.1146/annurev.biochem.77.070606.101543.

[4] Nobelprize.org, “The Nobel Prize in Chemistry 2014 - Press Release” (2014), (Accessed: 2014-11-12).

[5] J. Yu, “Single-Molecule Studies in Live Cells”, *Annual Review of Physical Chemistry* **67**, 565 (2016). DOI: 10.1146/annurev-physchem-040215-112451.

[6] H. H. Tuson, J. S. Biteen, “Unveiling the inner workings of live bacteria using super-resolution microscopy”, *Analytical Chemistry* **87**, 42 (2015). DOI: 10.1021/ac5041346.

[7] J. Biteen, K. A. Willets, “Introduction: Super-Resolution and Single-Molecule Imaging”, *Chemical Reviews* **117**, 7241 (2017). DOI: 10.1021/acs.chemrev.7b00242.

[8] K. A. Willets, A. J. Wilson, V. Sundaresan, P. B. Joshi, “Super-Resolution Imaging and Plasmonics”, *Chemical Reviews* **117**, 7538 (2017). DOI: 10.1021/acs.chemrev.6b00547.

[9] A. B. Zrimsek, *et al.*, “Single-Molecule Chemistry with Surface- and Tip-Enhanced Raman Spectroscopy”, *Chemical Reviews* **117**, 7583 (2017). DOI: 10.1021/acs.chemrev.6b00552.

[10] S. Habuchi, “Super-Resolution Molecular and Functional Imaging of Nanoscale Architectures in Life and Materials Science”, *Frontiers in Bioengineering and Biotechnology* **2** (2014). DOI: 10.3389/fbioe.2014.00020.

[11] D. Wöll, C. Flors, “Super-resolution Fluorescence Imaging for Materials Science”, *Small Methods* **1**, 1700191 (2017). DOI: 10.1002/smtd.201700191.

[12] T. Chen, *et al.*, “Optical Super-Resolution Imaging of Surface Reactions”, *Chemical Reviews* **117**, 7510 (2017). DOI: 10.1021/acs.chemrev.6b00673.

[13] Y. Kazoe, K. Mawatari, Y. Sugii, T. Kitamori, “Development of a Measurement Technique for Ion Distribution in an Extended Nanochannel by Super-Resolution-Laser-Induced Fluorescence”, *Analytical Chemistry* **83**, 8152 (2011). DOI: 10.1021/ac201654r.

[14] C. E. ONeil, J. M. Jackson, S.-H. Shim, S. A. Soper, “Interrogating Surface Functional Group Heterogeneity of Activated Thermoplastics Using Super-Resolution Fluorescence Microscopy”, *Analytical Chemistry* **88**, 3686 (2016). DOI: 10.1021/acs.analchem.5b04472.

[15] J. N. Anker, *et al.*, “Biosensing with plasmonic nanosensors”, *Nature Materials* **7**, 442 (2008). DOI: 10.1038/nmat2162.

[16] P. Bharadwaj, B. Deutsch, L. Novotny, “Optical Antennas”, *Advances in Optics and Photonics* **1**, 438 (2009). DOI: 10.1364/AOP.1.000438.

[17] L. Novotny, N. Van Hulst, “Antennas for light”, *Nature Photonics* **5**, 83 (2011). DOI: 10.1038/nphoton.2010.237.

[18] M. Agio, “Optical antennas as nanoscale resonators”, *Nanoscale* **4**, 692 (2012). DOI: 10.1039/C1NR11116G.

[19] J. Alda, J. M. Rico-García, J. M. López-Alonso, G. Boreman, “Optical antennas for nano-photonic applications”, *Nanotechnology* **16**, S230 (2005). DOI: 10.1088/0957-4484/16/5/017.

[20] M. I. Stockman, “Nanoplasmonics: past, present, and glimpse into future”, *Optics Express* **19**, 22029 (2011). DOI: 10.1364/OE.19.022029.

[21] X. Fan, W. Zheng, D. J. Singh, “Light scattering and surface plasmons on small spherical particles”, *Light: Science & Applications* **3**, e179 (2014). DOI: 10.1038/lsa.2014.60.

[22] M. Pelton, J. Aizpurua, G. Bryant, “Metal-nanoparticle plasmonics”, *Laser and Photonics Reviews* **2**, 136 (2008). DOI: 10.1002/lpor.200810003.

[23] J. A. Schuller, *et al.*, “Plasmonics for extreme light concentration and manipulation”, *Nature Materials* **9**, 193 (2010). DOI: 10.1038/nmat2630.

[24] A. F. Koenderink, A. Alù, A. Polman, “Nanophotonics: Shrinking light-based technology”, *Science* **348**, 516 (2015). DOI: 10.1126/science.1261243.

[25] D. K. Gramotnev, S. I. Bozhevolnyi, “Plasmonics beyond the diffraction limit”, *Nature Photonics* **4**, 83 (2010). DOI: 10.1038/nphoton.2009.282.

[26] K. A. Willets, R. P. Van Duyne, “Localized Surface Plasmon Resonance Spectroscopy and Sensing”, *Annual Review of Physical Chemistry* **58**, 267 (2007). DOI: 10.1146/annurev.physchem.58.032806.104607.

[27] C. L. Haynes, A. D. McFarland, R. P. V. Duyne, “Surface-Enhanced Raman Spectroscopy”, *Analytical Chemistry* **77**, 338 A (2005). DOI: 10.1021/ac053456d.

[28] J. R. Cole, N. A. Mirin, M. W. Knight, G. P. Goodrich, N. J. Halas, “Photothermal efficiencies of nanoshells and nanorods for clinical therapeutic applications”, *Journal of Physical Chemistry C* **113**, 12090 (2009). DOI: 10.1021/jp9003592.

[29] M. F. Tsai, *et al.*, “Au nanorod design as light-absorber in the first and second biological near-infrared windows for in vivo photothermal therapy”, *ACS Nano* **7**, 5330 (2013). DOI: 10.1021/nn401187c.

[30] J. M. Stern, J. Stanfield, W. Kabbani, J. T. Hsieh, J. A. Cadeddu, “Selective prostate cancer thermal ablation with laser activated gold nanoshells”, *Journal of Urology* **179**, 748 (2008). DOI: 10.1016/j.juro.2007.09.018.

[31] M. S. Tame, *et al.*, “Quantum plasmonics”, *Nature Physics* **9**, 329 (2013). DOI: 10.1038/nphys2615.

[32] A. Ridolfo, O. Di Stefano, N. Fina, R. Saija, S. Savasta, “Quantum Plasmonics with Quantum Dot-Metal Nanoparticle Molecules: Influence of the Fano Effect on Photon Statistics”, *Physical Review Letters* **105**, 263601 (2010). DOI: 10.1103/PhysRevLett.105.263601.

[33] T. B. Hoang, G. M. Akselrod, M. H. Mikkelsen, “Ultrafast Room-Temperature Single Photon Emission from Quantum Dots Coupled to Plasmonic Nanocavities”, *Nano Letters* **16**, 270 (2016). DOI: 10.1021/acs.nanolett.5b03724.

[34] M. Ringler, *et al.*, “Shaping emission spectra of fluorescent molecules with single plasmonic nanoresonators”, *Physical Review Letters* **100**, 203002 (2008). DOI: 10.1103/PhysRevLett.100.203002.

[35] E. Wertz, B. P. Isaacoff, J. D. Flynn, J. S. Biteen, “Single-Molecule Super-Resolution Microscopy Reveals How Light Couples to a Plasmonic Nanoantenna on the Nanometer Scale”, *Nano Letters* **15**, 2662 (2015). DOI: 10.1021/acs.nanolett.5b00319.

[36] E. A. Wertz, B. P. Isaacoff, J. S. Biteen, “Wavelength-Dependent Super-resolution Images of Dye Molecules Coupled to Plasmonic Nanotriangles”, *ACS Photonics* **3**, 1733 (2016). DOI: 10.1021/acsphotonics.6b00344.

[37] B. Fu, B. P. Isaacoff, J. S. Biteen, “Super-Resolving the Actual Position of Single Fluorescent Molecules Coupled to a Plasmonic Nanoantenna”, *ACS Nano* **11**, 8978 (2017). DOI: 10.1021/acsnano.7b03420.

[38] M. Abramowitz, M. W. Davidson, “Olympus BH2 Research Microscope Cutaway Diagram”, https://www.olympus-lifescience.com/en/microscope-resource/primer/anatomy/bh2cutaway/ (2012), (Accessed: 2018-02-18).

[39] W. Fester, M. Abramowitz, M. Davidson, “Olympus IX70 Fluorescence Microscope Cutaway Diagram”, https://www.olympus-lifescience.com/en/microscope-resource/primer/techniques/fluorescence/ix70fluorescence/ (2012), (Accessed: 2018-02-18).

[40] L. Novotny, B. Hecht, *Principles of nano-optics*, vol. 9781107005 (Cambridge University Press, 2009).

[41] E. Abbe, “Beiträge zur Theorie des Mikroskops und der mikroskopischen Wahrnehmung”, *Archiv für Mikroskopische Anatomie* **9**, 413 (1873). DOI: 10.1007/BF02956173.

[42] H. Lipson, S.G. and Lipson, D. S. Tannhauser, *Optical Physics* (Cambridge University Press, 1995), fourth edn.

[43] M. W. D. Joel S. Silfies, Stanley A. Schwartz, “The Diffraction Barrier in Optical Microscopy” (2013).

[44] E. Hecht, *Optics* (Adison-Wesley, 2002), fourth edn.

[45] A. V. Helden, S. Dupré, R. van Gent, H. Zuidervaart, *The origins of the telescope* (KNAW Press, 2010).

[46] F. M. Ross, “Opportunities and challenges in liquid cell electron microscopy”, *Science* **350**, aaa9886 (2015). DOI: 10.1126/science.aaa9886.

[47] N. De Jonge, D. B. Peckys, “Live Cell Electron Microscopy Is Probably Impossible”, *ACS Nano* **10**, 9061 (2016). DOI: 10.1021/acsnano.6b02809.

[48] M. Wojcik, M. Hauser, W. Li, S. Moon, K. Xu, “Graphene-enabled electron microscopy and correlated super-resolution microscopy of wet cells”, *Nature Communications* **6**, 7384 (2015). DOI: 10.1038/ncomms8384.

[49] M. S. Joens, *et al.*, “Helium Ion Microscopy (HIM) for the imaging of biological samples at sub-nanometer resolution”, *Scientific Reports* **3**, 3514 (2013). DOI: 10.1038/srep03514.

[50] T. Ando, T. Uchihashi, N. Kodera, “High-Speed AFM and Applications to Biomolecular Systems”, *Annual Review of Biophysics* **42**, 393 (2013). DOI: 10.1146/annurev-biophys-083012-130324.

[51] J. R. Lakowicz, *Principles of Fluorescence Spectroscopy Principles of Fluorescence Spectroscopy* (Springer, 2006), third edn.

[52] M. Orrit, “Chemical and physical aspects of charge transfer in the fluorescence intermittency of single molecules and quantum dots”, *Photochemical & Photobiological Sciences* **9**, 637 (2010). DOI: 10.1039/b9pp00192a.

[53] C. Jing, V. W. Cornish, “Chemical tags for labeling proteins inside living cells”, *Accounts of Chemical Research* **44**, 784 (2011). DOI: 10.1021/ar200099f.

[54] W. E. Moerner, L. Kador, "Optical detection and spectroscopy of single molecules in a solid", *Physical Review Letters* **62**, 2535 (1989). DOI: 10.1103/PhysRevLett.62.2535.

[55] M. Orrit, J. Bernard, "Single pentacene molecules detected by fluorescence excitation in a p -terphenyl crystal", *Physical Review Letters* **65**, 2716 (1990). DOI: 10.1103/PhysRevLett.65.2716.

[56] W. E. Moerner, M. Orrit, "Illuminating single molecules in condensed matter", *Science* **283**, 1670 (1999). DOI: 10.1126/science.283.5408.1670.

[57] F. Güttler, T. Irngartinger, T. Plakhotnik, A. Renn, U. P. Wild, "Fluorescence microscopy of single molecules", *Chemical Physics Letters* **217**, 393 (1994). DOI: 10.1016/0009-2614(94)87003-9.

[58] T. Schmidt, G. J. Schütz, W. Baumgartner, H. J. Gruber, H. Schindler, "Imaging of single molecule diffusion.", *Proceedings of the National Academy of Sciences of the United States of America* **93**, 2926 (1996).

[59] T. Ha, T. A. Laurence, D. S. Chemla, S. Weiss, "Polarization Spectroscopy of Single Fluorescent Molecules", *The Journal of Physical Chemistry B* **103**, 6839 (1999). DOI: 10.1021/jp990948j.

[60] W. E. Moerner, D. P. Fromm, "Methods of single-molecule fluorescence spectroscopy and microscopy", *Review of Scientific Instruments* **74**, 3597 (2003). DOI: 10.1063/1.1589587.

[61] A. Sharonov, R. M. Hochstrasser, "Wide-field subdiffraction imaging by accumulated binding of diffusing probes", *Proceedings of the National Academy of Sciences* **103**, 18911 (2006). DOI: 10.1073/pnas.0609643104.

[62] E. Betzig, *et al.*, "Imaging intracellular fluorescent proteins at nanometer resolution", *Science* **313**, 1642 (2006). DOI: 10.1126/science.1127344.

[63] S. T. Hess, T. P. Girirajan, M. D. Mason, "Ultra-high resolution imaging by fluorescence photoactivation localization microscopy", *Biophysical Journal* **91**, 4258 (2006). DOI: 10.1529/biophysj.106.091116.

[64] M. J. Rust, M. Bates, X. Zhuang, "Sub-diffraction-limit imaging by stochastic optical reconstruction microscopy (STORM)", *Nature Methods* **3**, 793 (2006). DOI: 10.1038/nmeth929.

[65] R. E. Thompson, D. R. Larson, W. W. Webb, "Precise nanometer localization analysis for individual fluorescent probes", *Biophysical Journal* **82**, 2775 (2002). DOI: 10.1016/S0006-3495(02)75618-X.

[66] A. Yildiz, *et al.*, "Myosin V walks hand-over-hand: Single fluorophore imaging with 1.5-nm localization", *Science* **300**, 2061 (2003). DOI: 10.1126/science.1084398.

[67] A. Small, S. Stahlheber, "Fluorophore localization algorithms for super-resolution microscopy", *Nature Methods* **11**, 267 (2014). DOI: 10.1038/nmeth.2844.

[68] D. Sage, *et al.*, "Quantitative evaluation of software packages for single-molecule localization microscopy", *Nature Methods* **12**, 717 (2015). DOI: 10.1038/nmeth.3442.

[69] A. Lee, K. Tsekouras, C. Calderon, C. Bustamante, S. Pressé, "Unraveling the Thousand Word Picture: An Introduction to Super-Resolution Data Analysis", *Chemical Reviews* **117**, 7276 (2017). DOI: 10.1021/acs.chemrev.6b00729.

[70] B. Hebert, S. Costantino, P. W. Wiseman, "Spatiotemporal image correlation spectroscopy (STICS) theory, verification, and application to protein velocity mapping in living CHO cells", *Biophysical Journal* **88**, 3601 (2005). DOI: 10.1529/biophysj.104.054874.

[71] D. J. Rowland, H. H. Tuson, J. S. Biteen, "Resolving Fast, Confined Diffusion in Bacteria with Image Correlation Spectroscopy", *Biophysical Journal* **110**, 2241 (2016). DOI: 10.1016/j.bpj.2016.04.023.

[72] H. Shen, *et al.*, "Single Particle Tracking: From Theory to Biophysical Applications", *Chemical Reviews* **117**, 7331 (2017). DOI: 10.1021/acs.chemrev.6b00815.

[73] S. W. Hell, J. Wichmann, "Breaking the diffraction resolution limit by stimulated emission: stimulated-emission-depletion fluorescence microscopy", *Optics Letters* **19**, 780 (1994). DOI: 10.1364/OL.19.000780.

[74] H. Blom, J. Widengren, "Stimulated Emission Depletion Microscopy", *Chemical Reviews* **117**, 7377 (2017). DOI: 10.1021/acs.chemrev.6b00653.

[75] E. Betzig, A. Lewis, A. Harootunian, M. Isaacson, E. Kratschmer, "Near Field Scanning Optical Microscopy (NSOM): Development and Biophysical Applications", *Biophysical Journal* **49**, 269 (1986). DOI: 10.1016/S0006-3495(86)83640-2.

[76] R. C. Dunn, "Near-Field Scanning Optical Microscopy", *Chemical Reviews* **99**, 2891 (1999). DOI: 10.1021/cr980130e.

[77] D. A. Bonnell, *et al.*, "Imaging physical phenomena with local probes: From electrons to photons", *Reviews of Modern Physics* **84**, 1343 (2012). DOI: 10.1103/RevModPhys.84.1343.

[78] N. Rotenberg, L. Kuipers, "Mapping nanoscale light fields", *Nature Photonics* **8**, 919 (2014). DOI: 10.1038/nphoton.2014.285.

[79] T. Dertinger, R. Colyer, G. Iyer, S. Weiss, J. Enderlein, "Fast, background-free, 3D super-resolution optical fluctuation imaging (SOFI)", *Proceedings of the National Academy of Sciences* **106**, 22287 (2009). DOI: 10.1073/pnas.0907866106.

[80] E. Aslan, *et al.*, "Multispectral Cesaro-Type Fractal Plasmonic Nanoantennas", *ACS Photonics* **3**, 2102 (2016). DOI: 10.1021/acsphotonics.6b00540.

[81] S. Gottheim, H. Zhang, A. O. Govorov, N. J. Halas, "Fractal nanoparticle plasmonics: The cayley tree", *ACS Nano* **9**, 3284 (2015). DOI: 10.1021/acsnano.5b00412.

[82] S. A. Maier, *Plasmonics: Fundamentals and applications* (Springer US, Boston, MA, 2007).

[83] M. Fox, *Optical Properties of Solids* (Oxford University Press, 2010), second edn.

[84] P. B. Johnson, R. W. Christy, "Optical constants of the noble metals", *Physical Review B* **6**, 4370 (1972). DOI: 10.1103/PhysRevB.6.4370.

[85] B. Ung, Y. Sheng, "Interference of surface waves in a metallic nanoslit", *Optics Express* **15**, 1182 (2007). DOI: 10.1364/OE.15.001182.

[86] A. D. Rakić, A. B. Djurišić, J. M. Elazar, M. L. Majewski, "Optical properties of metallic films for vertical-cavity optoelectronic devices", *Applied Optics* **37**, 5271 (1998). DOI: 10.1364/AO.37.005271.

[87] S. Lal, S. Link, N. J. Halas, "Nano-optics from sensing to waveguiding", *Nature Photonics* **1**, 641 (2007). DOI: 10.1038/nphoton.2007.223.

[88] S. Khatua, M. Orrit, "Probing, sensing, and fluorescence enhancement with single gold nanorods", *Journal of Physical Chemistry Letters* **5**, 3000 (2014). DOI: 10.1021/jz501253j.

[89] K. M. Mayer, J. H. Hafner, "Localized surface plasmon resonance sensors", *Chemical Reviews* **111**, 3828 (2011). DOI: 10.1021/cr100313v.

[90] A. B. Taylor, P. Zijlstra, "Single-Molecule Plasmon Sensing: Current Status and Future Prospects", *ACS Sensors* **2**, 1103 (2017). DOI: 10.1021/acssensors.7b00382.

[91] J. D. Jackson, *Classical Electrodynamics* (Wiley, 1999), third edn.

[92] C. F. Bohren, D. R. Huffman, *Absorption and Scattering of Light by Small Particles* (Wiley-VCH Verlag GmbH, Weinheim, Germany, 1998).

[93] S. A. Maier, H. A. Atwater, "Plasmonics: Localization and guiding of electromagnetic energy in metal/dielectric structures", *Journal of Applied Physics* **98**, 011101 (2005). DOI: 10.1063/1.1951057.

[94] M. A. van Dijk, *et al.*, "Absorption and scattering microscopy of single metal nanoparticles", *Physical Chemistry Chemical Physics* **8**, 3486 (2006). DOI: 10.1039/b606090k.

[95] L. Slaughter, W. S. Chang, S. Link, "Characterizing plasmons in nanoparticles and their assemblies with single particle spectroscopy", *Journal of Physical Chemistry Letters* **2**, 2015 (2011). DOI: 10.1021/jz200702m.

[96] J. Olson, *et al.*, "Optical characterization of single plasmonic nanoparticles", *Chemical Society Reviews* **44**, 40 (2015). DOI: 10.1039/C4CS00131A.

[97] P. K. Jain, K. S. Lee, I. H. El-Sayed, M. A. El-Sayed, "Calculated absorption and scattering properties of gold nanoparticles of different size, shape, and composition: Applications in biological imaging and biomedicine", *Journal of Physical Chemistry B* **110**, 7238 (2006). DOI: 10.1021/jp057170o.

[98] S. Link, M. A. El-Sayed, "Shape and size dependence of radiative, non-radiative and photothermal properties of gold nanocrystals", *International Reviews in Physical Chemistry* **19**, 409 (2000). DOI: 10.1080/01442350050034180.

[99] K. L. Kelly, E. Coronado, L. L. Zhao, G. C. Schatz, "The Optical Properties of Metal Nanoparticles: The Influence of Size, Shape, and Dielectric Environment", *The Journal of Physical Chemistry B* **107**, 668 (2003). DOI: 10.1021/jp026731y.

[100] T. K. Sau, A. L. Rogach, eds., *Complex-Shaped Metal Nanoparticles* (Wiley-VCH Verlag GmbH & Co. KGaA, Weinheim, Germany, 2012).

[101] C. L. Nehl, J. H. Hafner, "Shape-dependent plasmon resonances of gold nanoparticles", *Journal of Materials Chemistry* **18**, 2415 (2008). DOI: 10.1039/b714950f.

[102] M. Grzelczak, J. Pérez-Juste, P. Mulvaney, L. M. Liz-Marzán, "Shape control in gold nanoparticle synthesis", *Chemical Society Reviews* **37**, 1783 (2008). DOI: 10.1039/b711490g.

[103] D. Walls, G. J. Milburn, *Quantum Optics* (Springer Berlin Heidelberg, Berlin, Heidelberg, 2008).

[104] M. Pelton, "Modified spontaneous emission in nanophotonic structures", *Nature Photonics* **9**, 427 (2015). DOI: 10.1038/NPHOTON.2015.103.

[105] E. Purcell, "Spontaneous emission probabilities at radio frequencies", *Physical Review* **69**, 674 (1946). DOI: 10.1103/PhysRev.69.674.2.

[106] M. Agio, "Molecular Scattering and Fluorescence in Strongly Confined Optical Fields", Ph.D. thesis (2011).

[107] T. A. Klar, J. Feldmann, *Complex-Shaped Metal Nanoparticles* (Wiley-VCH Verlag GmbH & Co. KGaA, Weinheim, Germany, 2012), pp. 395–427.

[108] P. Meystre, M. Sargent, *Elements of Quantum Optics* (Springer Berlin Heidelberg, Berlin, Heidelberg, 2007).

[109] S. A. Maier, "Plasmonic field enhancement and SERS in the effective mode volume picture", *Optics Express* **14**, 1957 (2006). DOI: 10.1364/OE.14.001957.

[110] A. F. Koenderink, "On the use of Purcell factors for plasmon antennas", *Optics Letters* **35**, 4208 (2010). DOI: 10.1364/OL.35.004208.

[111] B. Gallinet, J. Butet, O. J. F. Martin, "Numerical methods for nanophotonics: standard problems and future challenges", *Laser & Photonics Reviews* **9**, 577 (2015). DOI: 10.1002/lpor.201500122.

[112] J. Smajic, C. Hafner, L. Raguin, K. Tavzarashvili, M. Mishrikey, “Comparison of Numerical Methods for the Analysis of Plasmonic Structures”, *Journal of Computational and Theoretical Nanoscience* **6**, 763 (2009). DOI: 10.1166/jctn.2009.1107.

[113] G. A. E. Vandenbosch, V. Volski, N. Verellen, V. V. Moshchalkov, “On the use of the method of moments in plasmonic applications”, *Radio Science* **46**, n/a (2011). DOI: 10.1029/2010RS004582.

[114] K. Han, C.-H. Chang, “Numerical Modeling of Sub-Wavelength Anti-Reflective Structures for Solar Module Applications”, *Nanomaterials* **4**, 87 (2014). DOI: 10.3390/nano4010087.

[115] F. Kahnert, “Numerical methods in electromagnetic scattering theory”, *Journal of Quantitative Spectroscopy and Radiative Transfer* **79-80**, 775 (2003). DOI: 10.1016/S0022-4073(02)00321-7.

[116] E. Miller, “A selective survey of computational electromagnetics”, *IEEE Transactions on Antennas and Propagation* **36**, 1281 (1988). DOI: 10.1109/8.8607.

[117] B. Gallinet, T. Siegfried, H. Sigg, P. Nordlander, O. J. Martin, “Plasmonic radiance: Probing structure at the Ångström scale with visible light”, *Nano Letters* **13**, 497 (2013). DOI: 10.1021/nl303896d.

[118] K. S. Yee, “Numerical Solution of Initial Boundary Value Problems Involving Maxwell’s Equations in Isotropic Media”, *IEEE Transactions on Antennas and Propagation* **14**, 302 (1966). DOI: 10.1109/TAP.1966.1138693.

[119] A. Taflove, S. C. Hagness, *Computational Electrodynamics: The Finite Difference Time-Domain Method* (Artech House, 2005), third edn.

[120] K. S. Kunz, R. J. Luebbers, *The Finite Difference Time Domain Method for Electromagnetics* (CRC Press, 1993).

[121] S. D. Gedney, *Introduction to the Finite-Difference Time-Domain (FDTD) Method for Electromagnetics* (Morgan & Claypool, 2011).

[122] FDominec, “FDTD Yee grid 2d-3d”, https://en.wikipedia.org/wiki/File:FDTD_Yee_grid_2d-3d.svg (2015), (Accessed: 2018-03-20). Licensed under ÂăCreative Commons Attribution-Share Alike 4.0 International license.

[123] J. S. Toll, “Causality and the Dispersion Relation: Logical Foundations”, *Physical Review* **104**, 1760 (1956). DOI: 10.1103/PhysRev.104.1760.

[124] J.-P. Berenger, “A perfectly matched layer for the absorption of electromagnetic waves”, *Journal of Computational Physics* **114**, 185 (1994). DOI: 10.1006/jcph.1994.1159.

[125] D. Katz, E. Thiele, A. Taflove, “Validation and extension to three dimensions of the Berenger PML absorbing boundary condition for FD-TD meshes”, *IEEE Microwave and Guided Wave Letters* **4**, 268 (1994). DOI: 10.1109/75.311494.

[126] K. Umashankar, A. Taflove, “A Novel Method to Analyze Electromagnetic Scattering of Complex Objects”, *IEEE Transactions on Electromagnetic Compatibility* **EMC-24**, 397 (1982). DOI: 10.1109/TEMC.1982.304054.

[127] S. A. Schelkunoff, “Kirchhoof’s formula, its vector analogue, and other field equivalence theorems”, *Communications on Pure and Applied Mathematics* **4**, 43 (1951). DOI: 10.1002/cpa.3160040107.

[128] “Lumerical Inc.”, https://www.lumerical.com/tcad-products/fdtd/.

[129] I. R. Çapoglu, J. D. Rogers, A. Taflove, V. Backman, *The Microscope in a Computer: Image Synthesis from Three-Dimensional Full-Vector Solutions of Maxwell’s Equations at the Nanometer Scale*, vol. 57 of *Progress in Optics* (Elsevier, 2012).

[130] B. Fu, J. D. Flynn, B. P. Isaacoff, D. J. Rowland, J. S. Biteen, “Super-Resolving the Distance-Dependent Plasmon-Enhanced Fluorescence of Single Dye and Fluorescent Protein Molecules”, *Journal of Physical Chemistry C* **119**, 19350 (2015). DOI: 10.1021/acs.jpcc.5b05154.

[131] S. H. Gage, “Modern Dark-Field Microscopy and the History of Its Development”, *Transactions of the American Microscopical Society* **39**, 95 (1920). DOI: 10.2307/3221838.

[132] P. Midgley, M. Weyland, “3D electron microscopy in the physical sciences: the development of Z-contrast and EFTEM tomography”, *Ultramicroscopy* **96**, 413 (2003). DOI: 10.1016/S0304-3991(03)00105-0.

[133] L. Jiang, *et al.*, “Accurate Modeling of Dark-Field Scattering Spectra of Plasmonic Nanostructures”, *ACS Nano* **9**, 10039 (2015). DOI: 10.1021/acsnano.5b03622.

[134] S. Eustis, M. A. El-Sayed, “Why gold nanoparticles are more precious than pretty gold: Noble metal surface plasmon resonance and its enhancement of the radiative and nonradiative properties of nanocrystals of different shapes”, *Chem. Soc. Rev.* **35**, 209 (2006). DOI: 10.1039/B514191E.

[135] X. Huang, S. Neretina, M. A. El-Sayed, “Gold Nanorods: From Synthesis and Properties to Biological and Biomedical Applications”, *Advanced Materials* **21**, 4880 (2009). DOI: 10.1002/adma.200802789.

[136] C. J. Murphy, *et al.*, “The Many Faces of Gold Nanorods”, *The Journal of Physical Chemistry Letters* **1**, 2867 (2010). DOI: 10.1021/jz100992x.

[137] E. C. Dreaden, A. M. Alkilany, X. Huang, C. J. Murphy, M. A. El-Sayed, “The golden age: gold nanoparticles for biomedicine”, *Chem. Soc. Rev.* **41**, 2740 (2012). DOI: 10.1039/C1CS15237H.

[138] H. Chen, L. Shao, Q. Li, J. Wang, “Gold nanorods and their plasmonic properties”, *Chem. Soc. Rev.* **42**, 2679 (2013). DOI: 10.1039/C2CS35367A.

[139] J. Pérez-Juste, I. Pastoriza-Santos, L. M. Liz-Marzán, P. Mulvaney, "Gold nanorods: Synthesis, characterization and applications", *Coordination Chemistry Reviews* **249**, 1870 (2005). DOI: 10.1016/j.ccr.2005.01.030.

[140] S. E. Lohse, C. J. Murphy, "The Quest for Shape Control: A History of Gold Nanorod Synthesis", *Chemistry of Materials* **25**, 1250 (2013). DOI: 10.1021/cm303708p.

[141] N. D. Burrows, *et al.*, "Surface Chemistry of Gold Nanorods", *Langmuir* **32**, 9905 (2016). DOI: 10.1021/acs.langmuir.6b02706.

[142] P. Zijlstra, J. W. M. Chon, M. Gu, "Five-dimensional optical recording mediated by surface plasmons in gold nanorods", *Nature* **459**, 410 (2009). DOI: 10.1038/nature08053.

[143] Q. Dai, *et al.*, "Encoding Random Hot Spots of a Volume Gold Nanorod Assembly for Ultralow Energy Memory", *Advanced Materials* **29**, 1701918 (2017). DOI: 10.1002/adma.201701918.

[144] A. J. Mieszawska, W. J. Mulder, Z. A. Fayad, D. P. Cormode, "Multifunctional gold nanoparticles for diagnosis and therapy of disease", *Molecular Pharmaceutics* **10**, 831 (2013). DOI: 10.1021/mp3005885.

[145] J. E. Donehue, E. Wertz, C. N. Talicska, J. S. Biteen, "Plasmon-Enhanced brightness and photostability from single fluorescent proteins coupled to gold nanorods", *Journal of Physical Chemistry C* **118**, 15027 (2014). DOI: 10.1021/jp504186n.

[146] H. Yuan, S. Khatua, P. Zijlstra, M. Yorulmaz, M. Orrit, "Thousand-fold enhancement of single-molecule fluorescence near a single gold nanorod", *Angewandte Chemie - International Edition* **52**, 1217 (2013). DOI: 10.1002/anie.201208125.

[147] W. Zhang, M. Caldarola, B. Pradhan, M. Orrit, "Gold Nanorod Enhanced Fluorescence Enables Single-Molecule Electrochemistry of Methylene Blue", *Angewandte Chemie International Edition* **56**, 3566 (2017). DOI: 10.1002/anie.201612389.

[148] Z. Wang, X. Meng, A. V. Kildishev, A. Boltasseva, V. M. Shalaev, "Nanolasers Enabled by Metallic Nanoparticles: From Spasers to Random Lasers", *Laser & Photonics Reviews* **11**, 1700212 (2017). DOI: 10.1002/lpor.201700212.

[149] R. Chandrasekar, *et al.*, "Lasing Action with Gold Nanorod Hyperbolic Metamaterials", *ACS Photonics* **4**, 674 (2017). DOI: 10.1021/acsphotonics.7b00010.

[150] H. Katz-Boon, *et al.*, "Three-Dimensional Morphology and Crystallography of Gold Nanorods", *Nano Letters* **11**, 273 (2011). DOI: 10.1021/nl103726k.

[151] J. Pérez-Juste, L. M. Liz-Marzán, S. Carnie, D. Y. C. Chan, P. Mulvaney, "Electric-Field-Directed Growth of Gold Nanorods in Aqueous Surfactant Solutions", *Advanced Functional Materials* **14**, 571 (2004). DOI: 10.1002/adfm.200305068.

[152] C. Ayala-Orozco, *et al.*, "Fluorescence Enhancement of Molecules Inside a Gold Nanomatryoshka", *Nano Letters* **14**, 2926 (2014). DOI: 10.1021/nl501027j.

[153] V. Giannini, *et al.*, "Plasmonic Nanoantennas: Fundamentals and Their Use in Controlling the Radiative Properties of Nanoemitters", *Chemical Reviews* **111**, 3888 (2011). DOI: 10.1021/cr1002672.

[154] K. Drexhage, "Influence of a dielectric interface on fluorescence decay time", *Journal of Luminescence* **1-2**, 693 (1970). DOI: 10.1016/0022-2313(70)90082-7.

[155] K. H. Drexhage, "MONOMOLECULAR LAYERS AND LIGHT", *Scientific American* **222**, 108 (1970).

[156] R. R. Chance, A. Prock, R. Silbey, *Advances in Chemical Physics* (1978), pp. 1–65.

[157] R. R. Chance, A. H. Miller, A. Prock, R. Silbey, "Fluorescence and energy transfer near interfaces: The complete and quantitative description of the Eu +3 /mirror systems", *The Journal of Chemical Physics* **63**, 1589 (1975). DOI: 10.1063/1.431483.

[158] G. W. Ford, W. H. Weber, "Electromagnetic interactions of molecules with metal surfaces", *Physics Reports* **113**, 195 (1984). DOI: 10.1016/0370-1573(84)90098-X.

[159] D. Waldeck, A. Alivisatos, C. Harris, "Nonradiative damping of molecular electronic excited states by metal surfaces", *Surface Science* **158**, 103 (1985). DOI: 10.1016/0039-6028(85)90290-0.

[160] W. L. Barnes, "Fluorescence near interfaces: The role of photonic mode density", *Journal of Modern Optics* **45**, 661 (1998). DOI: 10.1080/09500349808230614.

[161] A. Mohammadi, V. Sandoghdar, M. Agio, "Gold nanorods and nanospheroids for enhancing spontaneous emission", *New Journal of Physics* **10**, 105015 (2008). DOI: 10.1088/1367-2630/10/10/105015.

[162] S. Kühn, U. Håkanson, L. Rogobete, V. Sandoghdar, "Enhancement of single-molecule fluorescence using a gold nanoparticle as an optical nanoantenna", *Physical Review Letters* **97**, 017402 (2006). DOI: 10.1103/PhysRevLett.97.017402.

[163] S. Kuhn, G. Mori, M. Agio, V. Sandoghdar, "Modification of single molecule fluorescence close to a nanostructure: radiation pattern, spontaneous emission and quenching", *Molecular Physics* **106**, 893 (2008). DOI: 10.1080/00268970802002510.

[164] P. Bharadwaj, L. Novotny, "Spectral dependence of single molecule fluorescence enhancement", *Optics Express* **15**, 14266 (2007). DOI: 10.1364/OE.15.014266.

[165] P. Anger, P. Bharadwaj, L. Novotny, "Enhancement and quenching of single-molecule fluorescence", *Physical Review Letters* **96**, 113002 (2006). DOI: 10.1103/PhysRevLett.96.113002.

[166] K. Munechika, *et al.*, “Quantum dot/plasmonic nanoparticle metachromophores with quantum yields that vary with excitation wavelength”, *Nano Letters* **11**, 2725 (2011). DOI: 10.1021/nl2010127.

[167] A. Rose, *et al.*, “Control of Radiative Processes Using Tunable Plasmonic Nanopatch Antennas”, *Nano Letters* **14**, 4797 (2014). DOI: 10.1021/nl501976f.

[168] J. S. Biteen, D. Pacifici, N. S. Lewis, H. A. Atwater, “Enhanced radiative emission rate and quantum efficiency in coupled silicon nanocrystal-nanostructured gold emitters”, *Nano Letters* **5**, 1768 (2005). DOI: 10.1021/nl051207z.

[169] Y. Xu, R. K. Lee, A. Yariv, “Quantum analysis and the classical analysis of spontaneous emission in a microcavity”, *Physical Review A* **61**, 033807 (2000). DOI: 10.1103/PhysRevA.61.033807.

[170] S. Khatua, *et al.*, “Resonant plasmonic enhancement of single-molecule fluorescence by individual gold nanorods”, *ACS Nano* **8**, 4440 (2014). DOI: 10.1021/nn406434y.

[171] J. Yang, M. Perrin, P. Lalanne, “Analytical formalism for the interaction of two-level quantum systems with metal nanoresonators”, *Physical Review X* **5**, 021008 (2015). DOI: 10.1103/PhysRevX.5.021008.

[172] C. Sauvan, J. P. Hugonin, I. S. Maksymov, P. Lalanne, “Theory of the spontaneous optical emission of nanosize photonic and plasmon resonators”, *Physical Review Letters* **110**, 237401 (2013). DOI: 10.1103/PhysRevLett.110.237401.

[173] T. A. Klar, “personal communication” (2015).

[174] A. B. Myers, “Molecular Electronic Spectral Broadening in Liquids and Glasses”, *Annual Review of Physical Chemistry* **49**, 267 (1998). DOI: 10.1146/annurev.physchem.49.1.267.

[175] K. Umezawa, A. Matsui, Y. Nakamura, D. Citterio, K. Suzuki, “Bright, Color-Tunable Fluorescent Dyes in the Vis/NIR Region: Establishment of New âĂIJTailor-MadeâĂİ Multicolor Fluorophores Based on Borondipyrromethene”, *Chemistry - A European Journal* **15**, 1096 (2009). DOI: 10.1002/chem.200801906.

[176] M. K. Cheezum, W. F. Walker, W. H. Guilford, “Quantitative comparison of algorithms for tracking single fluorescent particles”, *Biophysical Journal* **81**, 2378 (2001). DOI: 10.1016/S0006-3495(01)75884-5.

[177] B. C. Chen, *et al.*, “Lattice light-sheet microscopy: Imaging molecules to embryos at high spatiotemporal resolution”, *Science* **346**, 1257998 (2014). DOI: 10.1126/science.1257998.

[178] F. Greiss, M. Deligiannaki, C. Jung, U. Gaul, D. Braun, “Single-Molecule Imaging in Living Drosophila Embryos with Reflected Light-Sheet Microscopy”, *Biophysical Journal* **110**, 939 (2016). DOI: 10.1016/j.bpj.2015.12.035.

[179] M. Tokunaga, N. Imamoto, K. Sakata-Sogawa, "Highly inclined thin illumination enables clear single-molecule imaging in cells", *Nature Methods* **5**, 159 (2008). DOI: 10.1038/nmeth1171.

[180] D. Axelrod, "Total Internal Reflection Fluorescence Microscopy", *Methods in Cell Biology* **30**, 245 (1989). DOI: 10.1016/S0091-679X(08)60982-6.

[181] T. Ha, P. Tinnefeld, "Photophysics of Fluorescent Probes for Single-Molecule Biophysics and Super-Resolution Imaging", *Annual Review of Physical Chemistry* **63**, 595 (2012). DOI: 10.1146/annurev-physchem-032210-103340.

[182] E. J. Titus, K. A. Willets, "Accuracy of superlocalization imaging using Gaussian and dipole emission point-spread functions for modeling gold nanorod luminescence", *ACS Nano* **7**, 6258 (2013). DOI: 10.1021/nn4022845.

[183] E. Hoogendoorn, *et al.*, "The fidelity of stochastic single-molecule super-resolution reconstructions critically depends upon robust background estimation", *Scientific Reports* **4**, 3854 (2014). DOI: 10.1038/srep03854.

[184] T. Y. Chen, *et al.*, "Concentration-and chromosome-organization-dependent regulator unbinding from DNA for transcription regulation in living cells", *Nature Communications* **6**, 7445 (2015). DOI: 10.1038/ncomms8445.

[185] K. L. Blythe, E. J. Titus, K. A. Willets, "Triplet-state-mediated super-resolution imaging of fluorophore-labeled gold nanorods", *ChemPhysChem* **15**, 784 (2014). DOI: 10.1002/cphc.201300767.

[186] K. L. Blythe, E. J. Titus, K. A. Willets, "Comparing the Accuracy of Reconstructed Image Size in Super-Resolution Imaging of Fluorophore-Labeled Gold Nanorods Using Different Fit Models", *The Journal of Physical Chemistry C* **119**, 19333 (2015). DOI: 10.1021/acs.jpcc.5b04993.

[187] X. Zhou, *et al.*, "Quantitative super-resolution imaging uncovers reactivity patterns on single nanocatalysts", *Nature Nanotechnology* **7**, 237 (2012). DOI: 10.1038/nnano.2012.18.

[188] P. D. Simonson, E. Rothenberg, P. R. Selvin, "Single-molecule-based super-resolution images in the presence of multiple fluorophores", *Nano Letters* **11**, 5090 (2011). DOI: 10.1021/nl203560r.

[189] D. T. Burnette, P. Sengupta, Y. Dai, J. Lippincott-Schwartz, B. Kachar, "Bleaching/blinking assisted localization microscopy for superresolution imaging using standard fluorescent molecules", *Proceedings of the National Academy of Sciences* **108**, 21081 (2011). DOI: 10.1073/pnas.1117430109.

[190] A. Carattino, M. Caldarola, M. Orrit, "Gold nanoparticles as absolute nanothermometers", *Nano Letters* **18**, 874 (2018). DOI: 10.1021/acs.nanolett.7b04145.

[191] Y. Liao, Y. Li, J. W. Schroeder, L. A. Simmons, J. S. Biteen, "Single-Molecule DNA Polymerase Dynamics at a Bacterial Replisome in Live Cells", *Biophysical Journal* **111**, 2562 (2016). DOI: 10.1016/j.bpj.2016.11.006.

[192] H. W. Kuhn, *Naval Research Logistics Quarterly* (Wiley Subscription Services, Inc., A Wiley Company, 1955), vol. 2, pp. 83–97.

[193] Y. Liao, J. W. Schroeder, B. Gao, L. A. Simmons, J. S. Biteen, "Single-molecule motions and interactions in live cells reveal target search dynamics in mismatch repair", *Proceedings of the National Academy of Sciences* **112**, E6898 (2015). DOI: 10.1073/pnas.1507386112.

[194] D. J. Rowland, J. S. Biteen, "Measuring molecular motions inside single cells with improved analysis of single-particle trajectories", *Chemical Physics Letters* **674**, 173 (2017). DOI: 10.1016/j.cplett.2017.02.052.

[195] H. W. Kuhn, "Variants of the hungarian method for assignment problems", *Naval Research Logistics Quarterly* **3**, 253 (1956). DOI: 10.1002/nav.3800030404.

[196] M. J. Saxton, "Single-particle tracking: The distribution of diffusion coefficients", *Biophysical Journal* **72**, 1744 (1997). DOI: 10.1016/S0006-3495(97)78820-9.

[197] J. R. Lakowicz, "Radiative decay engineering: Biophysical and biomedical applications", *Analytical Biochemistry* **298**, 1 (2001). DOI: 10.1006/abio.2001.5377.

[198] J. Lakowicz, Y. Fu, "Modification of single molecule fluorescence near metallic nanostructures", *Laser & Photonics Review* **3**, 221 (2009). DOI: 10.1002/lpor.200810035.

[199] A. Kinkhabwala, *et al.*, "Large single-molecule fluorescence enhancements produced by a bowtie nanoantenna", *Nature Photonics* **3**, 654 (2009). DOI: 10.1038/nphoton.2009.187.

[200] S. A. Lee, J. S. Biteen, "Interplay of Nanoparticle Resonance Frequency and Array Surface Coverage in Live-Cell Plasmon-Enhanced Single-Molecule Imaging", *The Journal of Physical Chemistry C* **122**, 5705 (2018). DOI: 10.1021/acs.jpcc.8b01436.

[201] A. S. De Silva Indrasekara, *et al.*, "Optimization of Spectral and Spatial Conditions to Improve Super-Resolution Imaging of Plasmonic Nanoparticles", *Journal of Physical Chemistry Letters* **8**, 299 (2017). DOI: 10.1021/acs.jpclett.6b02569.

[202] H. Cang, *et al.*, "Probing the electromagnetic field of a 15-nanometre hotspot by single molecule imaging", *Nature* **469**, 385 (2011). DOI: 10.1038/nature09698.

[203] C. Ropp, *et al.*, "Nanoscale probing of image-dipole interactions in a metallic nanostructure", *Nature Communications* **6**, 6558 (2015). DOI: 10.1038/ncomms7558.

[204] F. Tam, G. P. Goodrich, B. R. Johnson, N. J. Halas, "Plasmonic enhancement of molecular fluorescence", *Nano Letters* **7**, 496 (2007). DOI: 10.1021/nl062901x.

[205] Y. Chen, K. Munechika, D. S. Ginger, "Dependence of fluorescence intensity on the spectral overlap between fluorophores and plasmon resonant single silver nanoparticles", *Nano Letters* **7**, 690 (2007). DOI: 10.1021/nl062795z.

[206] L. Su, *et al.*, "Super-resolution Localization and Defocused Fluorescence Microscopy on Resonantly Coupled Single-Molecule, Single-Nanorod Hybrids", *ACS Nano* **10**, 2455 (2016). DOI: 10.1021/acsnano.5b07294.

[207] M. Heilemann, *et al.*, "Subdiffraction-Resolution Fluorescence Imaging with Conventional Fluorescent Probes", *Angewandte Chemie International Edition* **47**, 6172 (2008). DOI: 10.1002/anie.200802376.

[208] M. Heilemann, S. van de Linde, A. Mukherjee, M. Sauer, "Super-Resolution Imaging with Small Organic Fluorophores", *Angewandte Chemie International Edition* **48**, 6903 (2009). DOI: 10.1002/anie.200902073.

[209] J. Vogelsang, T. Cordes, C. Forthmann, C. Steinhauer, P. Tinnefeld, "Controlling the fluorescence of ordinary oxazine dyes for single-molecule switching and super-resolution microscopy", *Proceedings of the National Academy of Sciences* **106**, 8107 (2009). DOI: 10.1073/pnas.0811875106.

[210] S. van de Linde, *et al.*, "Direct stochastic optical reconstruction microscopy with standard fluorescent probes", *Nature Protocols* **6**, 991 (2011). DOI: 10.1038/nprot.2011.336.

[211] C. J. Murphy, *et al.*, "Anisotropic metal nanoparticles: Synthesis, assembly, and optical applications", *Journal of Physical Chemistry B* **109**, 13857 (2005). DOI: 10.1021/jp0516846.

[212] L. Shao, Z. J. Yang, D. Andrén, P. Johansson, M. Käll, "Gold Nanorod Rotary Motors Driven by Resonant Light Scattering", *ACS Nano* **9**, 12542 (2015). DOI: 10.1021/acsnano.5b06311.

[213] Y. Gao, Y. Yu, L. Sanchez, Y. Yu, "Seeing the unseen: Imaging rotation in cells with designer anisotropic particles", *Micron* **101**, 123 (2017). DOI: 10.1016/j.micron.2017.07.002.

[214] K. Chen, *et al.*, "Characteristic rotational behaviors of rod-shaped cargo revealed by automated five-dimensional single particle tracking", *Nature Communications* **8**, 887 (2017). DOI: 10.1038/s41467-017-01001-9.

[215] T. Li, *et al.*, "Three-Dimensional Orientation Sensors by Defocused Imaging of Gold Nanorods through an Ordinary Wide-Field Microscope", *ACS Nano* **6**, 1268 (2012). DOI: 10.1021/nn203979n.

[216] S. Biswas, D. Nepal, K. Park, R. A. Vaia, "Orientation Sensing with Color Using Plasmonic Gold Nanorods and Assemblies", *The Journal of Physical Chemistry Letters* **3**, 2568 (2012). DOI: 10.1021/jz3009908.

[217] S. Enoki, *et al.*, “High-Speed Angle-Resolved Imaging of a Single Gold Nanorod with Microsecond Temporal Resolution and One-Degree Angle Precision”, *Analytical Chemistry* **87**, 2079 (2015). DOI: 10.1021/ac502408c.

[218] J. W. Ha, “Recent advances in single particle rotational tracking of plasmonic anisotropic gold nanoparticles under far-field optical microscopy”, *Applied Spectroscopy Reviews* **51**, 552 (2016). DOI: 10.1080/05704928.2016.1165688.

[219] A. Edelstein, N. Amodaj, K. Hoover, R. Vale, N. Stuurman, *Current Protocols in Molecular Biology*, no. SUPPL. 92 (John Wiley & Sons, Inc., Hoboken, NJ, USA, 2010).

[220] A. D. Edelstein, *et al.*, “Advanced methods of microscope control using μManager software”, *Journal of Biological Methods* **1**, 10 (2014). DOI: 10.14440/jbm.2014.36.

[221] C. Lethiec, *et al.*, “Measurement of three-dimensional dipole orientation of a single fluorescent nanoemitter by emission polarization analysis”, *Physical Review X* **4**, 021037 (2014). DOI: 10.1103/PhysRevX.4.021037.

[222] T. Ming, *et al.*, “Strong polarization dependence of plasmon-enhanced fluorescence on single gold nanorods”, *Nano Letters* **9**, 3896 (2009). DOI: 10.1021/nl902095q.

[223] S. Colabrese, M. Castello, G. Vicidomini, A. Del Bue, “Machine learning approach for single molecule localisation microscopy”, *Biomedical Optics Express* **9**, 1680 (2018). DOI: 10.1364/BOE.9.001680.

[224] E. Nehme, L. E. Weiss, T. Michaeli, Y. Shechtman, “Deep-STORM: super-resolution single-molecule microscopy by deep learning”, *Optica* **5**, 458 (2018). DOI: 10.1364/OPTICA.5.000458.

[225] A. C.-Y. Wu, S. A. Rifkin, “Aro: a machine learning approach to identifying single molecules and estimating classification error in fluorescence microscopy images”, *BMC Bioinformatics* **16**, 102 (2015). DOI: 10.1186/s12859-015-0534-z.

[226] R. C. Boutelle, D. Neuhauser, S. Weiss, “Far-Field Super-resolution Detection of Plasmonic Near-Fields”, *ACS Nano* **10**, 7955 (2016). DOI: 10.1021/acsnano.6b03873.

[227] E. Johlin, *et al.*, “Super-resolution imaging of lightâĂŞmatter interactions near single semiconductor nanowires”, *Nature Communications* **7**, 13950 (2016). DOI: 10.1038/ncomms13950.

[228] M. Raab, C. Vietz, F. D. Stefani, G. P. Acuna, P. Tinnefeld, “Shifting molecular localization by plasmonic coupling in a single-molecule mirage”, *Nature Communications* **8**, 13966 (2017). DOI: 10.1038/ncomms13966.

[229] D. L. Mack, *et al.*, “Decoupling absorption and emission processes in super-resolution localization of emitters in a plasmonic hotspot”, *Nature Communications* **8**, 14513 (2017). DOI: 10.1038/ncomms14513.

[230] K. Guo, M. A. Verschuuren, A. Femius Koenderink, “Superresolution imaging of the local density of states in plasmon lattices”, *Optica* **3**, 289 (2016). DOI: 10.1364/OPTICA.3.000289.

[231] C. W. Heaps, G. C. Schatz, “Modeling super-resolution SERS using a T-matrix method to elucidate molecule-nanoparticle coupling and the origins of localization errors”, *The Journal of Chemical Physics* **146**, 224201 (2017). DOI: 10.1063/1.4984120.

[232] A. Taylor, R. Verhoef, M. Beuwer, Y. Wang, P. Zijlstra, “All-Optical Imaging of Gold Nanoparticle Geometry Using Super-Resolution Microscopy”, *The Journal of Physical Chemistry C* **122**, 2336 (2018). DOI: 10.1021/acs.jpcc.7b12473.

[233] F. D. Moura Neto, A. J. da Silva Neto, *An Introduction to Inverse Problems with Applications* (Springer Berlin Heidelberg, Berlin, Heidelberg, 2013).

[234] C. R. Vogel, *Computational Methods for Inverse Problems* (Society for Industrial and Applied Mathematics, 2002).

[235] A. Tarantola, *Inverse Problem Theory and Methods for Model Parameter Estimation* (Society for Industrial and Applied Mathematics, 2005).

[236] T. Hu, *et al.*, “Self-organization of plasmonic and excitonic nanoparticles into resonant chiral supraparticle assemblies”, *Nano Letters* **14**, 6799 (2014). DOI: 10.1021/nl502237f.

[237] C. Noguez, I. L. Garzón, “Optically active metal nanoparticles”, *Chemical Society Reviews* **38**, 757 (2009). DOI: 10.1039/b800404h.

[238] V. E. Ferry, J. M. Smith, A. P. Alivisatos, “Symmetry Breaking in Tetrahedral Chiral Plasmonic Nanoparticle Assemblies”, *ACS Photonics* **1**, 1189 (2014). DOI: 10.1021/ph5002632.

[239] X. Duan, S. Yue, N. Liu, “Understanding complex chiral plasmonics”, *Nanoscale* **7**, 17237 (2015). DOI: 10.1039/C5NR04050G.

[240] L. Y. Wang, *et al.*, “Circular Differential Scattering of Single Chiral Self-Assembled Gold Nanorod Dimers”, *ACS Photonics* **2**, 1602 (2015). DOI: 10.1021/acsphotonics.5b00395.

[241] L. V. Poulikakos, *et al.*, “Optical Chirality Flux as a Useful Far-Field Probe of Chiral Near Fields”, *ACS Photonics* **3**, 1619 (2016). DOI: 10.1021/acsphotonics.6b00201.

[242] L. V. Poulikakos, P. Thureja, A. Stollmann, E. De Leo, D. J. Norris, “Chiral Light Design and Detection Inspired by Optical Antenna Theory”, *Nano Letters* p. acs.nanolett.8b00083 (2018). DOI: 10.1021/acs.nanolett.8b00083.

[243] C. L. Holloway, *et al.*, “An Overview of the Theory and Applications of Metasurfaces: The Two-Dimensional Equivalents of Metamaterials”, *IEEE Antennas and Propagation Magazine* **54**, 10 (2012). DOI: 10.1109/MAP.2012.6230714.

[244] N. Yu, F. Capasso, “Optical Metasurfaces and Prospect of Their Applications Including Fiber Optics”, *Journal of Lightwave Technology* **33**, 2344 (2015). DOI: 10.1109/JLT.2015.2404860.

[245] J. P. Balthasar Mueller, N. A. Rubin, R. C. Devlin, B. Groever, F. Capasso, “Metasurface Polarization Optics: Independent Phase Control of Arbitrary Orthogonal States of Polarization”, *Physical Review Letters* **118**, 113901 (2017). DOI: 10.1103/PhysRevLett.118.113901.

[246] C. Pfeiffer, C. Zhang, V. Ray, L. J. Guo, A. Grbic, “High Performance Bianisotropic Metasurfaces: Asymmetric Transmission of Light”, *Physical Review Letters* **113**, 023902 (2014). DOI: 10.1103/PhysRevLett.113.023902.

[247] C. Pfeiffer, *et al.*, “Efficient Light Bending with Isotropic Metamaterial Huygens’ Surfaces”, *Nano Letters* **14**, 2491 (2014). DOI: 10.1021/nl5001746.

[248] C. Pfeiffer, A. Grbic, “Metamaterial Huygens’ Surfaces: Tailoring Wave Fronts with Reflectionless Sheets”, *Physical Review Letters* **110**, 197401 (2013). DOI: 10.1103/PhysRevLett.110.197401.

[249] C. Pfeiffer, C. Zhang, V. Ray, L. Jay Guo, A. Grbic, “Polarization rotation with ultra-thin bianisotropic metasurfaces”, *Optica* **3**, 427 (2016). DOI: 10.1364/OPTICA.3.000427.

[250] M. P. Backlund, *et al.*, “Removing orientation-induced localization biases in single-molecule microscopy using a broadband metasurface mask”, *Nature Photonics* **10**, 459 (2016). DOI: 10.1038/nphoton.2016.93.

[251] M. D. Lew, W. E. Moerner, “Azimuthal Polarization Filtering for Accurate, Precise, and Robust Single-Molecule Localization Microscopy”, *Nano Letters* **14**, 6407 (2014). DOI: 10.1021/nl502914k.